Digital Spectral Analysis and Adaptive Processing Techniques for Phase Modulated Optical Fiber Sensors

by

Tuan A. Tran

Dissertation submitted to the Faculty of the
Virginia Polytechnic Institute and State University
in partial fulfillment of the requirements for the degree of

Doctor Of Philosophy
In
Electrical Engineering

APPROVED:

Dr. Kent A. Murphy, Chairman

Dr. Richard O. Claus

Dr. Hugh F. VanLandingham

Dr. Ioannis M. Besieris

Dr. James R. Heflin

December 20, 1996

Blacksburg, Virginia

Keywords: Spectral Analysis, Optical Fiber Sensors, Adaptive Signal Processing

Digital Spectral Analysis and Adaptive Processing Techniques for Phase Modulated Optical Fiber Sensors

by

Tuan A. Tran
Dr. Kent A. Murphy, Chairman
Department of Electrical Engineering

(ABSTRACT)

The objective of this work is to investigate new signal processing techniques for optical fiber sensors that utilize the phase information of the electromagnetic field. Research concentrated on Fourier transform spectroscopy as a means for capturing wavelength encoded information from the fiber sensor. Classical spectral analysis utilizing the Fourier transform as a mathematical foundation for relating a time or space signal to its frequency-domain representation was shown to be inadequate for mitigating the bias errors caused by harmonic distortions. A modified spectral estimation algorithm is presented to overcome some of the practical issues while maintaining the high spectral resolution characteristic of the classical technique. This research also showed that unlike in free-space propagation, an optical signal propagating through a fiber waveguide, even over short distances, can experience significant phase modulation noise. A number of chromatic distortion mechanisms including modal interference, mode coupling due to periodic perturbations such as microdeformation and macrobends, and mode field diameter variations are addressed. We treated these issues by employing both theoretical simulation and experimental data. Coupled-mode formalism based upon approximated field solutions is used in the theoretical analysis. An extensive error analysis was also performed to determine how waveguide and noise distortion affect the performance of the spectral estimation algorithm.

Abstract

Acknowledgements

I would like to express my deepest gratitude to my entire advisory committee particularly Dr. K. A. Murphy for his counsel, encouragement, and making my Ph.D. study at Virginia Tech possible. This dissertation is the direct result of his many innovations, insightful leadership and invaluable support. I would like to similarly thank Dr. R. O. Claus for all his encouragements, endless enthusiasm and guidance over the past 8 years. I also want to thank Dr. I. M. Besieris, Dr. H. F. VanLandingham and Dr. J. R. Heflin for their helpful suggestions.

I am grateful to my friends Dr. Marten DeVries, Dr. Vikram Bhatia, Dr. Kevin Shinpaugh and Jonathan Greene for their assistance and technical insights. Special thanks extended to my colleagues Russ May, Mike Gunther, Vivek Arya, Mark Jones, Steve Poland, and everyone at FEORC and F&S for their consultation.

Finally, I would like to thank my parents, Tung Van Tran and Ngan Thi-Bao Tran, my younger siblings, Nga Tran, Minh Tran, Khoa Tran and Ngoc Tran, my entire immediate and extended family for giving me the daily support, encouragement and strength during my study at Virginia Tech. I am extremely grateful to my dearest wife, Dr. Linh Thuy-Do Tran, for delaying her career, for all the sleepless nights caring for our children, Maxwell and Michael, and for her being a wonderful solo parent so that I could complete my study.

Table of Contents

List of Figures

List of Tables

1. Introduction

An interferometer is an optical instrument that splits an optical wave into two waves using a beamsplitter, delays them by unequal optical path lengths, redirects them using mirrors, recombines them using another (or the same) beamsplitter, and detects the intensity of their superposition. The four important examples are the Mach-Zehnder, the Michelson, the Sagnac and the Fabry-Perot interferometers [1,2]. Interferometers have been used for many diverse applications in research science and commercial systems. For example, Fabry-Perot interferometers are used as optical resonators in most gas and semiconductor lasers [3]. Conventional interferometers are also employed in optical spectrum analyzers, sensors and measurement instrumentation [4,5,6]. Since interferometers employ high frequency optical signals, they are capable of resolving wavelength changes on the order of picometers.

The concept of interferometry was first developed in the 18th century. Yet, the widespread use of interferometers as high precision measurement devices was not practical until optical lasers were introduced in the late 1960's. Today most of the development of optical fiber based sensor systems is based on these basic interferometric configurations [3,4].

While phase modulated optical fiber sensors are among the most sensitive, their implementation requires complex stabilization and signal processing methods. Calibration is also a major issue, particularly after an electrical interruption since the initial phase of the interferometer is usually lost. Another fundamental problem associated with conventional interferometric sensors is the ambiguous output signals due to a phase shift

in the sinusoidal transfer function. In recent years, optical fiber-based white light interferometry has been developed as a viable technique to overcome the ambiguity problem aside having the capability for self-calibration [7,8]. The basic white light interferometer system consists of a low coherence light source, a sensing (encoder) interferometer that transfers the measurand into optical path difference information, and a receiving (decoder) interferometer or a optical spectrum analyzer to recover the signal [7]. Because of the low coherence property of the light source, the interference signals can only be detected when the optical path length difference (OPD) in the unbalanced receiving interferometer can match the OPD generated by the sensing interferometer [9].

1.1 Prior Optical Signal Processing Research

Although a number of novel white light interferometric demodulation techniques have been discussed in literature, practical implementation of these techniques has resulted in limited success. Demodulation systems employing a Michelson interferometric cross-correlator have been demonstrated by Lee and Zuliani [8,10]. A similar approach using a Fizeau interferometer was recently demonstrated by Belleville [11]. The simplest technique for recovering the spectrally encoded information is to employ a spectrometer using either a diffraction grating or scanning Fabry-Perot etalon [7]. While numerous optical fiber sensing and demodulation methods have been developed in the past twenty years, the actual signal processing algorithms used to characterize the measurement fields have not been thoroughly investigated. Practical fiber sensor systems must have the following characteristics: 1) real-time measurement capability, 2) fast response, 3) high resolution, 4) high accuracy, and 5) self-referencing. Current research, however, does not adequately address these issues. Even though tremendous progress has been made in the

optical communication field, the development of signal processing techniques for optical fiber sensing systems has been lagging.

1.2 Scope of Research

The motivation for this research is to investigate spectral analysis and digital signal processing techniques to decode phase modulated optical fiber sensors and ultimately to design a robust, effective and reliable algorithm capable of real-time acquisition and processing. · For the dissertation research, fiber optic Fabry-Perot sensors, and spectrometer-based demodulation systems will be evaluated and implemented in the field for applications in materials characterization and analysis, process and health monitoring systems, and manufacturing quality control. Specifically, the issues listed below are considered in this research effort.

- Investigate an optical phase demodulation system employing Fourier spectroscopy,
- Develop digital spectral analysis techniques specifically tailored for the nonuniform wavelength sampling of a continuous optical signal,
- Investigate the impact of chromatic and waveguide distortions on the signal processing algorithms, and
- Assess the system performance of the demodulation system and the means to improve its performance.

1.3 Research Outline

In Chapter 2, we review the operation of interferometers and investigate how the source spectra influence the resolution and dynamic range of the fiber sensor. Specifically, we will study the relationship between the temporal coherence of the source and its effect on the detected fringe visibility. We will later show in Chapter 4 how the fringe visibility relates to the output resolution of the CCD-based gratings demodulation system. Here, we will mainly develop models to aid in our study of the tradeoffs between the measurement resolution and the dynamic range of the fiber sensor.

In Chapter 3 we examine the various demodulation schemes for decoding the Fabry-Perot interferometric signal. Although a number of optical fiber-based cross-correlators are discussed, the main emphasis of this research makes use of the spectrometer.

Chapter 4 emphasizes the fundamentals of digital signal processing and discusses algorithms tailored specifically for grating-based spectrometers. The spectral analysis approach of signal processing is initiated by digitally sampling and transforming the interferogram into the frequency domain using the fast Fourier transform (FFT). From this basic transformation, a variety of adaptive filtering and interpolation procedures (parabolic, Gaussian, Sinc, and centroid fits) will be investigated to optimize the frequency estimation accuracy. To resolve the effect caused by the nonuniform sampling, a novel chromatic power spectrum algorithm is presented.

In Chapter 5 we first summarize the background for the analysis of optical fiber waveguides and discuss the methods used to obtain elementary, monochromatic plane-wave type solutions. We briefly review linearly polarized (LP) modes in optical fibers and use the approximations to simplify the perturbation analysis. We will also

summarize the coupled-mode formalism to describe mode propagation in uniform and slightly non-uniform cylindrical optical fiber systems. This approach is useful for treating waveguide problems involving energy exchange between modes causing wavelength dependent losses.

In Chapter 6, we provide an extensive theoretical and experimental analysis of the errors that arise when the optical fiber is used as a waveguiding medium. Specifically, we investigate how chromatic distortions caused by a) modal interference (two-mode) b) mode-field diameter, and c) wavelength dependent losses affect system performance. Finally, the conclusions and future directions are presented in Chapter 7.

2. Background of Interferometers

When two monochromatic waves of complex amplitude, $E_1(z)$ and $E_2(z)$, in an interferometer are superimposed, the result is a monochromatic wave of the same frequency and complex amplitude described by

$$E(z) = E_1(z) + E_2(z)\,. \tag{2.0-1}$$

The intensities of the constituent waves are $I_1=|E_1(z)|^2$ and $I_2=|E_2(z)|^2$ and the intensity of the total wave is [1,2]

$$I = |E|^2 = |E1+ E2|^2 = |E1|^2 + |E2|^2 + E_2{}^*E_1 + E_1{}^*E_2\,, \tag{2.0-2}$$

$$I = I_1 + I_2 + 2\sqrt{I_1 I_2}\cos\phi\,, \tag{2.0-3}$$

where ϕ is the phase difference between the interfering waves. Assuming that one wave is delayed by a distance *d* with respect to the other so that $E_1 = I_0^{1/2}$ exp (-jkz) and $E_2 = I_0^{1/2}$ exp [-jk(z-d)], where $k=2\pi/\lambda$. The intensity I of the sum of these two waves can be determined by substituting $I_1= I_2=I_0$ and $\phi=2\pi d/\lambda$ into (2.0-3), [1,2]

$$I = 2I_0\left[1+\cos\left(\frac{2\pi d}{\lambda}\right)\right]. \tag{2.0-4}$$

Since the intensity I is dependent on the phase $\phi = 2\pi d/\lambda = 2\pi\nu d/\lambda_o = 2\pi\nu\nu d/c$, where ν is the optical frequency, the interferometer can be used to accurately measure small variations of the distance *d*, the refractive index *n*, or wavelength λ. The output of the interferometer may be monitored with a photodiode which converts the optical intensity into an electric current. In order to use the interferometer to quantify measurements like strain, temperature, or pressure, the source wavelength is typically held constant during the measurement process while either the path length difference or the refractive index of the medium, traveled by the optical waves, is allowed to change.

Fiber optic phase sensors typically utilize one of the classical interferometric configurations for extracting information regarding the applied perturbation. Interferometry-based sensors comprise two signals, the sensing and the reference signal, which constructively and destructively interfere with each other resulting in an intensity modulation at the output. The sensing signal undergoes a phase change due to the perturbation, while the reference signal is kept isolated from the perturbation. The phase difference that results between the two signals manifests itself as an intensity change at the photodetector.

2.1 Fabry-Perot Interferometric Sensors

Fiber optic Fabry-Perot interferometers are used in two basic configurations termed intrinsic and extrinsic. The intrinsic Fabry-Perot interferometer (IFPI) consists of a monochromatic source such as a laser diode that injects light into one of the input arms of a 2x2 bidirectional single-mode coupler. The Fabry-Perot cavity is formed by placing a segment of a single mode fiber that has both endfaces coated with a semi-transparent reflective coating to one of the output arms of the coupler. The signals that form the interference pattern are reflected from the two ends of this fused fiber segment. The

balanced sensor proposed by Lee and Taylor and the high-temperature sapphire sensor proposed by Wang are examples of intrinsic Fabry-Perot interferometers [12,13,14]. In an extrinsic Fabry-Perot interferometer, the resonant cavity is formed by placing two optical fibers in an alignment tube separated by an air-gap [15,16].

The intrinsic Fabry-Perot interferometers suffer from several inherent drawbacks. Because the sensing fiber must be fused to one of the arms of the coupler, it is difficult to prevent the metal oxide, which has a lower melting temperature than silica, from deteriorating. The IFPI sensors are highly sensitive to thermal effects and are susceptible to six states of strain. In order to overcome the construction difficulties and avoid the thermal and cross-sensitivity effects inherent with IFPI, the extrinsic Fabry-Perot inteferometer (EFPI) was developed by Murphy [15,16]. The Fabry-Perot cavity is formed between an input/output optical fiber and another reflecting surface. To simplify the construction of the EFPI sensor, for the opposing reflecting surface one may use either a singlemode or multimode fiber.

2.2 Finesse of Fabry-Perot Cavity

In the simplified analysis of the Fabry-Perot cavity discussed above, we have assumed that the multiple reflections from the glass/air interfaces did not contribute to the intensity modulation at the output. This assumption is justified because the Fresnel reflection coefficient [1],

$$r = \left(\frac{n_1 - n_2}{n_1 + n_2} \right)^2, \tag{2.2-1}$$

for normal incidence at the glass/air interface is just 4% (for n_1=1.48 and n_2=1.00), where n_1 and n_2 are the refractive indices of the two media forming the interface. Due to the low

reflectivity of the Fabry-Perot cavity, the effect of the second and higher order reflections are negligible. If n_l can be made higher by coating the ends of the input and reflecting fiber with multilayer dielectric films or with partially transparent films of metals, the reflection coefficient can be increased and the amplitude of the second and higher order reflections would become high enough to cause a change in the intensity distribution at the photodetector. In modeling the output response of the Fabry-Perot inteferometer, we need to account for the reflection properties of the resonant cavity.

2.2.1 Lossless Fabry-Perot Cavity

Consider an ideal Fabry-Perot cavity assembled from two singlemode fibers which have thin metal or dielectric coatings, let the input light of amplitude *A* be incident on the i^{th} interface (i=1,2 for the two interfaces). If we assume that the mirrors are deposited with metal coating having no absorption, then there will be a $\pi/2$ phase shift between the transmitted and the reflected waves at both interfaces [17]. Furthermore, we also assume that the radiation source has an infinite coherence length. If we let r_i and t_i be the mirror reflectance and transmittance, the reflected and transmitted amplitudes are given by $jA\sqrt{r_i}$ and $jA\sqrt{t_i}$, respectively. Since both mirrors are assumed to be lossless, the sum of the reflectance and transmission equals one [2].

The amplitude of the resulting transmitted wave is the sum of the waves that are transmitted through the second interface. The ratio of the transmitted power to the incident power is

$$\frac{I_t}{I_i} = \frac{t_1 t_2}{1 - r_1 r_2 - 2\sqrt{r_1 r_2}\cos\left(\frac{4\pi nd}{\lambda}\right)} = \frac{(1-r_1)(1-r_2)}{1 - r_1 r_2 - 2\sqrt{r_1 r_2}\cos\left(\frac{4\pi nd}{\lambda}\right)}. \qquad (2.2.1\text{-}1)$$

Similarly, the ratio of the reflected power to the incident power and is given by

$$\frac{I_r}{I_i} = \frac{r_1^2 + r_2^2 + 2\sqrt{r_1 r_2}\cos\phi}{1 - r_1 r_2 - 2\sqrt{r_1 r_2}\cos\phi}, \qquad (2.2.1\text{-}2)$$

where $\phi=4\pi d/\lambda$ is the round trip phase shift in the cavity. Assuming that $r_1=r_2$ (hence $t_1=t_2$) and defining the transmittance as $t_1 t_2$ and the reflectance $R=r_1 r_2$, leads to [1,2]

$$\frac{I_t}{I_i} = \frac{(1-R)^2}{1-R^2-2R\cos\phi} = \frac{1}{1+\frac{4R}{(1-R)^2}\sin^2(\phi)}. \qquad (2.2.1\text{-}3)$$

It is convenient to write Equation (2.2.1-4) in the form of

$$\frac{I_t}{I_i} = \frac{1}{1+F\sin^2(\phi)}, \qquad (2.2.1\text{-}4)$$

where the quantity

$$F = \frac{4R}{(1-R)^2}, \qquad (2.2.1\text{-}5)$$

is referred to as the finesse [2]. Similarly, the reflectance can also be written in terms of the finesse,

$$\frac{I_r}{I_i} = \frac{F\sin^2(\phi)}{1+F\sin^2(\phi)}. \qquad (2.2.1\text{-}6)$$

The transmittance and reflectance are periodic functions of ϕ with period 2π as shown in Figure 2.2.1-1. An interesting feature of the Airy function is the passband of the transmittance signal, defined by the full width at half-maximum (FWHM), decreases when the finesse F is large (the factor r is close to 1) but increases for the reflectance signal. Several demodulation systems discussed in subsequent chapters will rely on the precise locations of these spectral peaks for signal processing. Therefore, steps taken to understand and enhance the performance of the sensor will provide improvements to the performance of the signal processing system as well. Another interesting feature describing the Airy function is the contrast $C=1+F=I_{max}/I_{min}$ where I_{max} and I_{min} are the maximum and the minimum values of either Equation (2.2.1-1) or (2.2.1-2).

In a practical Fabry-Perot interferometer, many defects such as misalignment of the optical components or the poor quality of the surfaces of the fiber will degrade the constrast of the output signal. To account for these deviations, surface-defect models have been developed to calculate how a specific defect degrades the Airy function. Hernandez investigated the variation in the linewidth due to surface defects [18] and Palik concentrated on the effects that degrade the contrast [19]. The complicated intensity function that account for these defects becomes [18,19]

$$I(\nu)=\left(\frac{1}{2\pi}\right)\left(1+2\sum_{k}R^{k}\exp\left[\frac{-4\pi k}{m_L}\right]\right)\left(\exp\left[\frac{-2.35\pi k}{m_G\sqrt{\ln 2}}\right]^2\right)x$$
$$\left[\frac{\sin(2\pi k/m_C)}{(2\pi k/m_C)}\right]\left[\frac{\sin(2\pi k/m_T)}{(2\pi k/m_T)}\right]\cos\left(\frac{2\pi k\nu}{\Delta}\right), \qquad (2.2.1\text{-}8)$$

where m_L, m_G, m_C and m_T are parameters that characterize the Lorentzian lineshape, Gaussian surface roughness, curvature and tilt defects described by Hernandez and Palik.

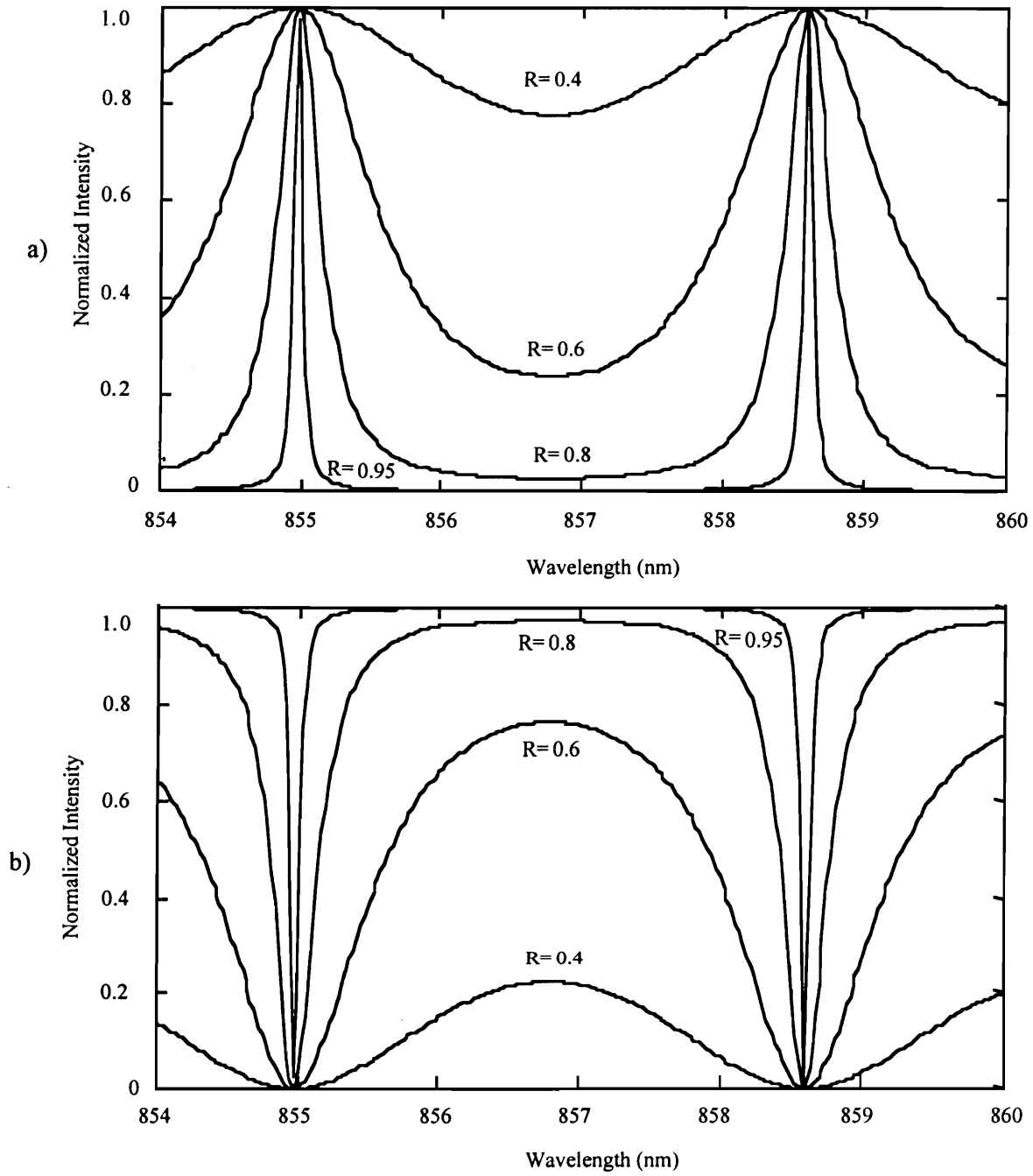

Figure 2.2-1. Plot of the a) transmittance and b) reflectance signals as a function of wavelength and reflection coefficients.

2.3 Random Phase Fluctuation

The basic interferometer concepts introduced in Section 2.1-2.2 have not taken into account the spectral width nor the coherence properties of the source but have assumed that a purely monochromatic light source with infinite coherence length is used. Random phase fluctuations of the optical source leads to spectral broadening, in turn shortening the temporal coherence of the source [2] and degrades the contrast of the interferometer. A measure of the degree of coherence of the optical source is traditionally obtained from the fringe visibility or normalized contrast, which is defined as [3],

$$V = I_{max}\text{-}I_{min}/I_{max}+I_{min} \tag{2.3-1}$$

where I_{max} and I_{min} are the maximum and minimum radiance of the interferogram produced by the interferometer, respectively.

In optical fiber communication systems, knowledge of the coherence function is required for the signal-to-noise ratio evaluation of modal noise [20]. For an interferometric fiber sensing system, the coherence behavior of the optical source affect the signal-to-noise ratio of the demodulation system. In this dissertation, we define the signal-to-noise ratio (SNR) as

$$\mathrm{SNR} = 10 \log\left[\frac{I_{max} - I_{min}}{N_{max} - N_{min}}\right], \tag{2.3-2}$$

where N_{max} and N_{min} are the noise power. In a practical fiber interferometer, surface defects can be controlled during assembly and do not vary over time. An optical source, however, will vary its operating characteristices during normal use due to thermal, back

reflections and aging effects. Since the fringe visibility of the Fabry-Perot interferometer affects the resolution and dynamic range of the sensor [21], we would like to examine how the spectral width and the temporal coherence of the source are related to the random phase fluctuation. If we assume that the electric field is stabilized in amplitude but subject to random phase modulations, then the electric field may be expressed in the form[2]

$$E(t) = E_0 \exp\left\{-j\left[2\pi\nu_0 t + \phi(t)\right]\right\}, \tag{2.3-3}$$

where E_0 is the stabilized amplitude, ν_0 is the center frequency, and $\phi(t)$ is the phase assumed to be a stationary random process. As a means for quantifying the temporal behavior of the source, we can perform a time average of the random fluctuation using the autocorrelation function [22,23]

$$G(\tau) = \left\langle E^*(t)E(t+\tau)\right\rangle = \lim_{T\to\infty}\frac{1}{2T}\int_{-T}^{T} E^*(t)E(t+\tau)dt. \tag{2.3-4}$$

In the language of optical coherence theory, the autocorrelation function $G(\tau)$ is known as the temporal coherence function [2]. A measure of the degree of coherence that is insensitive to intensity is provided by the normalized autocorrelation function of the spectrum

$$\begin{aligned} g_E(\tau) &= \left\langle E(t)E^*(t+\tau)\right\rangle \Big/ \left\langle E(t)E^*(t)\right\rangle \\ &= \left\langle \left[\exp(-j\phi(t))\right]\left[\exp(j\phi(t+\tau))\right]\right\rangle \left[\exp(j2\pi\nu_0\tau)\right], \end{aligned} \tag{2.3-5}$$

which is called the complex degree of temporal coherence [1,23]. The bracket $\langle\ \rangle$ notation denotes the time average, and the asterisk denotes the complex conjugate. In the analysis

of the statistical properties of random light, one requires that the correlation function given in Equation (2.3-5) takes a two sided exponential form

$$g_E(\tau) = \left[\exp(j2\pi\nu_0\tau)\right]\exp(-2\pi\Delta\nu|\tau|), \tag{2.3-6}$$

where $2\pi\Delta\nu$ represents a decaying function. A two side exponential function is necessary because if we take the Fourier transform of the autocorrelation $g_E(\tau)$ using the Wiener-Khinchin theorem, we see that the power spectral density must have a Lorentzian profile [1] .

$$S(\nu) = \frac{\Delta\nu/2\pi}{(\nu-\nu_0)^2 + (\Delta\nu/2)^2} \tag{2.3-7}$$

to be consistent with the lifetime broadening of stimulated emission source. Equating Equation (2.3-5) and (2.3-6) [1]

$$\left\langle\left[\exp(-j\phi(t))\right]\left[\exp(j\phi(t+\tau))\right]\right\rangle = \exp(-2\pi\Delta\nu\tau) \quad \text{for } \tau \geq 0, \tag{2.3-8}$$

we obtain an indirect expression which relates the random phase fluctuation with the spectral width. Equation (2.3-7) is used in Section 2.4 to relate the temporal coherence and spectral width of the source to the fringe visibility and output response of the Fabry-Perot interferometer.

2.4 Temporal Coherence Effects on a Fabry-Perot Interferometer

In this section we consider how the fringe visibility and output response of the Fabry-Perot interferometer is dependent on the coherence length of the radiation source while ignoring the effect due to absorption. Note that for gold sputtered films operating in the

wavelength region between 700-1100 nanometers, the absorption of the reflecting surfaces is minimal and may be neglected. However, if the optical source operates below 700 nanometer, significant absorption will occur. Note that absorption tends to lower the transmittance and reflectance but not the finesse nor fringe visibility [19]. Figure 2.4-1 illustrates the spectral reflectances for a number of sputtered metal films under ideal conditions. Although silver appears to provide a broad operating range, oxidation would prevent its long-term use. Aluminum thin-films would be more suitable but the absorption is not uniform as function of wavelength.

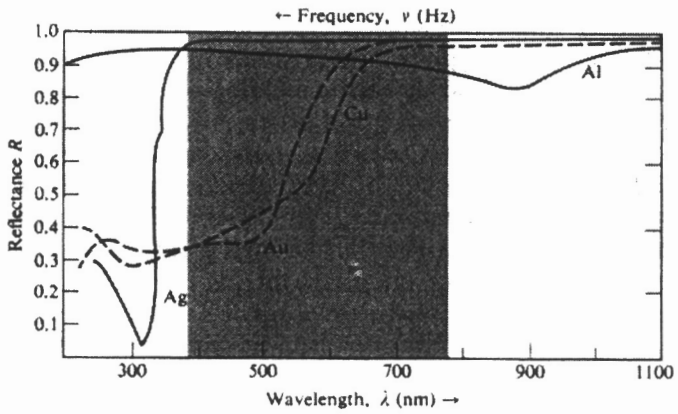

Figure 2.4-1. Reflectance versus wavelength for metallic thin-films [1].

Our treatment of temporal coherence follows in part that given by Wolf [1], Saleh [2] and Mandrel [24]. Previous works mainly considered the interference of two fields $E_1(t)$ and $E_2(t)$ in a double-beam type interferometer. Here, we adopt the approaches illustrated by Wolf, Saleh and Mandrel to consider the effect of multiple reflections and interference. This will allow us to obtain an expression relating the temporal coherence to the transmission output of the extrinsic Fabry-Perot interferometer as shown by Ohtsuka[25].

To simplify our analysis, we specify that the fiber endfaces have the same optical quality. As defined in Section 2.2.1, the amplitudes of the transmittances and reflectances are denoted as r_i and t_i (i=1,2 for the two interfaces), and the power transmittance and reflectance are given by $T=t_1t_2$ and $R=r_1r_2$, respectively. If the mirrored endfaces are separated by *d*, the round-trip travel time for the confined optical wave is $t_r=2nd/c$. As a result of multiple repetitive reflections inside the interferometer due to the high reflecting endfaces, the total optical wave field E(t), transmitted through the interferometer, may be expressed in a series formula. Referring to Equation (2.0-3) for the expression of the electric field, the optical wave field emerging from the Fabry-Perot cavity may be expressed as [1,2]

$$E(t) = E_0 t_1 t_2 \exp j[2\pi\nu_0 t + \phi(t)] + E_0 t_1 t_2 r_1 r_2 \exp j[2\pi\nu_0 (t - t_r) + \phi(t - t_r)] + \ldots + E_0 t_1 t_2 r_1 r_2^{2(m-1)} \exp j[2\pi\nu_0 (t - (m-1)t_r) + \phi(t - (m-1)t_r)] + \ldots \quad (2.4\text{-}1)$$

where *m* is an integer. We can express the optical wave field of Equation (2.4-1) as a series representation using the power transmittance and reflectance as [22,23,26]

$$E(t) = E_0 T \exp\left[j\left(2\pi\nu_0 t\right)\right]\sum_{m=1}^{\infty} R^{(m-1)} \exp\left[-2\pi j\nu_0\left(m-1\right)t_r\right]\exp\left\{j\phi\left[t-\left(m-1\right)t_r\right]\right\}. \qquad (2.4\text{-}2)$$

The resulting irradiance measured over some finite time interval is obtained by taking the time-average of Equation (2.4-2) [22,23]

$$I(t) = \left\langle \left|E(t)\right|^2 \right\rangle = T^2\left|\overline{E}_0\right|^2 \sum_{m=1}^{\infty}\sum_{n=1}^{\infty} R^{(m-1)}R^{(n-1)} \exp\left[2\pi j\nu_0 t_r\left(n-m\right)\right]$$
$$\cdot\ \exp j\phi\left[t-\left(m-1\right)t_r\right]\exp\left\{-j\phi\left[t-\left(n-1\right)t_r\right]\right\}, \qquad (2.4\text{-}3)$$

which may be divided into three summations and each considered separately,

$$I(t) = T^2 I_0\left(\sum_{m=n=1}^{\infty} + \sum_{m>n}^{\infty} + \sum_{m<n}^{\infty}\right), \qquad (2.4\text{-}4)$$

where $I_0 = \left|E_0\right|^2$. Knowing that the reflectance $0 < R < 1$, the first summation term simply converges to [26]

$$\sum_{m=n=1}^{\infty} = \sum_{m=1}^{\infty} R^{2(m-1)} = \frac{1}{\left(1-R^2\right)}. \qquad (2.4\text{-}5)$$

The second summation is calculated as [22,23]

$$\sum_{m>n}^{\infty} = \sum_{m=2}^{\infty}\sum_{n=1}^{\infty} R^{(m+n+2)} \exp\left[-2\pi j\nu_0 t_r\left(m-n\right)\right]$$
$$\exp j\phi\left[t-\left(m-1\right)t_r\right]\exp\left\{-j\phi\left[t-\left(n-1\right)t_r\right]\right\}. \qquad (2.4\text{-}6a)$$

Making the substitution m-n=p (p=1, 2, ...), Equation (2.4-6a) is converted to [1,2,22,23]

$$\sum_{m>n}^{\infty} = \sum_{p=1}^{\infty}\sum_{n=1}^{\infty} R^{2(n-1)}R^{p}\exp\left[-2\pi j\nu_0 t_r p\right] \exp\left\{j\phi\left[t-(n-1)t_r - t_r p\right]\right\}\exp\left\{-j\phi\left[t-(n-1)t_r\right]\right\}. \tag{2.4-6b}$$

Recalling that the optical wave field has been assumed to be stationary in time for the present situation, we can shift the origin of the time scale so that a replacement of [t-(n-1)t_r] with t gives [22-24]

$$\sum_{m>n}^{\infty} = \sum_{p=1}^{\infty}\sum_{n=1}^{\infty} R^{2(n-1)}R^{p}\exp\left[-2\pi j\nu_0 t_r p\right]\left\langle \exp j\phi\left[t-t_r p\right]\exp\left(-j\phi(t)\right)\right\rangle. \tag{2.4-6c}$$

Following the procedures outlined above, the third summation becomes

$$\sum_{m<n}^{\infty} = \sum_{p=1}^{\infty}\sum_{m=1}^{\infty} R^{2(m-1)}R^{p}\exp\left[2\pi j\nu_0 t_r p\right]\left\langle \exp\left[-j\phi\left(t-pt_r\right)\right]\exp\left[j\phi(t)\right]\right\rangle. \tag{2.4-7}$$

We see that the time-averaged components of Eqns. (2.4-6b) and (2.4-6c) resemble the autocorrelated signals where the term 'pt_r' corresponds to τ in Equation (2.3-2). Under the condition that the optical wave field is stationary as shown by Equation (2.3-4), the time-averaged part of Equation (2.4-6c) reduces to [22,23]

$$\left\langle \exp\left[j\phi\left(t-pt_r\right)\right]\exp\left[-j\phi(t)\right]\right\rangle = \exp(-2\pi\Delta\nu pt_r). \tag{2.4-8}$$

The use of the autocorrelation function [22,23] in Equation (2.4-8) enables us to simplify Equation (2.4-6c) so that

$$\sum_{m>n}^{\infty} = \sum_{n=1}^{\infty} R^{2(n-1)} \sum_{p=1}^{\infty} \left[R \exp\left(-2\pi j \nu_0 t_r - 2\pi \Delta\nu t_r\right) \right]^p . \qquad (2.4\text{-}9)$$

Again knowing that 0<R<1, the geometric series in (2.4-9) also converges to a finite sum[26]

$$\sum_{m>n}^{\infty} = \left[\frac{1}{1-R^2} \right] \frac{R \exp\left(-2\pi j \nu_0 t_r - 2\pi \Delta\nu t_r\right)}{1 - R \exp\left(-2\pi j \nu_0 t_r - 2\pi \Delta\nu t_r\right)} . \qquad (2.4\text{-}10)$$

Similarly, Equation (2.5-7) converges to [26]

$$\sum_{m<n}^{\infty} = \left[\frac{1}{1-R^2} \right] \frac{R \exp\left(2\pi j \nu_0 t_r - 2\pi \Delta\nu t_r\right)}{1 - R \exp\left(2\pi j \nu_0 t_r - 2\pi \Delta\nu t_r\right)} . \qquad (2.4\text{-}11)$$

Substitution of Eqns. (2.4-5), (2.4-10) and (2.4-11) into Equation (2.4-4) finally yields the transmitted [25]

$$\frac{I}{I_0} = \frac{T^2 \left[1 - R^2 \exp\left(-4\pi \Delta\nu t_r\right) \right]}{\left[1 - R^2 \right] \left\{ \left[1 - R \exp(-2\pi \Delta\nu t_r) \right]^2 + 4R \sin^2(\pi \nu_0 t_r) \exp(-2\pi \Delta\nu t_r) \right\}} . \qquad (2.4\text{-}12)$$

Since the coherence length of a radiation source is $L_c = c/\Delta\nu = \lambda_0^2 / \Delta\lambda$, we have $\Delta\nu t_r = d / L_c$ [3]. In view of the relation $T^2 = (1\text{-}R)^2$, Equation (2.5-12) may be rearranged into the following convenient form [1,2]

$$\frac{I}{I_0} = \frac{A}{1 + B \sin^2 \theta}, \qquad (2.4\text{-}13)$$

where

$$A = \left(\frac{1-R}{1+R}\right)\left[\frac{1+R\exp(-2\pi dL_c)}{1-R\exp(-2\pi dL_c)}\right], \tag{2.4-14}$$

$$B = \frac{4R\exp(-2\pi dL_c)}{\left[1-R\exp(-2\pi dL_c)\right]^2}, \tag{2.4-15}$$

$$\theta = \pi v_o t_r = kd, \tag{2.4-16}$$

and $k = 2\pi d/\lambda$ is the optical wavenumber in the interferometer. In the limit for which the coherence length is infinitely large ($\lim_{L_c\to\infty} A = 1$ and $\lim_{L_c\to\infty} B = 4R/(1-R)^2$), Equation (2.4-12) reduces to the conventional formula for the interferometer without absorption as shown before in Equation (2.2.2-4) [1,2]. The expression shown in Equation (2.2.2-4) does not properly take into account the coherence effect of the optical source. By expanding the reflectance function of Equation (2.4-12) to incorporate the spectral width of the input source, we observe in Figure 2.4-2 that the actual signal-to-noise ratio is dependent on the fringe visibility in addition to the input optical power. The graphs correspond to a variation in visibility associated with changes in the spectral width of the source. In Chapter 4 we will use this result to analyze how the fringe visibility or the signal-to-noise ratio affect the performance of the signal processing algorithm.

2.5 Limitations of the Monochromatic Interferometric Sensors

The extrinsic Fabry-Perot interferometric (EFPI) sensor measures the various external environmental parameters that result in air-gap displacement changes by relating the effect of these parameters to the gap between the two fibers aligned in the alignment tube. The parameter of interest, such as strain, is converted by the sensor into a displacement between the two fibers which is determined by the signal processing system. The EFPI

sensor output intensity as shown by Equation (2.1.2-3) is sinusoidal as a function of displacement when probed with a continuous wave, monochromatic light source [15,16]. To find the magnitude of the perturbation, either the EFPI sensor has to be maintained at the quiescent point (Q-point) or if the perturbation is large, a fringe counting technique has to be employed [27]. The EFPI sensor is extremely sensitive if it is operated at the Q-point but the sensitivity reduces dramatically if the sensor drifts a quarter wavelength away. Stabilizing the sensor at the Q-point using either wavelength tuning or thermal compensation is extremely difficult, and hence not typically done [27].

The periodicity of the output also causes two related problems when interpreting the sensor information. First, a sinusoidal transfer function for mapping the desired measurement signal is identical for increasing and decreasing measurands. That is, for an increasing strain, the output of the sensor would be exactly the same as the output when the strain is decreasing, from the same starting point. A mistaken calculation of the change in direction can lead to gross strain measurement errors [28]. Second, if the electrical power is interrupted in the phase demodulation system, the initial phase of the interferometer used by an electronic fringe counter to establish a reference signal is lost [7,8,28]. The directional problem associated with the EFPI can be solved using of quadrature-phase shifted (QPS) sensor [15]. A QPS sensor has two signals approximately 90° out-of-phase with one another. By monitoring the phase change between the quadrature shifted signal, one can determine when a change in the direction of the applied perturbation has occurred. Although this modified sensor configuration gives directional information, in practice, it is difficult to construct two adjacent Fabry-Perot cavities that are precisely phase shifted by 90°. Moreover, it is difficult to isolate a phase change resulting from transverse, torsional strain or bends from an actual change in direction. In order to resolve these difficulties, new demodulation and signal processing techniques have been developed for this dissertation.

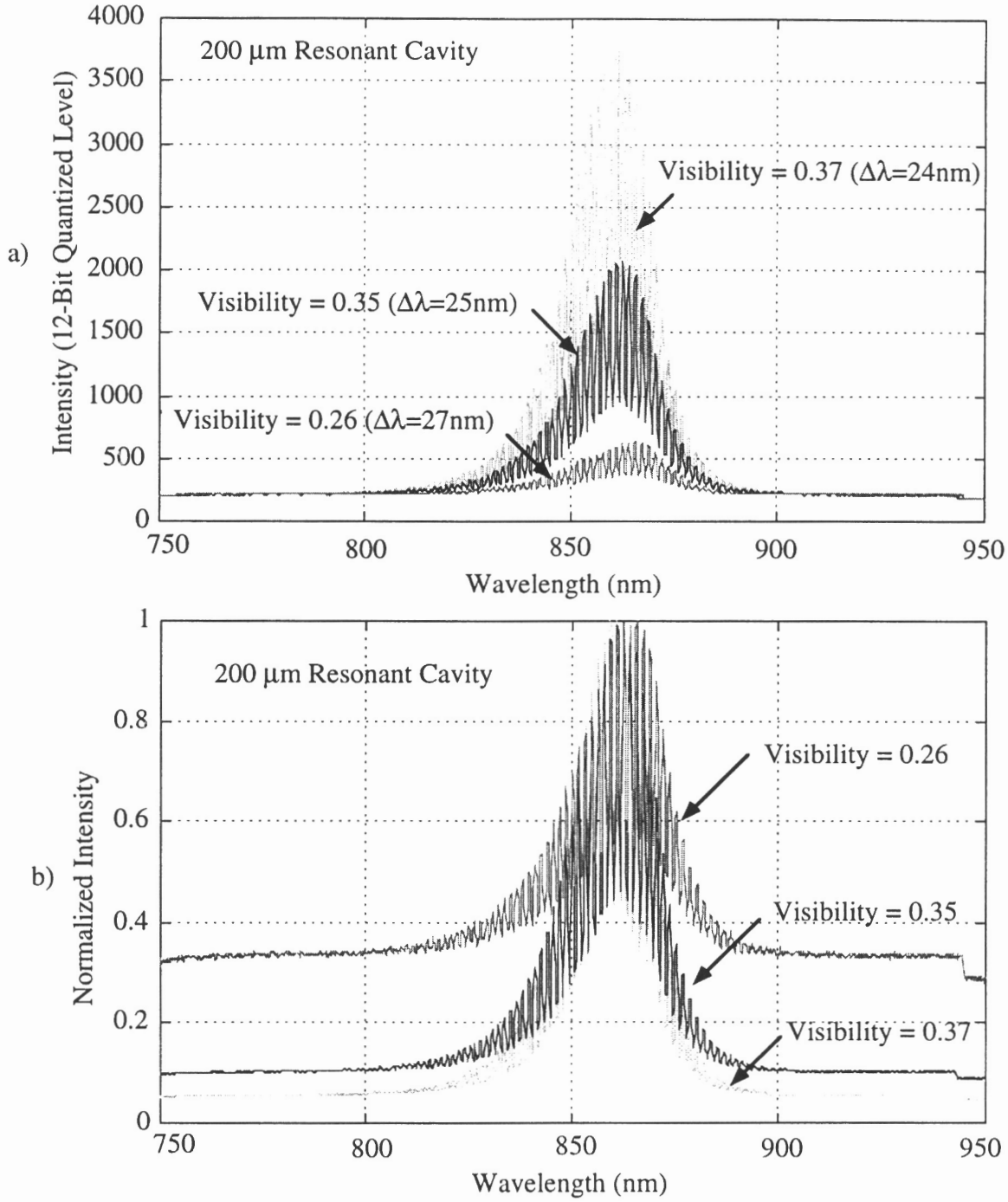

Figure 2.4-2. Optical fiber Fabry-Perot interference patterns produced by partially coherent light of varying spectral width. The spectral width is modified by changing the current supplied to the source.

3. Optical Demodulation Techniques

The main focus of this chapter is to discuss techniques that may be used to recover the optical signal encoded by a remote interferometric sensor. Demodulation systems based on novel optical cross-correlation techniques and classical Fourier transform spectroscopy are investigated. Before an effective signal processing algorithm can be developed, individual demodulation systems must be accurately characterized to assess the limitations and the practical issues involved in implementing the instrumentation for field applications. These assessment tasks were conducted so that we can develop a demodulation system having the optimal frequency response, resolution, and dynamic range yet is practical to implement. Figure 3.0-1 briefly summarizes the classification of some of the optical cross-correlators that are discussed in this chapter.

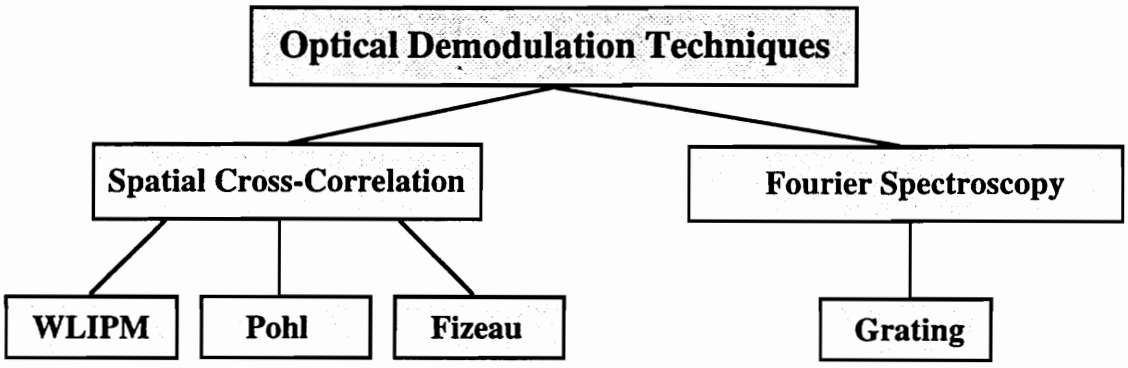

Figure 3.0-1. Summary of optical cross-correlation demodulation techniques.

3.1 White Light Optical Cross-Correlator

The technique of white-light interferometric path matching (WLIPM) is based on the principle that if the path difference of a single interferometer is larger than the coherence length of the source, then the two beams of light generated in the interferometer will be unable to generate interference fringes. However, if a second interferometer is included in the configuration so that its path difference matches that of the first interferometer, the overall path between the two beams of light will have a difference less than the coherence of the source, and the beams will interfere [7,8,9,10]. The second interferometer is used to extract information encoded by the sensing interferometer. A detailed description of several different WLIPM configurations are provided in the following sections.

3.1.1 Spatial Correlation

The WLIPM sensor demodulation system can be operated in either the reflective or transmissive mode. The reflective and transmissive configurations are shown in Figure 3.1-1(a) and (b). The objective of the WLIPM approach is to utilize an output interferometer such as Michelson or low-finesse Fabry-Perot scanning interferometer to correlate the cavity lengths of remotely located EFPI sensors as shown in Figure 3.1-1. When the coherence matching condition occurs (the optical path difference of the sensing interferometer matches the decoding interferometer) [7,8], an interference pattern (interferogram) is generated as shown in Figure 3.1-2. The peak of the envelop shown in Figure 3.1-2 indicates the position where the complementary interferometers are in complete coherence. The interferogram is obtained by synchronizing the oscilloscope to the start of the scan. Synchronization allows us to correlate the time axis with the displacement of the scanning Fabry-Perot cross-correlator [29].

Although we have demonstrated the WLIPM demodulation technique, the main drawback in using a mechanically scanned device is its slow response. Thus, it may be inadequate for applications that require a high frequency response such as vibration monitoring, or acoustic transducers. In spite of the slow frequency response, white light interferometry allows optical fiber sensors to be easily multiplexed. Figure 3.1-1 shows two multiplexing schemes. In either case, each sensor in the array must be set at a different initial gap to prevent cross-interference between individual sensors. Decoding a multiplexed sensor array is accomplished by a single scanning output cross-correlating interferometer. As the scanning cross-correlator approaches the optical path length difference of each sensor, an interferogram is generated.

In addition to its demultiplexing capability, another advantage of the WLIPM decoder is its extremely high resolving capability, limited by the sampling rate of the detection electronics. Figure 3.1-2 shows that the time resolution on the x-axis can be improved by capturing the interferogram at a higher sampling rate. We can improve the displacement resolution by increasing the sampling rate of the detection electronics. The displacement resolution of the spatial cross-correlator is obtained from the following relation

$$\delta d = \Delta t \, d_{scan}, \tag{3.1-1}$$

where Δt is the sampling rate and d_{scan} is the maximum scanning distance of the cross-correlator. Since we are correlating the displacement of the resonant cavity to a timing interval, the accuracy of this type of demodulation system is highly dependent on how well one can maintain the constant scanning rate of the output interferometer. The displacement estimation also depends on the proper synchronization of the detection electronics with the cross-correlator.

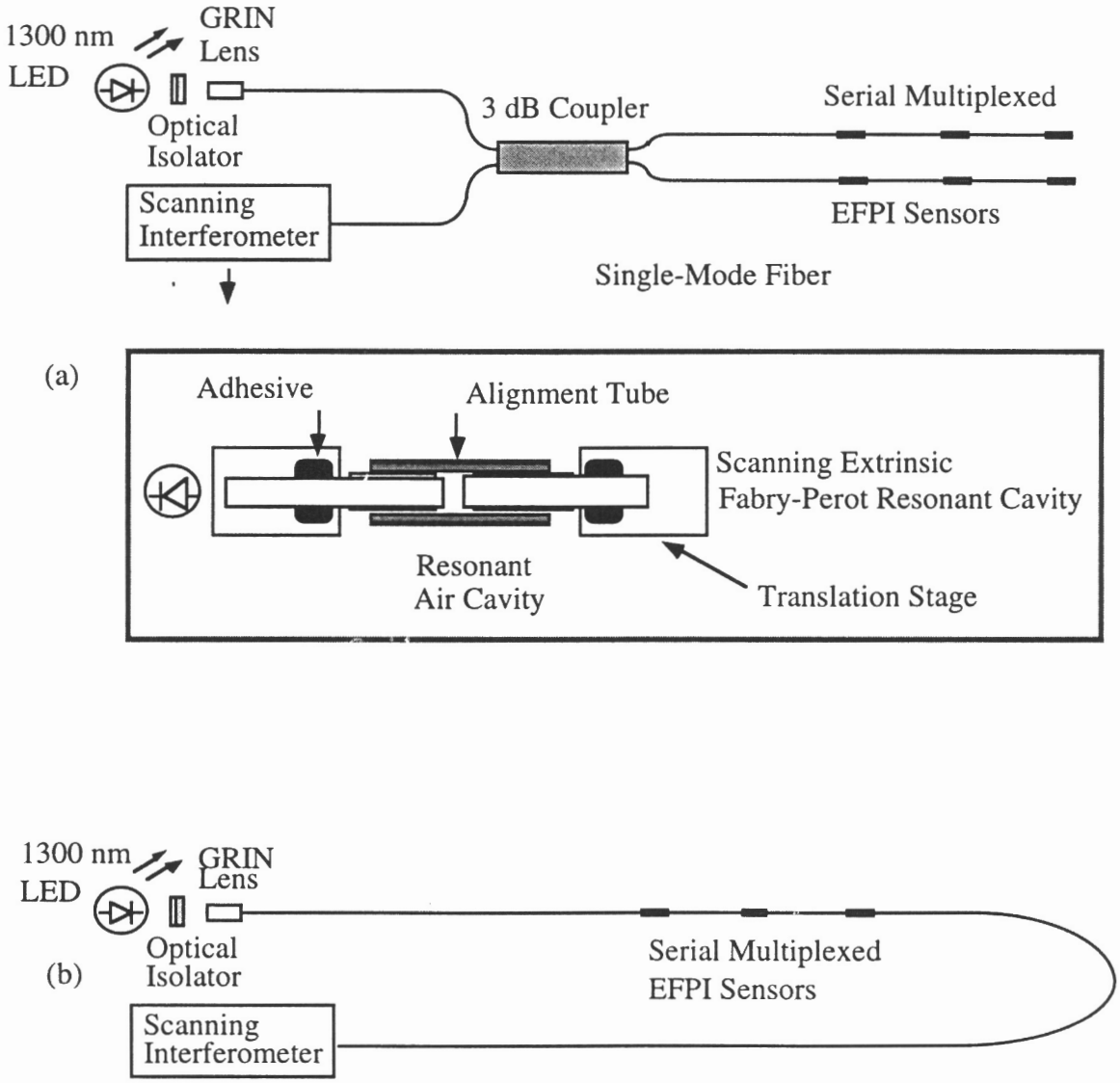

Figure 3.1-1. White light interferometry path matching topologies a) reflective and b) transmissive configurations [29].

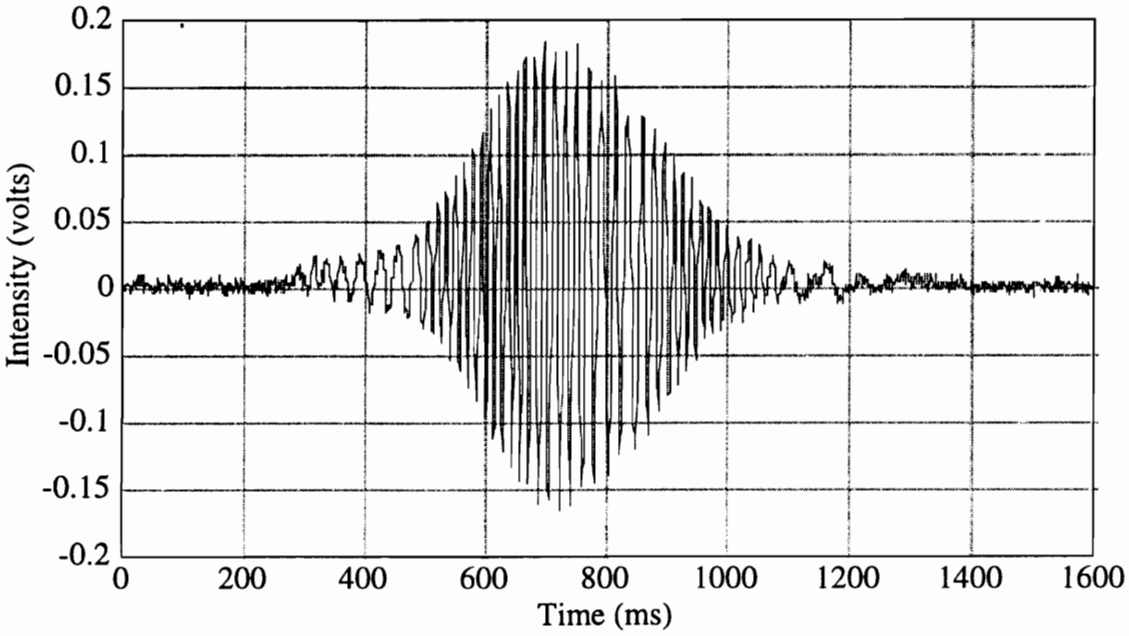

Figure 3.1-2. Output of white light path-matched interferometer [29].

3.2 Fizeau Cross-Correlator

One innovative approach that can be used to improve the frequency response of the cross-correlator is depicted in Figure 3.2-1(b). The Fizeau cross-correlating technique proposed by Belleville and Duplain employs a low-finesse wedge interferometric demodulator and a linear charge coupled device (CCD) array to capture the returned spectrum [11]. The frequency response of this type of demodulation system depends on the electronic scanning speed of the CCD array as opposed to a mechanical scanning device. The length of the Fabry-Perot cavity is determined by measuring the light spectrum $X(\lambda)$ transmitted or reflected by the sensor, and is accomplished by cross-correlating the measured spectrum with the simplified transmittance function $T(\lambda,d)$ of a Fabry-Perot. The cross-correlation coefficient at a given distance *d* is evaluated with the following relation [11],

$$C(d) = \frac{1}{M}\sum_{n=0}^{M-1} X(\lambda_0 + n\Delta\lambda)\frac{1}{1+F\sin^2[\frac{2\pi d}{\lambda_0 + n\Delta\lambda}]} . \qquad (3.2\text{-}1)$$

The Fizeau interferometer acts as an optical cross-correlator whose cavity length varies spatially along the length of the wedge. Therefore, the interferometric pattern resulting from gap correlation has a spatial dependence as opposed to the temporal dependence of the scanning EFPI. Spatially monitoring the location of the fringe pattern indicates the gap length corresponding to the sensing EFPI. In other words, the light intensity transmitted through a Fabry-Perot sensor with a cavity length of *d* will be maximally transmitted by the Fizeau interferometer exactly at the position where the distance

between the flat glass slides equals *d*. The interferogram captured on the CCD array is shown in Figure 3.2-2.

The highest peak of the interferogram corresponds to the location where the Fizeau and Fabry-Perot cavity lengths are matched. As one moves away from this central position, the path-matched condition between the sensor and the cross correlator gradually fades, thereby reducing the observed fringe visibility, or fringe contrast. This phenomenon thus enables the signal processing hardware to determine the precise location on the CCD array having the highest intensity peak [11]. A simple vector sorting routine may be implemented to perform this calculation. The theoretical displacement resolution of this demodulation system is simply

$$\delta d = \frac{a}{n \sin\left(\frac{\gamma}{2}\right)}, \tag{3.2-1}$$

where *a* is the width of the Fizeau wedge, *n* is the number of elements in the CCD array, and γ is the angle of the wedge. It is apparent from Figure 3.2-1 that the dynamic range is preset by the angle of the Fizeau wedge and the length of the CCD array (L_{CCD})

$$d_{max} = \frac{a L_{CCD}}{\sin\left(\frac{\gamma}{2}\right)}. \tag{3.2-2}$$

Equating Equation (3.2-1) with (3.2-2), we see that the resolution is inversely related to the dynamic range. The inverse relationship between resolution and dynamic range is the major disadvantage of the Fizeau cross-correlator since it is not possible to simultaneously obtain high resolution and wide dynamic range.

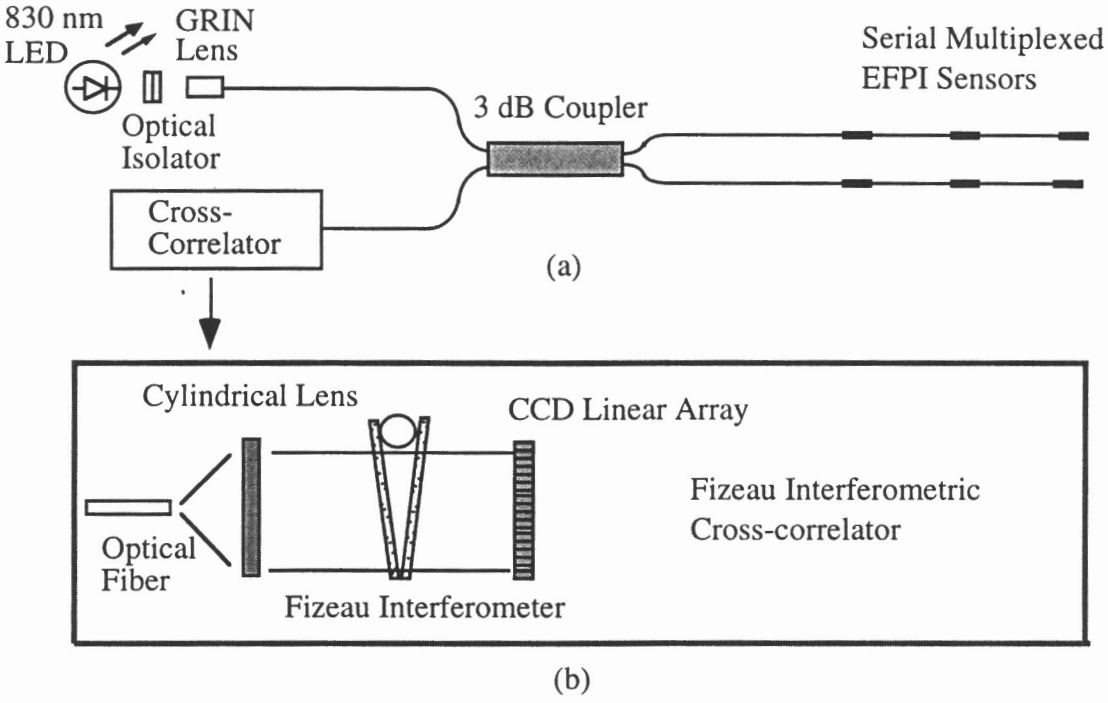

Figure 3.2-1. White light interferometry path matching topologies using a) scanning Fabry-Perot interferometer and b) Fizeau interferometric cross-correlator.

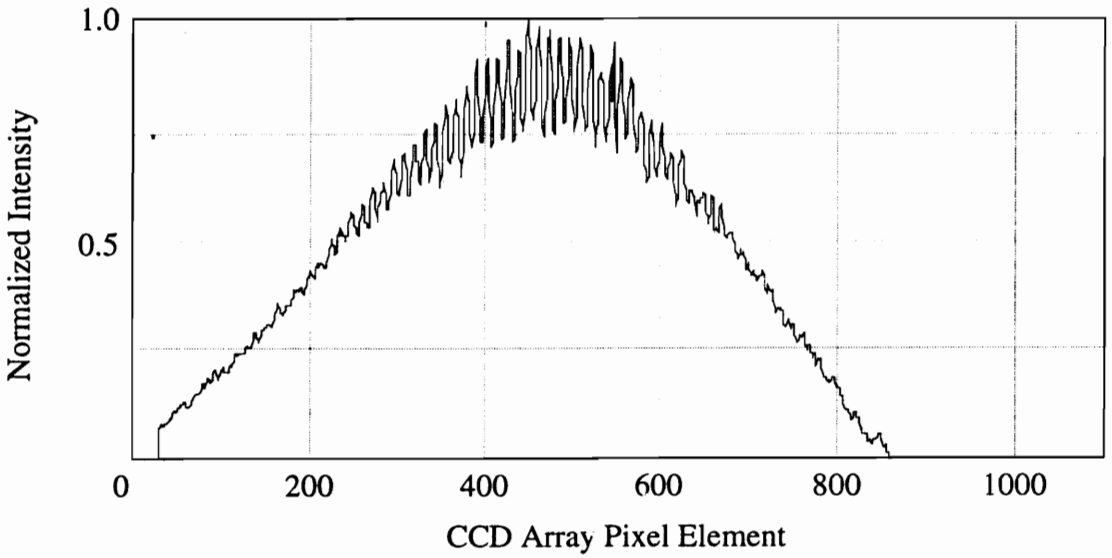

Figure 3.2-2. Output of CCD array illustrating typical path matching fringes resulting from using Fizeau cross correlation techniques.

3.3 Pohl Interferometric Demodulator

The principle of the Pohl interferometer is based on the optical path difference (OPD) that results from reflections off the front and back surface of the plate. Light incident at an angle on the parallel plate will reflect off both the front and back surface of the plate and have a phase difference which is dependent upon the incident angle of the light and the material and thickness of the plate. The phase difference is given by [30]

$$\Delta\phi = \frac{4\pi t \cos(\alpha)}{\lambda}, \tag{3.3-1}$$

where $\Delta\phi$ = phase difference, t = plate thickness, and α is the reflection angle from the back surface and is simply given by Snell's law as [30]

$$\alpha = \sin^{-1}\left(\frac{\sin\theta}{n}\right), \tag{3.3-2}$$

where θ is the angle of incident on the plate and *n* is the refractive index of the plate.

If the light incident upon the plate is collimated or if the angle of incident is normal to the parallel plate, the phase difference between front and back reflections does not vary spatially over the length of the plate. If, however, the light incident upon the plate is diverging as it is upon exiting an optical fiber, there will be different angles of incidence at different locations along the plate and hence spatial fringes will be observed. This concept is illustrated in Figure 3.3-1 [30].

If the plate is illuminated with a long coherence source such as a laser, the fringes described above should be visible in the far-field pattern reflected from the parallel plate. These fringes were observed upon illumination from a laser, and are shown schematically in Figure 3.3-2. Note that the periodicity of the interferogram varies due to the dependence of the OPD on the incident angle.

An experimentally measured section of the interferogram illuminated by a laser is shown in Figure 3.3-3. A small portion of the reflected signal was transmitted through a cylindrical lens and focused onto a CCD array. Since only a small portion of the entire interferogram was monitored, the fringes appear to be evenly spaced. The interferogram shown in Figure 3.3-3 represents the transfer function for a Helium Neon (HeNe) laser. The twelve fringes represent an overall OPD dynamic range of 7.5 micrometers over the length of the CCD array. Using a typical CCD array that has 1024 pixel elements would result in a spectral resolution of 7 nanometers. If the wavelength was to change, then the periodicity of the fringes would change. Therefore, by taking a fast Fourier transform (FFT) of the signal incident upon the CCD detector, the wavelength can be correlated to the spectral peak. Changes in wavelength and modulation frequency can also be detected by using an electronic phase-locked loop to determine the phase shift occurring between a carrier signal and the input optical signal [31].

Since the Pohl interferometer converts wavelength encoded information into a frequency modulated optical signal, the interrogation system is highly immune to source intensity drifts and other intensity based errors. We should note that the spatial frequency modulation only occurs when the coherence length of the optical source is greater than the optical path length difference produced by the parallel plate.

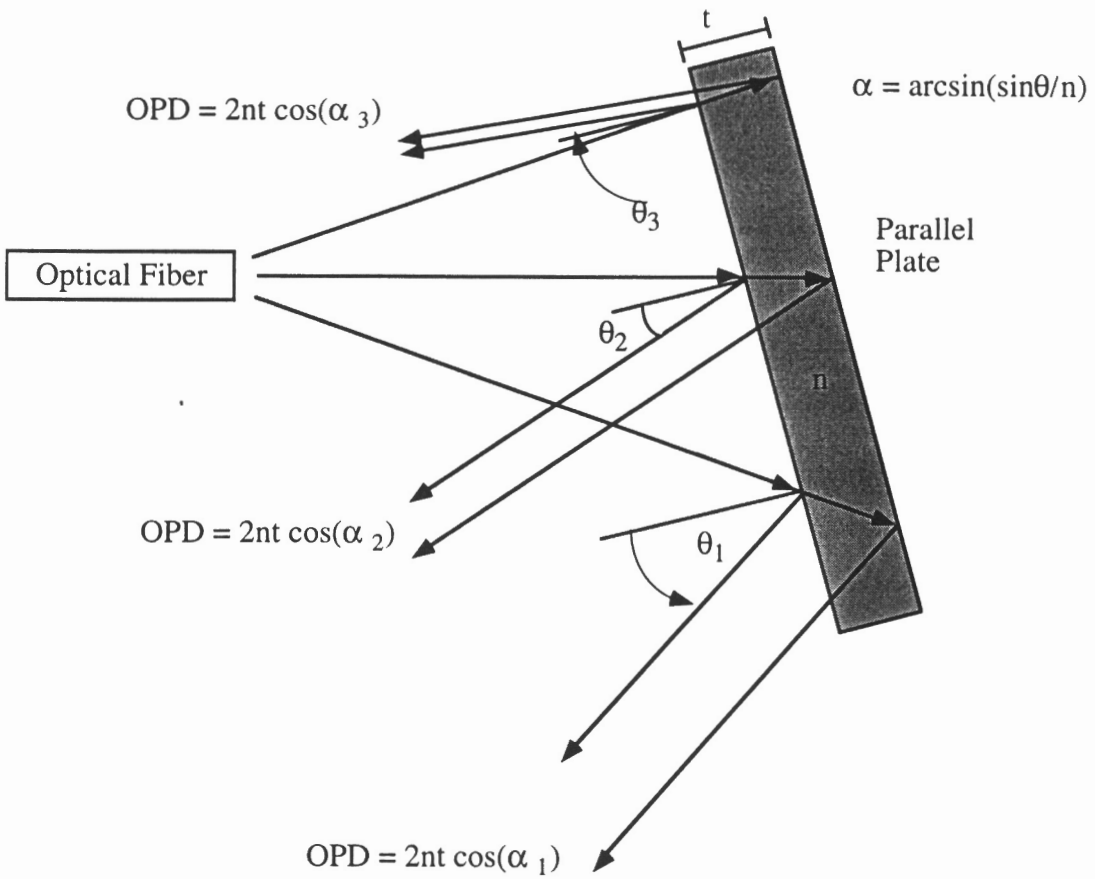

Figure 3.3-1. Schematic illustrating path differences resulting from a diverging light beam incident upon an angled parallel plate.

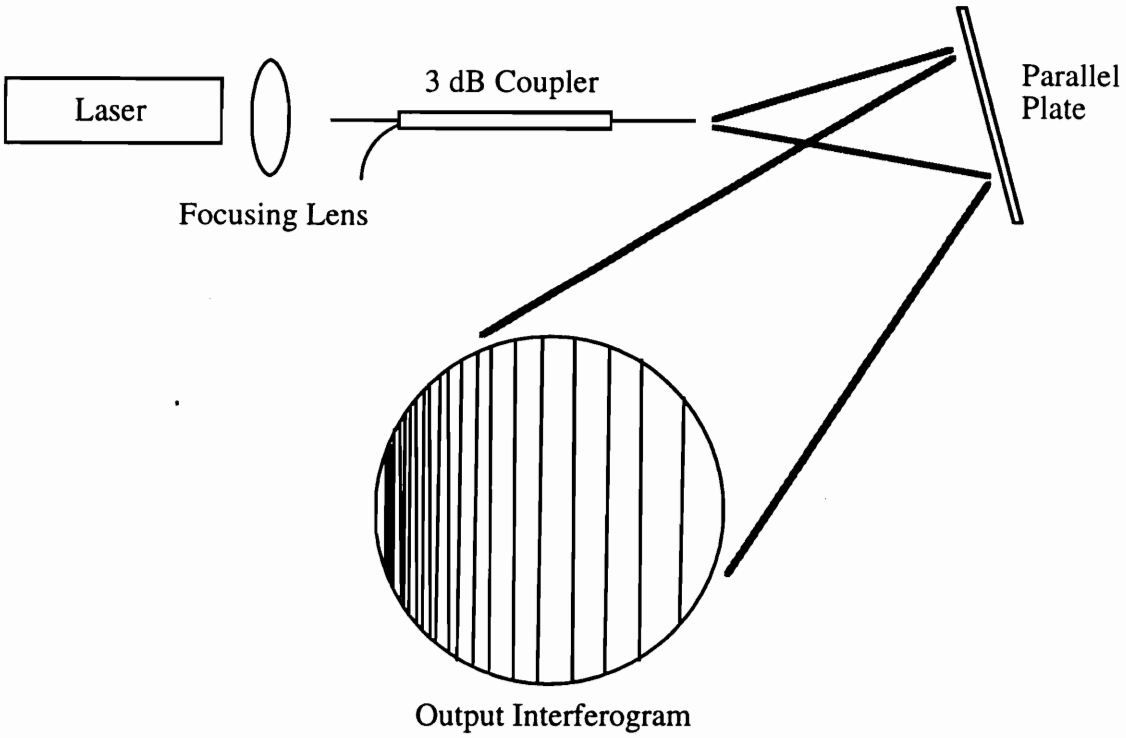

Figure 3.3-2. Interferogram of a Fizeau parallel plate interferometer illuminated by a diverging beam.

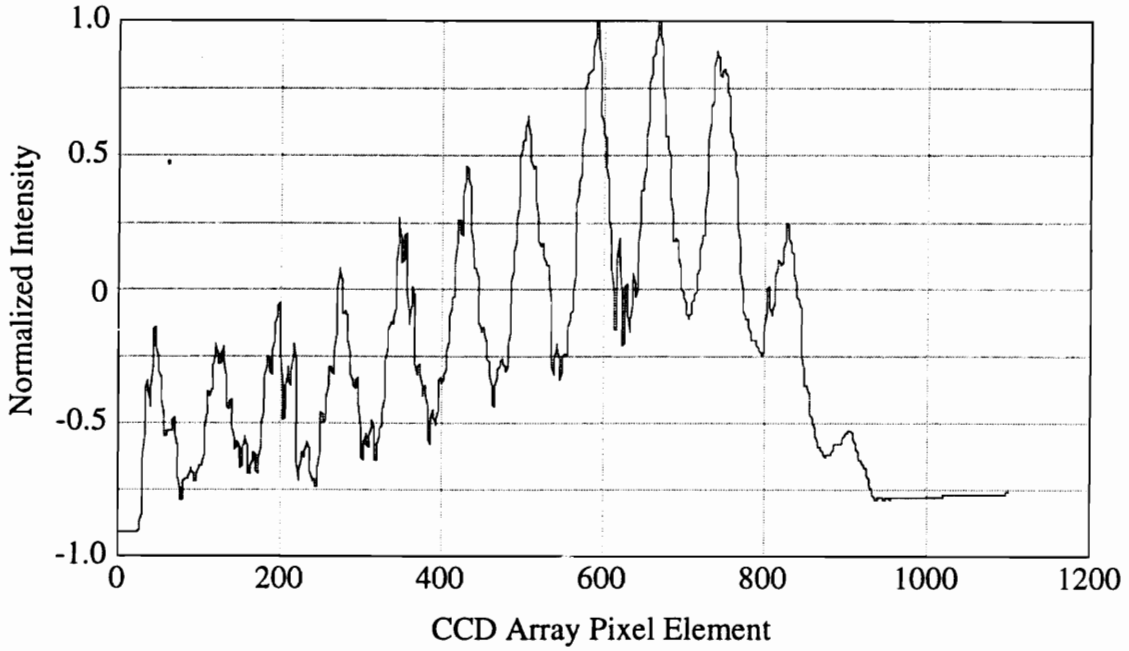

Figure 3.3-3. Interferogram from a Fizeau parallel plate demodulator for a HeNe laser operating at 632.8 nm.

3.4 Pohl Cross-Correlator

The Pohl interferometer discussed above can be effectively used as a cross-correlator for the Fabry-Perot fiber sensor. Here a broadband, short coherence source is used to obtain fringes when the total optical path difference in the system is within the source coherence length. This situation arises when the EFPI air gap matches the OPD generated by a specific divergence angle incident on the parallel plate. Therefore, as the gap changes, the corresponding angle must change and the fringe envelope resulting from correlation will shift back and forth across the CCD array. By tracking the position of the intensity peak incident on the CCD array, the EFPI displacement gap can be accurately monitored. The experimental setup for this technique is shown in Figure 3.4-1. For *n* number of pixel elements, the displacement resolution for the Pohl decoder is related to the thickness of the parallel plate and transmission angle to the CCD array [30]

$$\delta d = \frac{t \cos(\alpha)}{n}. \tag{3.4-1}$$

The resolution obtained from Equation (3.4-1) can be further improved by using more advanced central fringe identification schemes such as the centroid interpolation technique described in Section 4.2.3. The advantage of the Pohl interferometer is its simplicity in construction and operation. As a cross-correlator, the Pohl interferometer used in this configuration does not produce spatially varying frequency modulated signal, thus spectral analysis using the Fourier transform is not suitable for this application. The most direct signal processing method is simply to record the pixel position of the fringe having the highest amplitude.

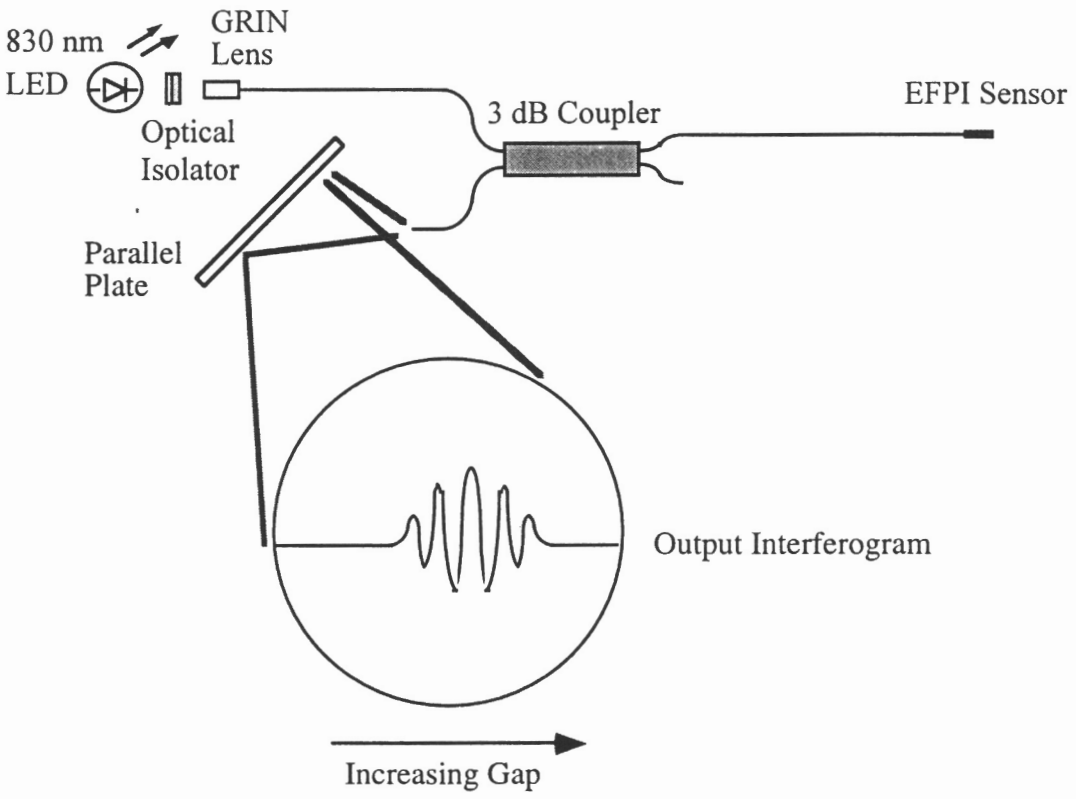

Figure 3.4-1. Path matching configuration using a Pohl parallel plate cross-correlator.

3.5 Dispersive Grating Spectroscopy

Because the Fabry-Perot cavity is uniquely specified by the transmittance function, an optical spectrum analyzer or any equivalent instrument such as grating, Fabry-Perot or Michelson spectrometer can also be used to determine the phase difference between the various wavelength components. The more common spectrometer scans the spectrum by diffracting the incoming optical signal onto a photodetector by means of a mechanically rotated diffraction grating. This method produces a digitized signal that is uniformly sampled in wavelength [32]. Another approach taken in designing a spectrometer is to diffract the entire spectrum onto a stationary CCD array via a grating [33]. In this scheme the incoming spectrum is not uniformly sampled since the diffracted beam incident on the CCD array is not normal to the imaging surface. The nonuniform sampling behavior is an important issue that will be addressed in Chapter 4.

In a demodulation system that utilizes a grating-based spectrometer, the resolution is governed by the periodicity of the diffraction grating, its diffraction characteristics, and the separation distance between the CCD, the geometry and pixel size of the CCD element. The spectrometer resolution is also dependent on the quality of the grating, the blazed angle, and pitch. Assuming that we have uniform wavelength sampling, the resolution of the spectrometer may be estimated from [34]

$$\delta\lambda = \frac{\Delta\lambda}{n}, \tag{3.5-1}$$

where n is the number of pixels in the CCD array and $\Delta\lambda$ is the passband of the spectrometer. The actual displacement resolution depends on the type of signal processing used to estimate the cavity length from the spectral encoded information.

In summary, we have demonstrated in this chapter several viable approaches for demodulating optical fiber-based interferometric sensors. However, due to practical implementation constraints, we will mainly use the spectrometer for the demodulation system. Utilizing any of the demodulation schemes described in Sections 3.1 through 3.4 would require a considerable hardware development effort in order to obtain a calibrated measurement system. In this dissertation, we have elected to use a calibrated spectrum analyzer so that we could allocate some of the research efforts to developing a viable signal processing algorithm and investigate the distortion effects that impose significant impact on the performance of the processing algorithm. A summary of the theoretical displacement/spectral resolution for each respective demodulation system discussed in this chapter is given in Table 3.5-1.

Table 3.5-1. Demodulation techniques and theoretical displacement/spectral resolution.

Demodulation Technique	**Displacement/Spectral Resolution**
WLIPM	$\delta d = \Delta t \, d_{scan}$
Fizeau Cross-Correlator	$\delta d = a \Big/ n \sin\left(\frac{\gamma}{2}\right)$
Pohl Cross-Correlator	$\delta d = \frac{t \cos(\alpha)}{n}$
Fourier Spectroscopy	$\delta\lambda = \frac{\Delta\lambda}{n}$

4. Digital Signal Processing Techniques

Digital signal processing is becoming a ubiquitous tool for many disciplines of engineering. It is currently undergoing a period of rapid growth caused by recent advances in VLSI technology, especially in the areas of optimal signal processing, namely, real-time adaptive signal processing, eigenvector methods of spectrum estimation, and parallel processor implementations of optimum filtering and prediction algorithms [35]. This chapter describes two digital signal processing techniques tailored specifically to process the wavelength encoded optical signals from the interferometer. The first technique employs a simple peak wavelength tracking approach to estimate the displacement of the Fabry-Perot interferometer. The second signal processing approach is an adaptive spectral estimation technique that makes extensive use of the Fourier transforms. For both techniques a spectrum analyzer was used to decode the optical signal. In the spectrum analyzer, the different optical power at each wavelength comprising the LED spectrum are resolved using a diffraction grating and continuously measured using a self-scanning CCD array interfaced with a personal computer.

4.1 Peak Wavelength Tracking

The use of a broadband source in the spectrometer-based demodulation system can be viewed as equivalent to a large number of laser diodes placed successively in the wavelength domain. Since the phase difference ϕ for a given Fabry-Perot gap separation described in Equation (3.1-2) is a function of the wavelength, the outputs due to each laser diode differ in phase, and hence, the output intensity varies as a function of

wavelength. For a broadband source, the phase difference $\Delta\phi$ between two fixed wavelengths λ_1 and λ_2 of the return signal from the interferometer has the following relationship [28, 36, 37]

$$\Delta\phi = \frac{4\pi nd}{\lambda_1} - \frac{4\pi nd}{\lambda_2}. \tag{4.1-1}$$

Rearranging the above equation, the dimension of the Fabry-Perot cavity can be found if the phase difference $\Delta\phi$ between two wavelengths is known, using [28, 36, 37]

$$d = \frac{\lambda_1\lambda_2}{4\pi(\lambda_2 - \lambda_1)}\Delta\phi. \tag{4.1-2}$$

A convenient approach toward evaluating Equation (4.1-2) is to set $\Delta\phi$ to 2π, which corresponds to the constant phase difference occurring exactly between two consecutive wavelength peaks. Decoding of the remote fiber sensor output is most easily accomplished with a spectrometer, and it requires only simple computation.

4.1.1 Hardware Configuration

The basic experimental setup of the spectrometer-based EFPI sensing system is illustrated in Figure 4.1-1. The experimental decoder consists of an 830 nanometer superluminescent light emitting diode (SLED) injecting a broadband optical signal having a full width half-maximum (FHWM) of 25 nanometers into the Fabry-Perot sensing cavity. The SLED, pigtailed onto a singlemode fiber, is rated for 1.4 milliwatt at a drive current of 120 milliamp. The output signal from the EFPI sensor is fed directly into a grating-based spectrometer where a CCD array is used for spectral imaging and analysis. The spectrometer made by Ocean Optics consists of an 1800 lines/mm holographic ruled

diffraction grating which spreads out the incoming light spatially across a linear CCD array. The internal arrangement of the diffraction grating and the imaging array of the spectrometer only passes wavelengths ranging from 780 to 860 nanometers ($\Delta\lambda$ = 80 nm). Since the CCD array has 1024 pixel elements, the wavelength resolution calculated from Equation (3.5-1) for the experimental spectrometer is approximately 0.07 nanometer. Thus, each output frame from the CCD array consists of 1024 pulse amplitude modulated (PAM) signals [31,33]. Based on this minimum detectable wavelength, the displacement that is calculated from Equation (4.1-2) can at the most have a resolution of 0.5 micrometers.

Since each pixel element in the CCD array is excited by a different wavelength, the incident light charges the CCD element to a voltage level proportional to the intensity and the efficiency at that particular wavelength. The individual pixel element behaves like a capacitor requiring a prescribed amount of time for charging and discharging. Therefore, the efficiency of the diffraction grating and the incident optical power dictates the integration time of the CCD array and thereby affects the overall frequency response of the spectrometer. The analog voltage signals from the CCD array are then sequentially sampled using a 12-bit analog-to-digital converter (ADC) board. Here, a ComputerBoard DAS-330 ADC allows the signal to be sampled at a rate of 500 kHz. At this maximum 500 kHz sampling rate, the acquired frame rate for the 1024 pixel element CCD array is 480 frames/second. Note that the frequency response of the demodulation system is specified by the slower frame rate since the signal processing is operated on the entire frame of data not on the individual pixel element. If we choose to process individual pixel element, the output from each pixel of the spectrometer is interleaved between successive scan thus the effective frequency response remains the frame rate. Finally, the digitized signal is processed with software using a personal computer.

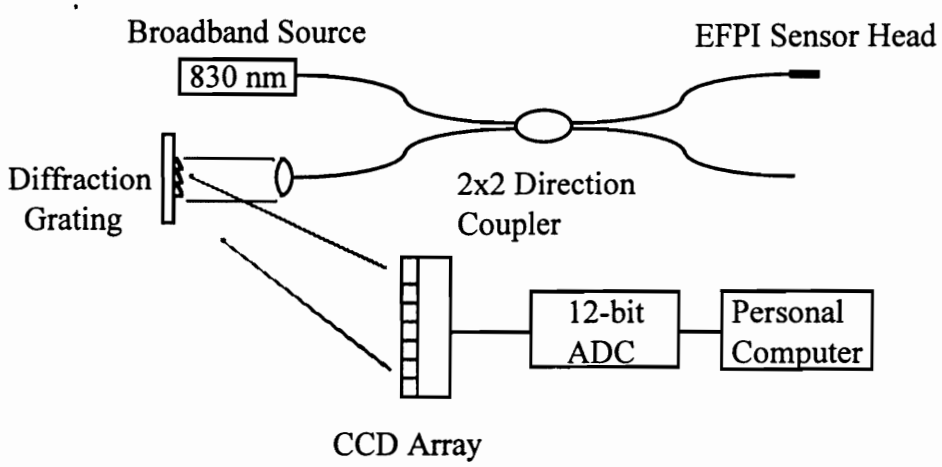

Figure 4.1-1. Experimental setup of the spectrometer-based EFPI sensing system.

The software that implemented the constant phase algorithm was written in Borland C++. The computer program is coded to perform a number of functions, specifically

- synchronize the timing between the ADC and the CCD array,
- calibrate the spectrometer so that each pixel of the CCD array corresponds to a particular wavelength,
- average the acquired data using a preset number of data frames,
- determine the wavelength peaks in the interferogram by calculating the slope of the voltage level between two adjacent pixels,
- obtain the Fabry-Perot cavity displacement from Equation (3.3.4-2), and
- display the calculated displacement as a measurement of the applied perturbation which may include strain, temperature, or pressure.

4.1.2 Experimental Results

Experiments conducted using the above basic wavelength tracking approach were initially unsatisfactory because the demodulation system utilized a sensor design that was impractical to use, and the unsophisticated signal processing algorithm performed poorly. For example, preliminary experiments required high finesse Fabry-Perot sensing cavities that operated only in transmission. The high finesse cavities were necessary to increase the sharpness of the transmittance peaks, thus allowing the software to better discriminate between the two wavelength peaks that are 2π out of phase. By increasing the reflectivities of the fiber endfaces, we effectively improve the fringe visibility and signal-to-noise ratio of the transmitted signal without having to increase the input optical power.

The preliminary experiments also indicated that the EFPI sensors cannot be used in reflection because the spectral peaks are dispersed over a broad range of wavelengths, as illustrated in Figure 4.1-2. The dispersion prevented the demodulation system from accurately locating the spectral peak. Finally, being located near the noise floor of the system, the poorly defined spectral minima did not provide the information needed to calculate the displacement of the Fabry-Perot cavity.

As a first step towards overcoming the impractical sensor design and the poor resolution, digital filters were utilized. As shown in Figure 4.1-3(a), a third-order Butterworth filter, implemented in software, can be used to selectively remove the high frequency noise interference from the interferogram of Figure 4.1-3(b). Besides removing the random noise, digital filters can be used to reshape the interferogram and enhance the spectra for application in the peak tracking algorithm. By making use of digital filters, the initial requirement that the sensor must be operated only in transmission and must use only high finesse cavities, the demodulation system can now work with a broad range of sensor configurations. Moreover, the actual optical fiber sensing probes can now be fabricated from EFPI sensors that operate in reflection. Further resolution improvement may be obtained through modification of the spectrometer. As is obvious, a CCD array having more than 1024 pixels can be used to improve the wavelength resolution, but this will increase the integration time of the array or decrease the frequency response. Similarly, at the expense of improving the resolution by using a grating with more diffraction lines (3600 lines/mm versus 1800 lines/mm), the efficiency of the spectrometer is significantly reduced [33]. As a solution to this problem, one would need to use a source that outputs higher intensity to achieve an equivalent SNR. Alternately, we can improve the performance of the spectrometer-based EFPI system by employing more advanced digital signal processing techniques, as discussed in Section 4.2.

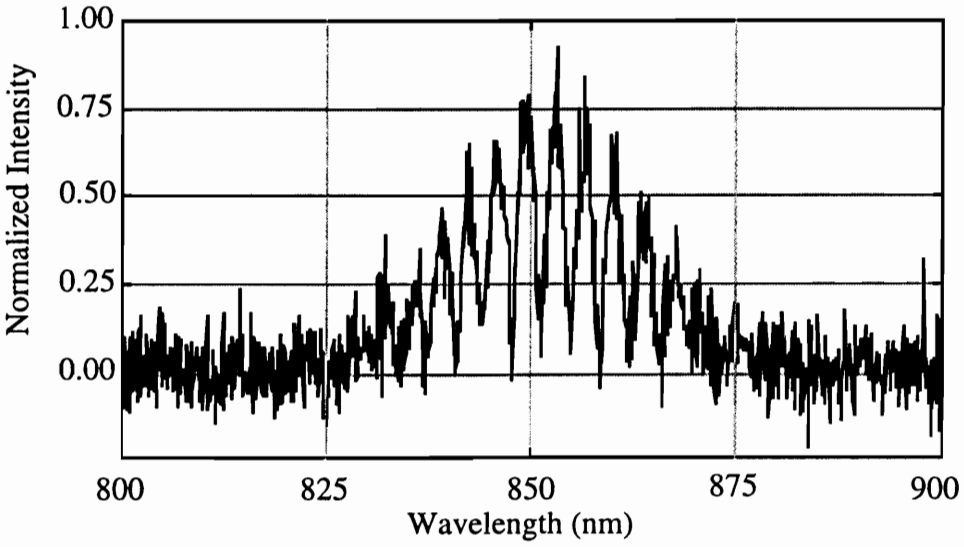

Figure 4.1-2. Reflected spectrum from the EFPI sensor showing the wavelength minima residing within the noise floor. R=70%, gap=50 μm.

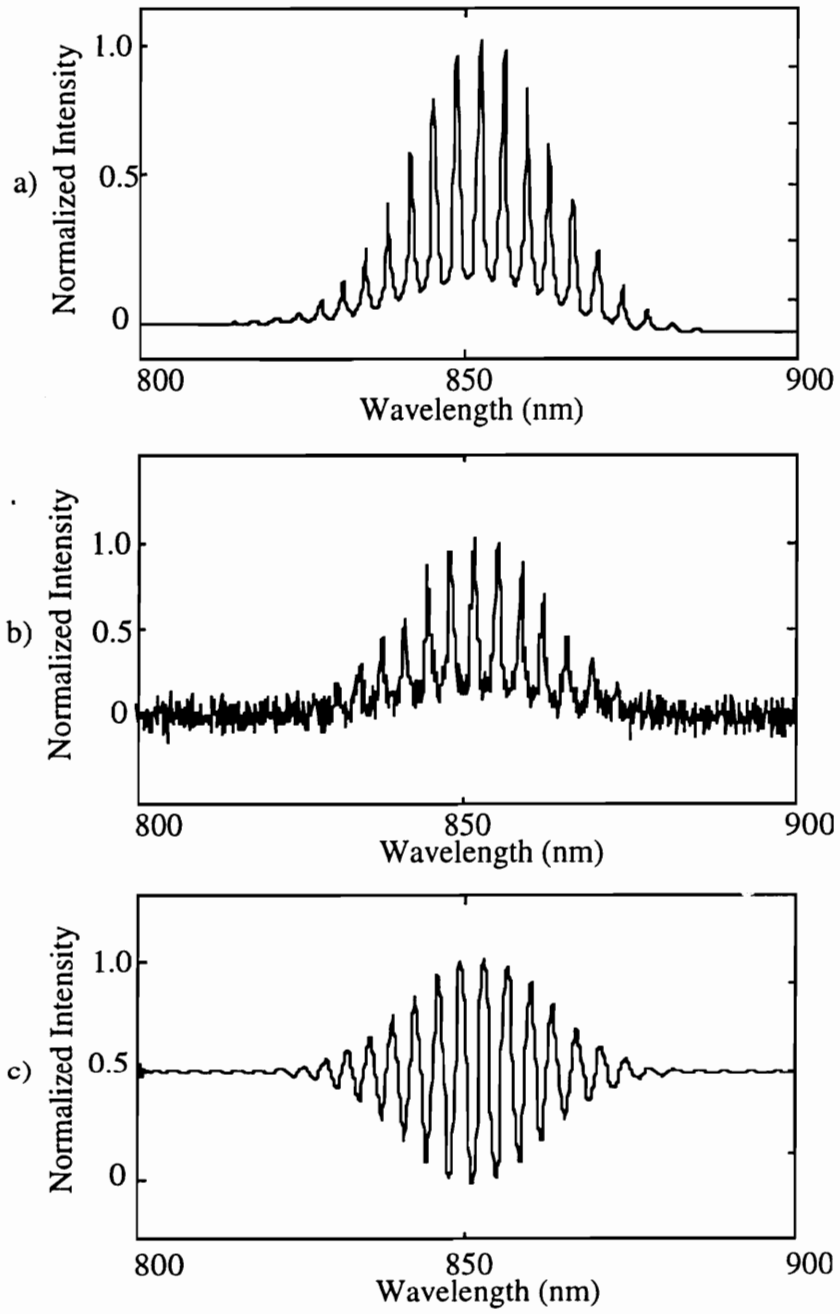

Figure 4.1-3. a) Interferogram corrupted with random thermal noise in CCD array. A low-pass Butterworth digital filter can be used to b) remove high-frequency noise component, or c) reshape the interferogram so that wavelength minima can be used in constant phase algorithm. Specifications of sensor: R=80%, gap=50 μm.

4.2 Fourier Transform Spectroscopy

Spectral estimation and fringe analysis using the Fourier transform offer a significantly higher measurement resolution. The fast Fourier transform (FFT) algorithm has been effectively applied for the past 25 years to general signal processing in data communications, seismology, radar, sonar, speech compression, imaging systems, and many other applications [38, 39, 40]. Processing of the interferogram in the frequency domain is appealing because of the availability of dedicated microprocessors designed for high-speed real-time processing.

The use of the FFT method for fringe analysis was first proposed by Takeda for measuring two-dimensional phase distributions over the interfering plane, and has since found applications in tomography and electron wave interferometry [6,41]. In these applications, the algorithm was restricted to straight, parallel and equi-distant fringes. In contrast, the fringe patterns of the fiber Fabry-Perot interferometer are typically distorted by various types of imperfections such as mirror surface irregularities and defects [42,43], angular misalignment of the mirrors [44-46] and the imaging behavior of the grating spectrometer [47,48]. The broadband source in combination with a nonlinear spectrometer, also produce interferograms comprised of many frequency harmonics. The FFT-based algorithm developed during this research is designed to overcome some of these problems. The FFT calculates as many harmonically related sets of sinusoidal components as there are data points in the data set. It is used primarily to compute the power spectral density (PSD). In the frequency domain, the desired signal can be easily isolated from the noise. Since discrete harmonic components are available from the FFT, the frequency resolution can be further improved by interpolation schemes.

Assuming then that the intensity distribution of the Fabry-Perot fringes forming the interferogram across the face of the CCD array is linear and uniformly spaced apart, and can be written as [41,48,49]

$$I(x) = A(x)\left[1 + \gamma(x)\cos(2\pi fx + \phi)\right], \tag{4.2-1}$$

where A(x) is the average intensity, $\gamma(x)$ is the contrast, f is the spatial frequency, ϕ is the initial phase of the fringes in the interferogram, and the argument x is the spacing across the surface of the CCD array. The Fourier transform of Equation (4.2-1) is expressed by [22,23,26]

$$\hat{I}(v) = \int_{-\infty}^{\infty} I(x)\exp(-2\pi ivx)dx = \hat{A}(v) + \hat{C}(v - f)\exp(i\phi) + \hat{C}(v + f)\exp(-i\phi), \tag{4.2-2}$$

where

$$\hat{A}(v) = \int_{-\infty}^{\infty} A(x)\exp(-2\pi ivx)dx, \tag{4.2-3}$$

$$\hat{C}(v) = \frac{1}{2}\int_{-\infty}^{\infty} A(x)\gamma(x)\exp(-2\pi ivx)dx. \tag{4.2-4}$$

Accounting for distortions caused by the imperfection of the interfering wave, the fringe intensity is described by [22,23,26]

$$I(x) = A(x)\left[1 + \gamma(x)\cos(2\pi fx + \omega(x) + \phi\right], \tag{4.2-5}$$

and

$$\hat{C}(v) = \frac{1}{2}\int_{-\infty}^{\infty} A(x)\gamma(x)\exp(-i\omega(x))\exp(-2\pi ivx)dx. \qquad (4.2\text{-}6)$$

For discretely sampled signals, the above calculation can be done with the use of a discrete Fourier transform (DFT). We considered using the discrete Fourier transform pair [40,41]

$$H(\frac{n}{NT}) = \sum_{p=0}^{N-1} h(pt)\exp(\frac{-2\pi ipn}{N}), \qquad (4.2\text{-}7)$$

and

$$H(p) = \frac{1}{N}\sum_{p=0}^{N-1} h(\frac{n}{NT})\exp(\frac{-2\pi ipn}{N}), \qquad (4.2\text{-}8)$$

where N denotes the number of sampling points, T is the sampling spacing, and n and k are integers. For simplicity we set T=1. The discrete representation of Equation (4.2-1) is

$$I(p) = A(p)[1+\gamma(p)\cos(2\pi fp+\phi)], \quad (p = 0,1,...,N-1). \qquad (4.2\text{-}9)$$

The discrete Fourier transform of Equation (4.2-9) is

$$\hat{I}(\frac{n}{N}) = \hat{A}(\frac{n}{N}) + \hat{C}(\frac{n}{N}-f)\exp(i\phi) + \hat{C}(\frac{n}{N}+f)\exp(-i\phi), \quad (n = 0,1,...,N-1), \qquad (4.2\text{-}10)$$

where

$$\hat{A}(\frac{n}{N}) = \sum_{p=0}^{N-1} A(p)\exp(-\frac{2\pi ipn}{N}), \tag{4.2-11}$$

and

$$\hat{C}(\frac{n}{N}) = \frac{1}{2}\sum_{p=0}^{N-1} A(p)\gamma(p)\exp(-\frac{2\pi ipn}{N}). \tag{4.2-12}$$

4.2.1 Issues of Windows for Fourier Transform

The Fourier transform series shown above treats a block of data as though it were one period of a periodic sequence. If the underlying waveform is not periodic, then harmonic distortion may occur because the periodic waveform created by the Fourier transform may have sharp discontinuities at the boundaries of the blocks. This effect is minimized by removing the mean of the data and by windowing the data so the ends of the block are smoothly tapered to zero. A good rule of thumb is to taper 10% of the data on each end of the block using either a cosine taper or one of the following common windows [39,40],

- Rectangular

$$w(n) = \begin{cases} 0.54 - 0.46\cos(2\pi n/N), & 0 \le n \le N-1 \\ 0, & \text{otherwise} \end{cases} \tag{4.2.1-1}$$

- Hamming

$$w(n) = \begin{cases} 0.54 - 0.46\cos(2\pi n/N), & 0 \le n \le N-1 \\ 0, & \text{otherwise} \end{cases} \tag{4.2.1-2}$$

- Hanning

$$w(n) = \begin{cases} 0.5 - 0.5\cos(2\pi n / N), & 0 \le n \le N-1 \\ 0, & \text{otherwise} \end{cases} \qquad (4.2.1\text{-}3)$$

- Blackman

$$w(n) = \begin{cases} 0.42 - 0.5\cos(2\pi n / N) + 0.08\cos(4\pi n / N), & 0 \le n \le N-1 \\ 0, & \text{otherwise} \end{cases} \qquad (4.2.1\text{-}4)$$

An alternate interpretation of this phenomenon is that finite-length observation has already windowed the true waveform with a rectangular window that has large spectral sidelobes. Hence, applying an additional window results in a more desirable window that minimizes frequency domain distortion.

4.2.2 Resolution of Fourier Transform Spectroscopy

The calculation of the Fourier transform is not usually accomplished with the discrete Fourier transform (DFT) shown above. The Fourier transform is evaluated using the FFT algorithm, since this numerical technique is several orders of magnitude faster than the DFT algorithm. The resolution that is obtainable by means of the Fourier analysis is inversely proportional to the total sample period; N/2 independent spectral lines spanning the frequency from 0 to 0.5 of the sampling frequency are obtained for N input data points.

To improve the estimation resolution, the input signal can be zero-padded to increase the record length [39]. Zero-padding provides the additional spectral lines in the FFT which

will approach the continuous Fourier transform based on the original sample record length. Zero-padding can also resolve ambiguities and reduce the quantization error in the spectral lines of the FFT. It must be understood that the finite observation interval results in a fundamental limit on the spectral resolution, even before the signals are sampled. The continuous time rectangular window has a $\sin(x)/x$ spectrum, which is convolved with the true spectrum of the analog signal. Therefore, the frequency resolution is limited by the width of the mainlobe in the $\sin(x)/x$ spectrum, which is inversely proportional to the length of the observation interval.

Sampling causes a certain degree of aliasing, although this effect can be minimized by sampling at a high rate. Therefore, lengthening the observation interval increases the fundamental resolution limit, while taking more samples within the observation minimizes aliasing distortion and provides a better definition of the underlying spectrum [22,40].

4.2.3 Spectral Estimation Errors

To further enhance the resolution already improved with zero-padding, information in adjacent spectral lines can be utilized in an interpolation technique. In general, a mathematical function is interpolated between the spectral peak of the FFT and the two adjacent spectral lines. The frequency estimate derived from this interpolation can be several orders of magnitude more accurate than a straight FFT calculation. Typical functions employed for curve fitting are parabolas, Gaussians, Sinc, or centroids of the energy of the spectral lines. The parabolic fit applied to the FFT of an interferogram uses the following equation [50]

$$\hat{I}_{est}(v) = \hat{I}(v) + \left[\frac{P_{i-1} - P_{i+1}}{2(P_{i-1} + P_{i+1} - 2P_i)}\right]\Delta I \ , \qquad (4.2.3\text{-}1)$$

where $\hat{I}_{est}(v)$ is the interferogram frequency estimate, $\hat{I}(v)$ is the frequency of the peak spectral line derived from the FFT, P_{i-1} and P_{i+1} are the magnitudes of the adjacent spectral lines, and $\Delta I = 1/N\ \Delta t$ is the spectral line spacing of the FFT. The Gaussian curve fit is applied in the same manner and is given by [51]

$$\hat{I}_{est}(v) = \hat{I}(v) + \left[\frac{\ln\left(\frac{P_{i-1}}{P_i}\right) - \ln\left(\frac{P_{i+1}}{P_i}\right)}{2\left[\ln\left(\frac{P_{i-1}}{P_i}\right) + \ln\left(\frac{P_{i+1}}{P_i}\right)\right]}\right]\Delta I. \qquad (4.2.3\text{-}2)$$

The centroid method is another method for interpolating the FFT. The centroid interpolation is given by [52]

$$\hat{I}_{est}(v) = \hat{I}(v) + \left[\frac{f_{i-1}P_{i-1} + f_iP_i + f_{i+1}P_{i+1}}{P_{i-1} + P_i + P_{i+1}}\right]\Delta I. \qquad (4.2.3\text{-}3)$$

4.2.4 Experimental Results of Fourier Transform Spectroscopy

Using the FFT algorithm, the gap of an EFPI sensor was determined by identifying the frequency of the sinusoidal period in the wavelength domain. Here, we have assumed that the spacing over a small spectral distance for EFPI fringes is approximately uniform. This periodicity corresponds uniquely to a specific gap based on the constructive and destructive superpositioning of individual wavelengths. Applying an FFT results in a spectral peak corresponding to a specific value in the frequency domain. This peak falls within a single FFT bin which correlates to a gap [29]. Calibration curves can be

determined for the displacement by determining the frequency bin of the spectral output sinusoid for a range of gaps. These values can be integrated into a look-up table for fast processing of the signal. In addition to interpolation methods for increasing the resolution, phase detection can also be employed. Figures 4.2-1 through 4.2-3 show the theoretical results expected when the FFT algorithm is used. The plots show both the error and the resolution expected for the FFT technique, both with and without phase corrections. The data also considers the size of the FFT necessary to achieve a desired resolution.

With ordinary spectral analysis, the resolution is directly related to the record length as we have explained earlier and illustrated in Figure 4.2-1. It would seem logical that we would want to calculate the FFT with as large of a record length as possible by increasing the zero-pad. With a long record length of 524288, we can theoretically achieve an estimate resolution of 1 nm. However, the computation time and hardware memory requirements would not be practical. For example, it takes 4.2 seconds to compute a complex FFT of 2^{17} (131072) elements using a 133 MHz Pentium® processor. The computation alone would also require 2 MB of memory to store and execute the transform. Clearly from a practical standpoint of speed, increasing the record length of the data via zero-padding to improve the resolution of the spectral estimation is not a viable option assuming that we can easily expand the memory capacity. Since the bias errors associated with the FFT algorithm do not significantly decrease with an increase in the record length as illustrated in Figures 4.2-1 and 4.2-2, the optimum record length for simultaneously minimizing the resolution and error is an FFT that is evaluated with 4096 elements. Even with a limited record length, the actual frequency response of the demodulation system employing digital filters, Fourier analysis and interpolation is still degraded to less than 10 Hz from a frame sampling rate of 480 Hz.

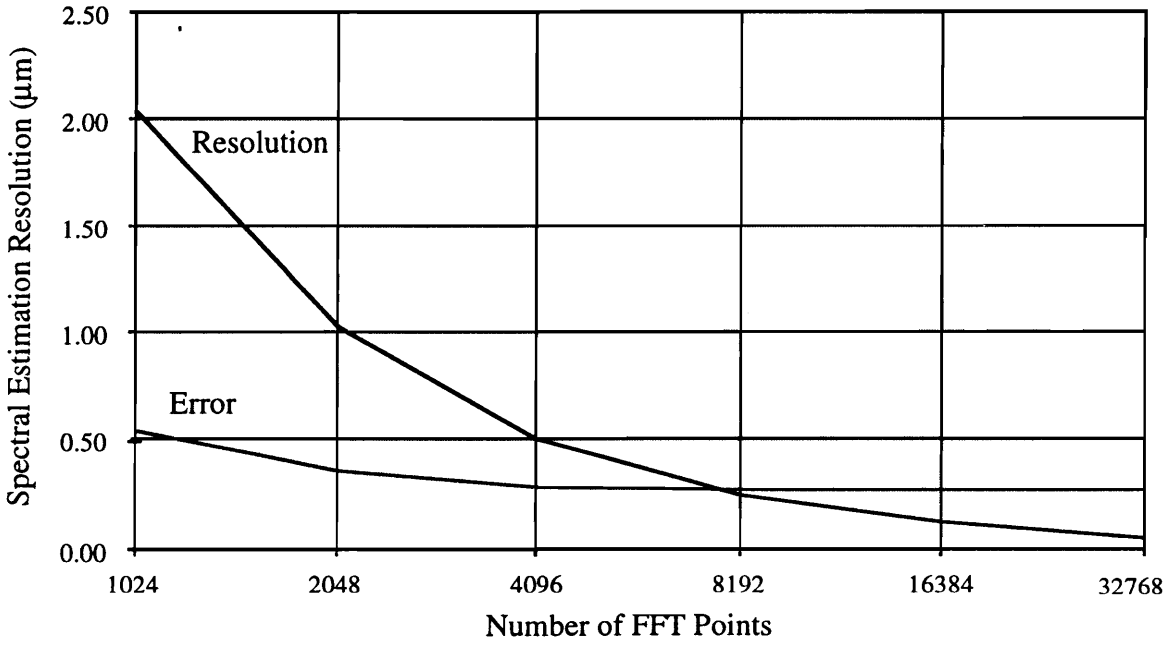

Figure 4.2-1. Resolution and error obtained with no phase correction.

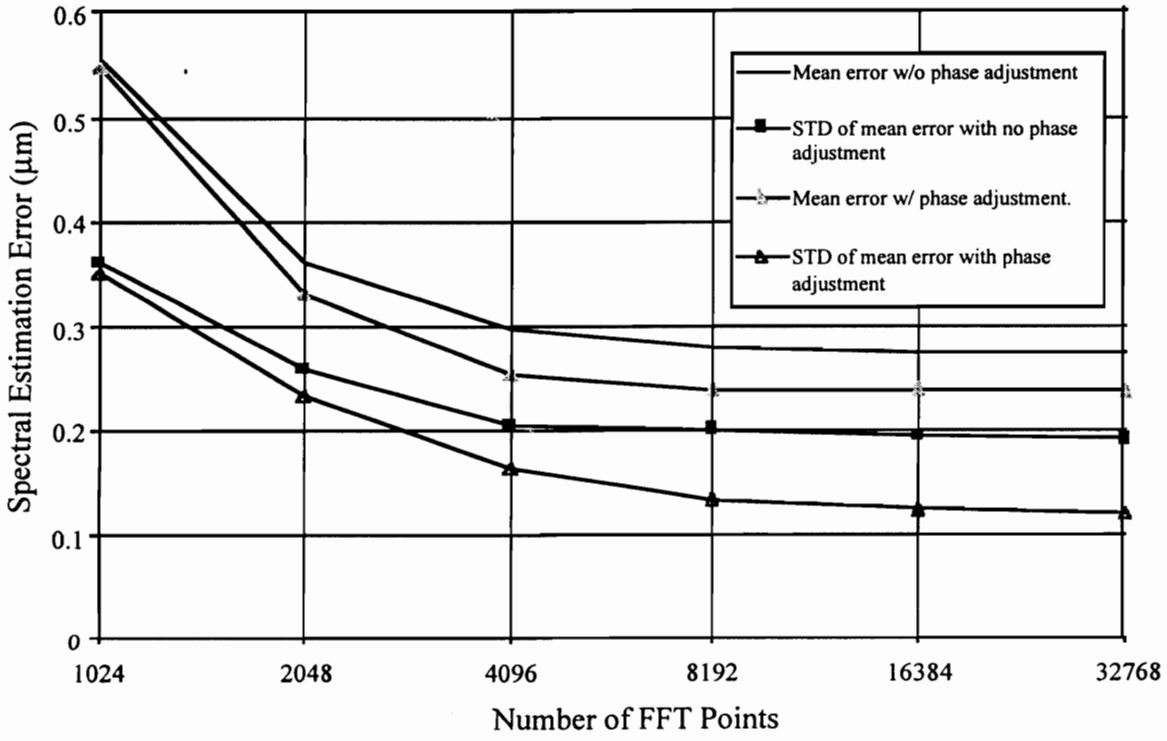

Figure 4.2-2. Mean and STD of error for FFT-based processing with and without phase adjustment.

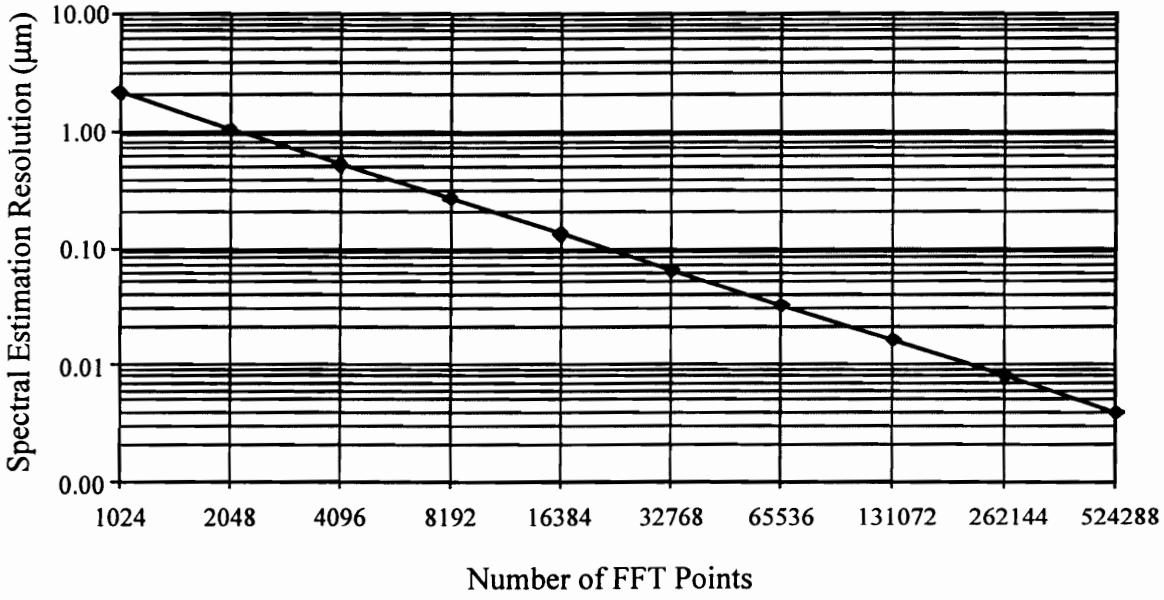

Figure 4.2-3. Theoretical spectral resolution without phase correction improves with an increase in the record length.

4.3 Irregular Sampling Problem

In developing the algorithm for analyzing the interferometric signal, we have assumed that the Fizeau fringes or interferogram, produced by the interference of plane waves are uniformly spaced apart (equispaced) and that the sampling interval are uniformly spaced at p = nh points, where h = $\lambda_{max}/2$, and n is an integer. When the digitized signal I(λ) is evaluated using the FFT algorithm, we expect to obtain an undistorted spectral peak, I(v), in the frequency domain. In practice, however, the intensity distributions that are captured by the CCD array do not produce equispaced interferograms. The main reason is that the incident wavefront is not normal to the surface of the imaging detector. Even though the incoming optical signal is sampled at a uniform rate, the angle at which the optical signal impinges on the detector face causes the actual recorded signal to chirp in frequency as illustrated in Figure 4.3-1. In fact, the instantaneous frequency of the chirped signal depends on where the light falls on the CCD array, the center wavelength, and the spectral width of the optical source.

For a given air-gap, the resulting spectral estimation errors are directly related to these distortion effects. Ordinary Fourier analysis hides the fact that a chirp signal has a well-defined instantaneous frequency by integrating over the entire time interval, thus arriving at a very broad frequency spectrum. The spectral peak from the periodogram is an average value indicating the dominant frequency of the interferogram. The use of such multiresolution approach as the short time (windowed) Fourier transform is similarly not effective for this application. We therefore need to extend the classical spectral estimation technique to specifically mitigate the distortion effects associated with our use of a CCD-based spectrum analyzer.

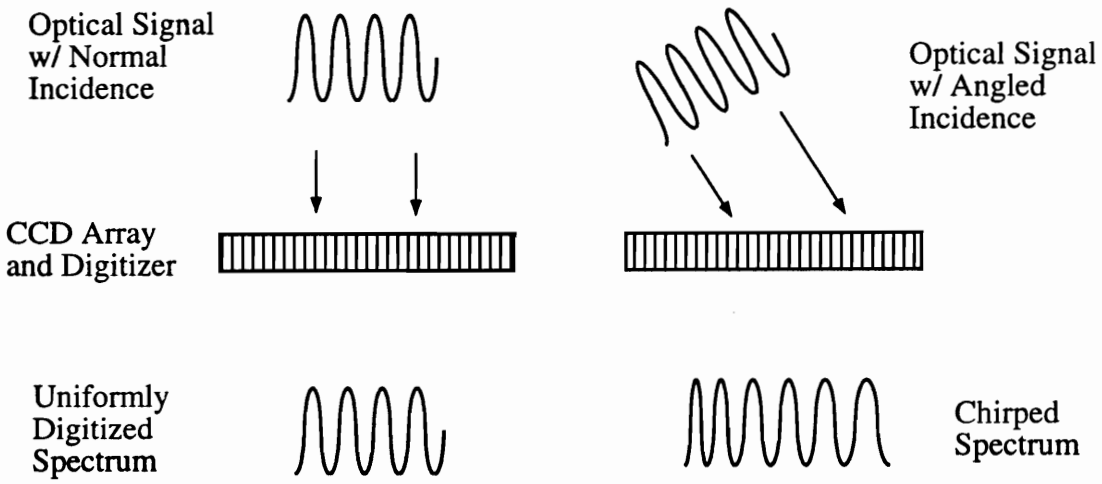

Figure 4.3-1. Signal distortion produced by a diffraction-based spectrometer.

We can regard the harmonic distortion discussed above as a problem of irregular sampling. Since a signal I(x) cannot be recorded in its entirety, it is sampled at sequence $\{ \lambda_n, n \in Z\}$. Then the question arises how $I(\lambda)$ can be reconstructed or at least approximated from the samples I(x). In practice, only a finite number of samples can be measured and stored. In the case of irregular sampling, the problem becomes a finite dimensional problem and can be approached with methods of linear algebra. Since the sampling points are nonuniform, the spatial frequency can be expressed by

$$f = (n_c + \Delta n)/N , \tag{4.3-1}$$

where n_c and Δn are the constant and the fluctuation components of the fringes respectively. When Δn in Equation (4.3-1) is not zero, we then have [48]

$$\hat{I}(\frac{n}{N}) = \hat{A}(\frac{n}{N}) + \hat{C}(\frac{n}{N} - f(n+\Delta n))\exp(i\phi) + \hat{C}(\frac{n}{N} + f(n+\Delta n))\exp(-i\phi), \quad (n = 0,1,...,N-1) \tag{4.3-2}$$

where

$$\hat{C}(\frac{\Delta n}{N}) = \sum_{p=0}^{N-1} A(p)\gamma(p)\exp(-2\pi i p\frac{\Delta n}{N}). \tag{4.3-3}$$

To find the interpolated value at the point $n_c+\Delta n$, we can use the shifting property of the discrete Fourier transform to obtain [48],

$$\hat{I}\left(\frac{n}{N}+\frac{\Delta n}{N}\right)=\sum_{p=0}^{N-1}I(p)\exp\left[-2\pi ip\left(\frac{n}{N}+\frac{\Delta n}{N}\right)\right]$$

$$=\sum_{p=0}^{N-1}I(p)\exp\left[-2\pi ip\frac{\Delta n}{N}\right]\exp\left[-2\pi ip\frac{n}{N}\right]. \qquad (4.3\text{-}4)$$

From the spectral estimation, we can calibrate the demodulation system to determine the displacement of the resonant cavity using a polynomial interpolation curve fit. The coefficients of the polynomial, relating the spatial frequency of the CCD array to the displacement of the resonant cavity, are determined by the diffraction characteristics of the spectrometer. We can also use Equations (4.2.3-1) through (4.2.3-3) to interpolate the spectral peak or parts thereof to further improve the measurement resolution.

Although the frequency estimation approach demonstrated above achieves a high displacement resolution, the algorithm still does not account for bias errors. As Figure 4.3-2 clearly shows, bias errors result if the source spectrum shifts in wavelength or changes its spectral width [35]. Figure 4.3-2(a) illustrates how a ±0.5% shift in the wavelength of the optical source can result in a ±2% bias estimation error. While not as severe, the spectral width of the optical source also contribute to the bias error.

The main cause of the bias errors illustrated in Figure 4.3-2 is attributed to the spectrometer. A spectrometer is normally calibrated so that each pixel element of the CCD array is associated with a particular wavelength. If the recorded waveform is plotted as a function of wavelength instead of pixel, Figure 4.3-3 shows that the fringe pattern is associated with a single sinusoidal frequency as opposed to a chirped frequency. Ordinary Fourier analysis cannot account for these nonlinear wavelength effects because the computation assumes a linear and uniform sampling interval.

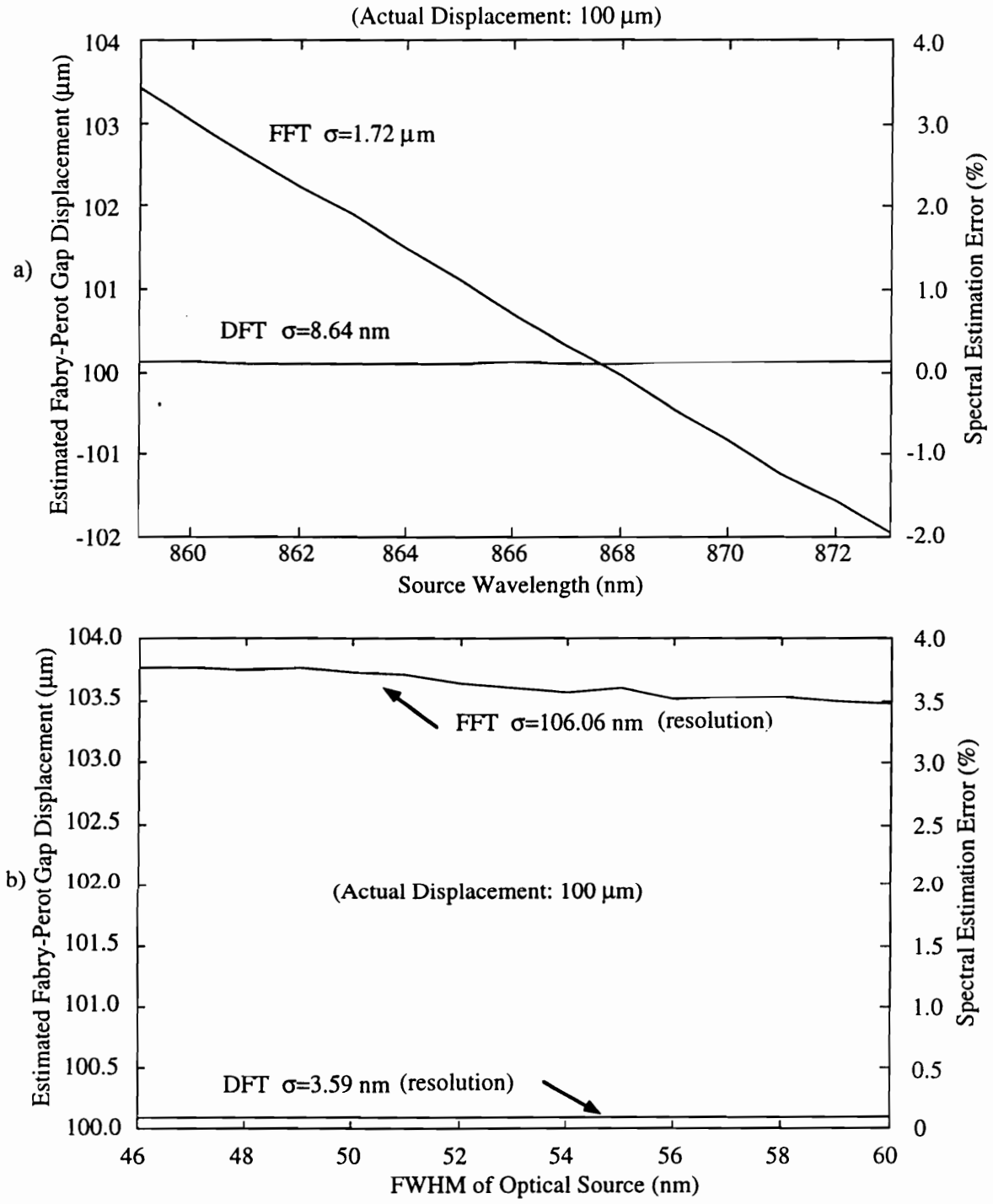

Figure 4.3-2. Graphs showing errors caused by a) shifts of the center wavelength, and b) changes in the spectral width of an optical source for two spectral estimation algorithms.

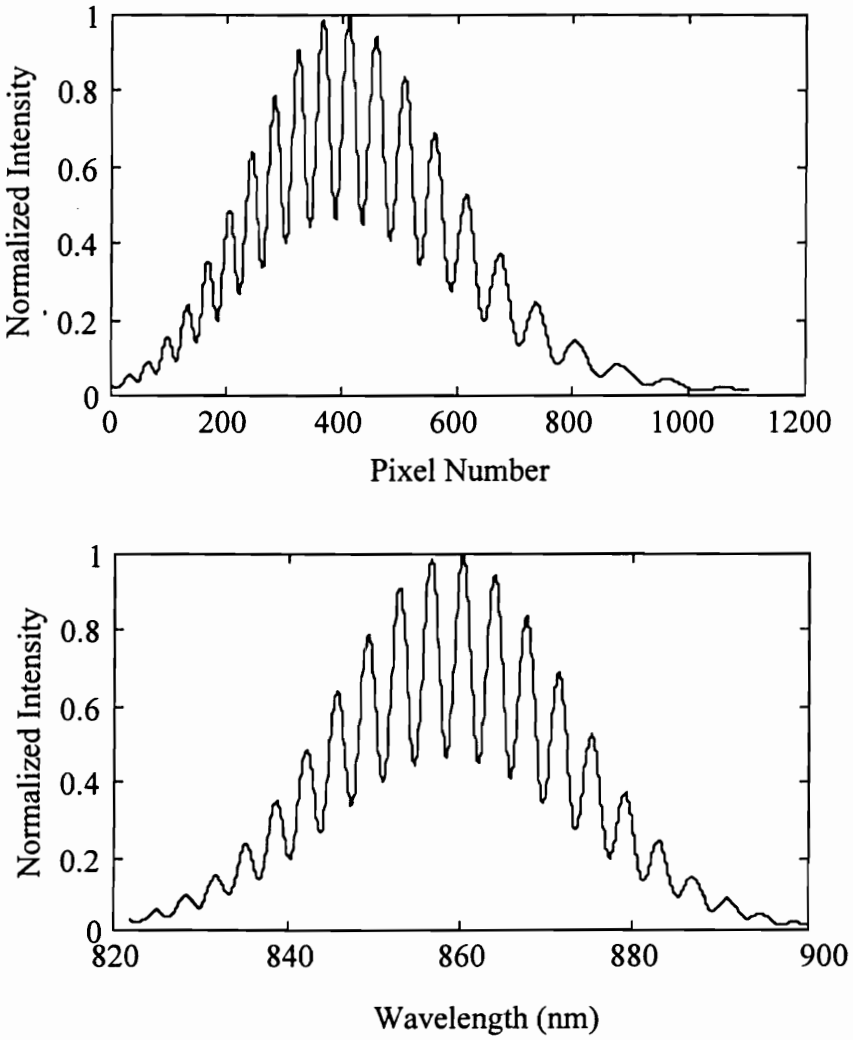

Figure 4.3-3. Graphs showing that a chirped waveform plotted as a function of the pixel element of the CCD array is uniform when it is plotted as a function wavelength.

Let us now define a chromatic Fourier transform integral which is also an orthonormal basis function

$$\hat{I}(d) = \int_{-\infty}^{\infty} I(\lambda)\exp(-\frac{4\pi id}{\lambda})d\lambda\ , \tag{4.3-6}$$

where the usual fundamental frequency ω (in cycles per unit time) is replaced with *d*, representing the displacement of the resonant cavity. Since the integration in Equation (4.3-6) is calculated with respect to wavelength, we are thus able to account for wavelength changes occurring in the fringe pattern. The spectral peak that is obtained by evaluation of Equation (4.3-6) is the actual dimension of the resonant cavity as opposed to a frequency spectral peak that is typically associated with the calculation of the ordinary Fourier transform. In a discrete representation, the chromatic power spectrum is expressed as

$$\hat{I}(d) = \sum_{\lambda_{min}}^{\lambda_{max}} I(\lambda)\exp(-\frac{4\pi id}{\lambda})\Delta\lambda. \tag{4.3-7}$$

The evaluation of Equation (4.3-7) requires a priori knowledge of the displacement. Since the correct displacement is not known, either an iterative method or the band-limited discrete Fourier transform (DFT) interpolation method is necessary. In the iterative method, one first calculate the FFT given by Equation (4.3-4) or use the wavelength peak tracking scheme of Equation (4.1-2) to determine a rough estimate of the displacement. From this estimate, the DFT is iteratively calculated using Equation (4.3-7) to obtain the maximum power spectra. By mathematically maximizing Equation (4.3-7), we can obtain a very precise estimate of the displacement of the resonant air-gap.

4.4 DFT Spectral Estimation Algorithm

Due to the fact that the behavior of the interferometer and the associated phase noise contribution from the optical source were known, several programs were written in both Matlab and C environments to numerically simulate the spectrum produced by a Fabry-Perot interferometer and support system and to evaluate the performance of the DFT implementation of the chromatic power spectral estimation algorithm. A summary of the chromatic spectral estimation algorithm is illustrated in the flowchart of Figure 4.4-1.

Figure 4.4-2(a) plots the interferogram produced by simulation and actual recorded data. The simulated waveform was generated by applying Equation (4.3-5). The Fourier transform of the simulated and experimentally derived signals in Figure 4.4-2(b) show that the spectral peaks are well matched except for the noise floor being greater in magnitude for the actual interferogram. These results are important because they indicate that the experimental interferogram can be represented by simulations with a high degree of accuracy. The simulation will now facilitate our study of other distortion effects in the optical waveguide.

The resolution of the chromatic DFT algorithm as a function of the gap displacement is illustrated in Figure 4.4-3. In the operating range of interest between 50 micrometers and 150 micrometers, the displacement resolution of the demodulation is better than 20 nanometers or 5 microstrain for a 4 millimeter gage length strain sensor. In comparison to the FFT algorithm, a record length of 34,768 elements is needed to achieve a resolution of 20 nanometers. To obtain the same resolution using interpolation, the required record length is shortened to 4,096 elements but the algorithm remains sensitive to random fluctuation. Using the chromatic DFT algorithm, the demodulation system achieves the

desired spectral resolution and is also highly robust against random noise. The main drawback of using the DFT approach is its slow speed caused by an inefficient computational algorithm.

Because the chromatic power spectrum is calculated from wavelength values produced in the calibration of the spectrometer, the dominant cause of errors is attributed to the inaccuracy of the calibration. Figure 4.4-4 plots the bias errors as a function of the pixel calibration error. As pixel jitters increase uniformly in magnitude, the displacement estimation error also increases. However, if the calibration error associated with each pixel is random, the bias estimation oscillates and monotonically increases in amplitude, as illustrated in Figure 4.4-5.

Finally, in Figure 4.4-6 we plot the theoretical spectral resolution as a function of the SNR of the demodulation system. As expected, the resolution plotted in terms of the random error degrades when the SNR decreases. Using an Ocean Optics spectrometer (Model SIE-77), a 1 milliwatt LED (830 nm) source and uncoated Fabry-Perot cavity sensors, a 20 dB SNR was measured for the demodulation system. Note that the SIE-77 spectrometer uses a 1800 lines/inch ruled grating centered at 850 nanometer and having a passband of 100 nanometers. Experimentally, a 20 dB SNR provided an estimation resolution of 10 nanometers. In comparison to theoretical simulations, the resolution for a 20 dB SNR is on the order of 5 nanometers.

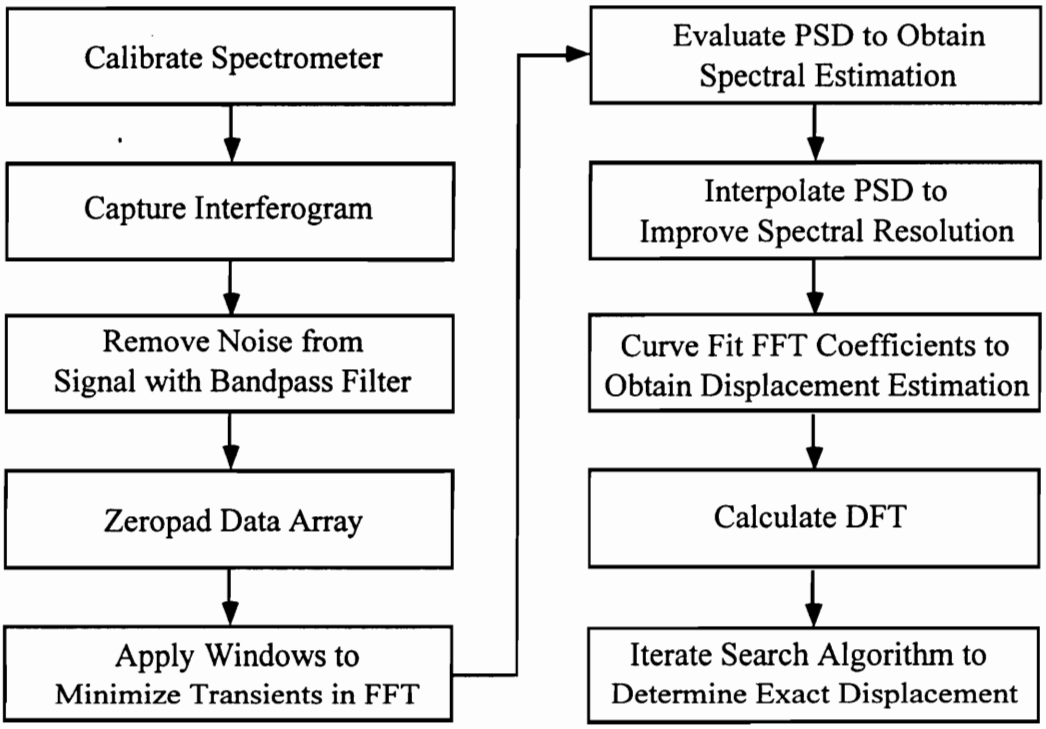

Figure 4.4-1. Flowchart summary of the DFT spectral estimation algorithm.

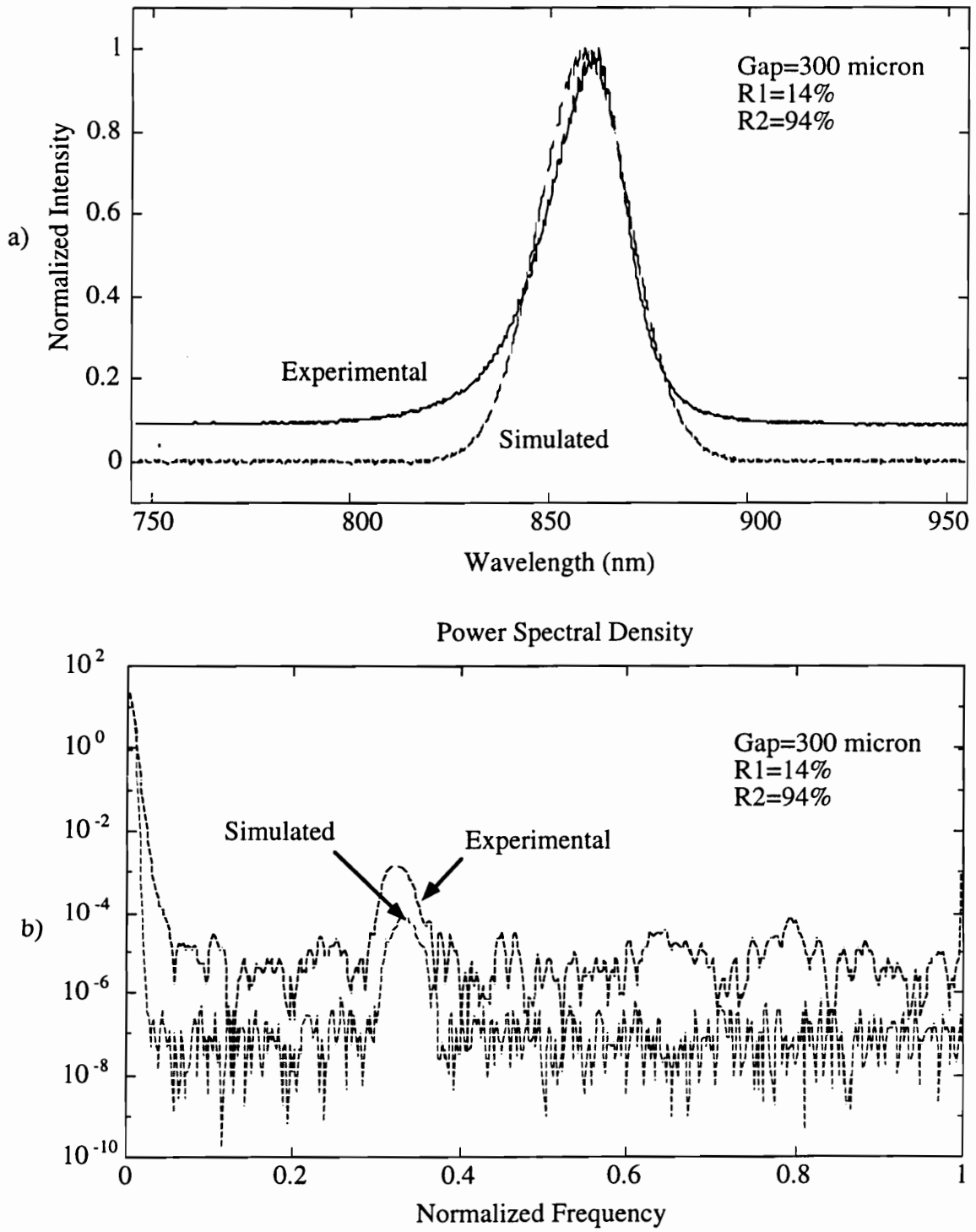

Figure 4.4-2. Plots of (a) interferograms produced by simulation and actual recorded data, and b) power spectral density of the digitized signals.

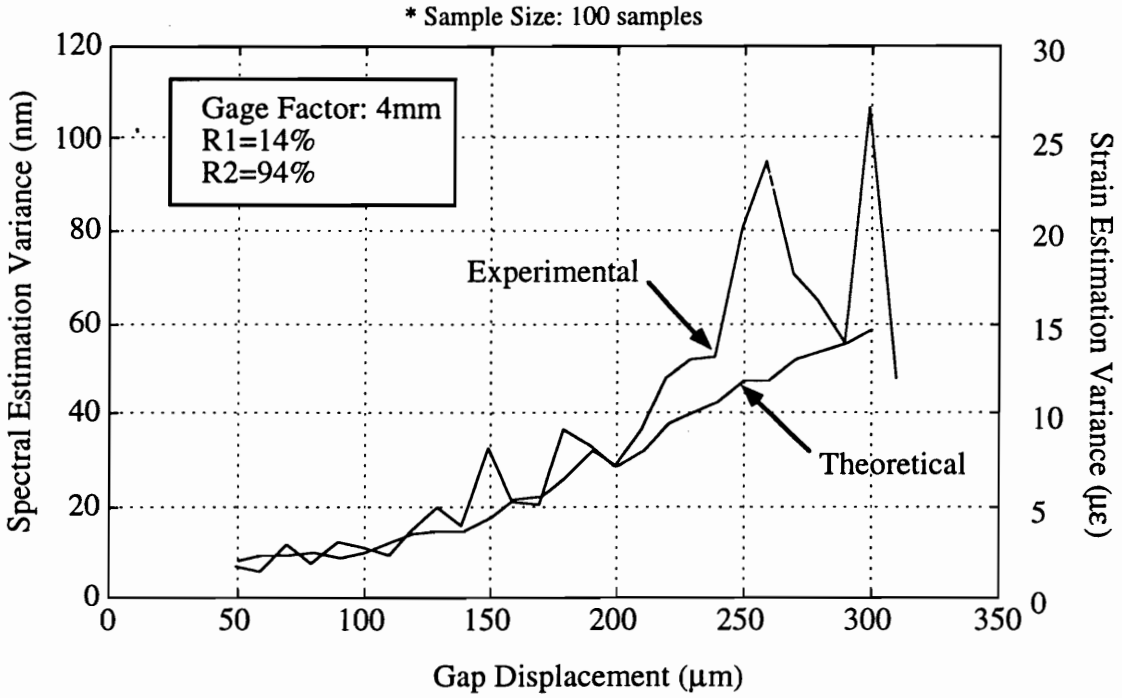

Figure 4.4-3. Degradation of measurement resolution due to large gap displacement.

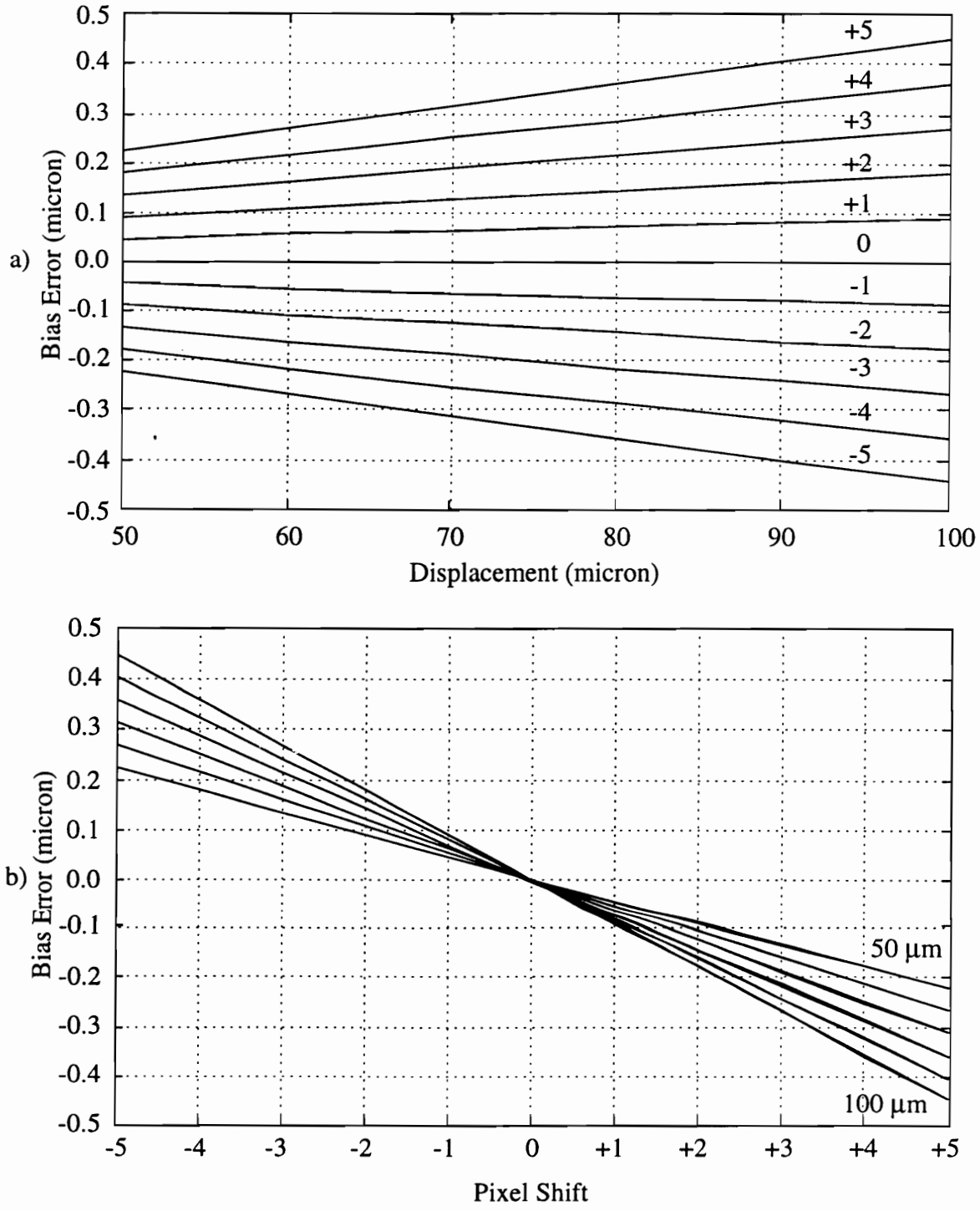

Figure 4.4-4. Bias errors for a spectrometer with fixed uniform pixel-to-wavelength association error.

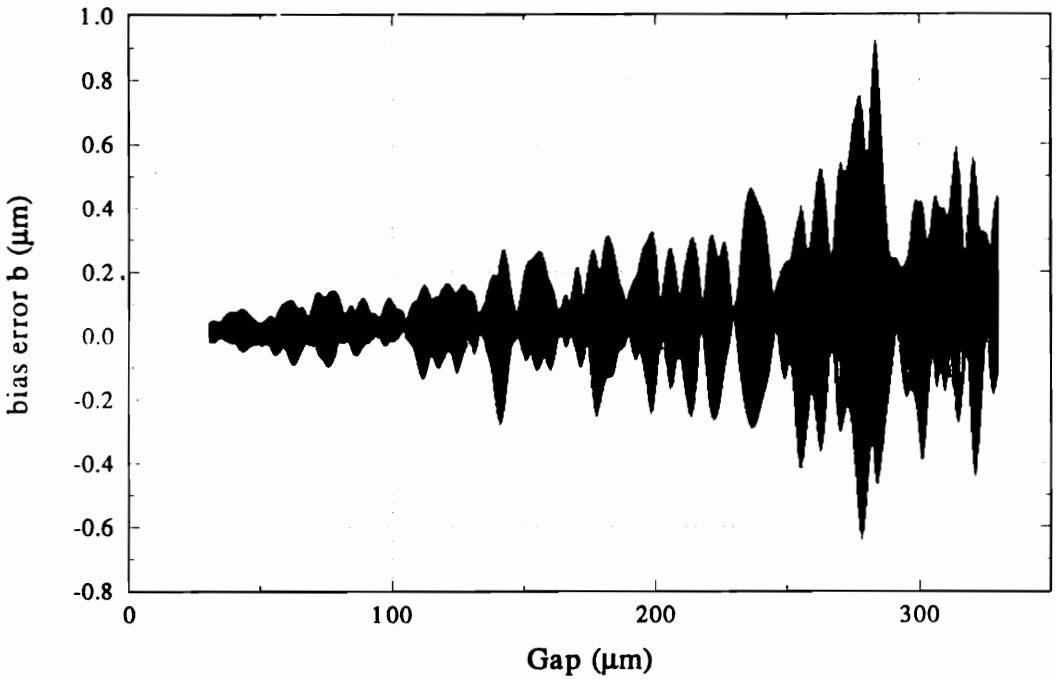

Figure 4.4-5. Bias errors for a spectrometer with random pixel-to-wavelength association error.

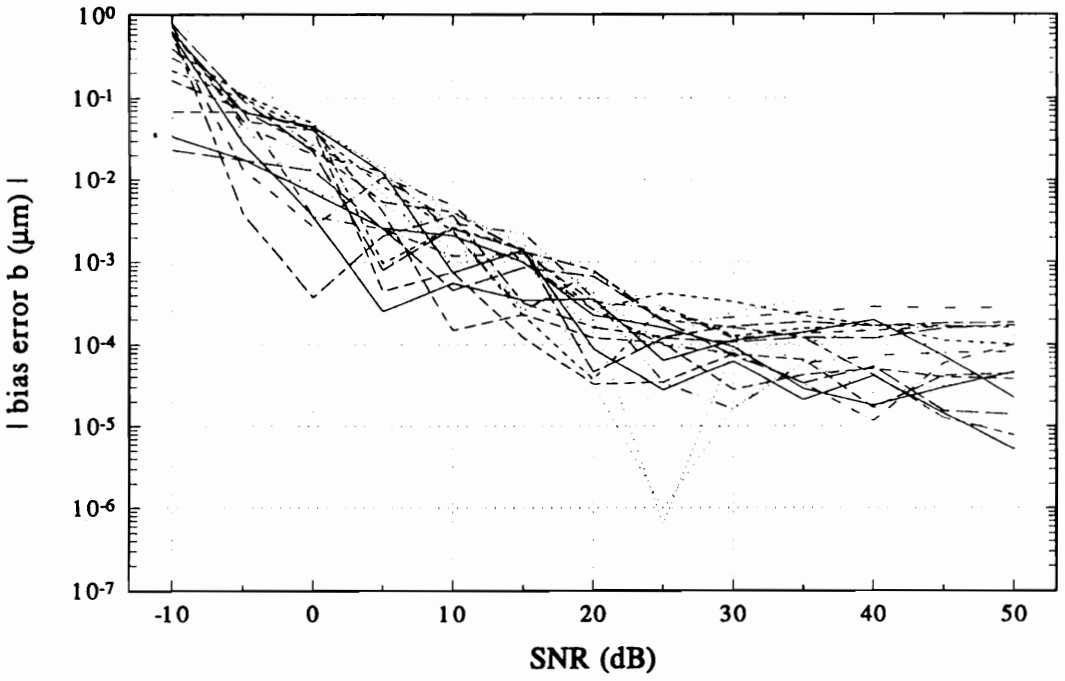

Figure 4.4-6. Spectral resolution degrades as the signal-to-noise ratio decreases.

5. Overview of Optical Waveguide Theory

In the previous chapters, the discussion of the interferometer and the associated signal processing algorithms has assumed that the optical waveguide does not affect the performance of the spectral estimation. Simulation of an ideal optical fiber interferometer using the FFT processing scheme provides a displacement resolution on the order of 0.1 nanometer. In practice, however, noise arising from thermal effects, jitters in the detection electronics, bending losses, chromatic distortion, and other pulse distortion mechanisms have limited the practical displacement resolution to more than 10 nanometers. In order to attain a more detailed understanding of how these effects degrade the performance of the spectral estimation, we need to review the fundamental optical fiber waveguide theory. The optical waveguide theory will allow us to study the mode structure of the optical signal and determine how changes to the guided mode structure will affect the spectral estimation. Since mode theory for circular waveguides has been carried out in extensive detail in a number of works [53-59], a general outline of the analysis will be provided in this chapter.

5.1 Monochromatic Plane-Wave Solutions

To analyze the optical waveguide, we typically consider Maxwell's equations that give the relationship between the electric and magnetic fields. To expedite the analysis, we assume that the medium is a linear and isotropic dielectric material having no currents and free charges. For monochromatic waves in an ideal optical fiber made of a nondispersive and nonabsorptive material, we consider the Helmholtz equation

$$(\nabla^2 + k_o^2 n_i^2\, \partial_t^2) G_i = 0, \tag{5.1-1}$$

where the subscript i=1 is the core, i=2 is the cladding, ∇^2 is the 3-dimensional Laplacian, n is the refractive index ($n_1 > n_2$; n_1, n_2 assumed to be constant), and $k_o = \omega/c$. The refractive index n is related to the dielectric constant $\varepsilon(r)$ by $n^2(r)=\varepsilon(r)/\varepsilon_0$ [1,2,17]. In analyzing the optical waveguide, we consider solutions to the Helmholtz equation represented by

$$G(r,\phi,z,t) = \psi(r,\phi)\exp\left[j(\omega t \pm \beta z)\right], \tag{5.1-2}$$

where β is the propagation constant and, ω is the angular frequency. Limiting ourselves to waves with phase fronts normal to the waveguide axis z, $\psi(r,\phi)$ assumes the form

$$\psi(r,\phi) = \begin{Bmatrix} AJ_v(q_1 r) \\ DK_v(q_2 r) \end{Bmatrix} \begin{pmatrix} \cos(v\phi) \\ \sin(v\phi) \end{pmatrix} \qquad \begin{Bmatrix} r < a \\ r > a \end{Bmatrix}, \tag{5.1-3}$$

where A and D are amplitude constants,

$$q_1^2 = k_o^2 n_1^2 - \beta^2, \text{ and} \tag{5.1-4a}$$

$$q_2^2 = \beta^2 - k_o^2 n_2^2, \tag{5.1-4b}$$

and J_v, K_v are ordinary and modified Bessel functions of order v. In Chapter 6, we will use the modal field expressions obtained here to model the propagation of a phase modulated signal in an optical fiber, and analyze how changes occurring in the waveguide medium, which alter the mode field distribution, will interfere with the performance of the spectral estimation algorithm.

5.2 Weakly Guiding Optical Fibers

In solving the wave equation, there are few known refractive index profiles for which Maxwell's equations lead to exact solutions for the modal fields. Even for the practical and relatively simple step-index profile, the derivation of the vector modal fields in a fiber has been shown to be cumbersome. A considerable simplication in the analysis results if the weak guidance approximation described by Gloge is used. The weak guidance approximation is given by $\Delta << 1$ where [54]

$$\Delta = \frac{n_1^2 - n_2^2}{2n_1^2} \cong \frac{n_1 - n_2}{n_1} << 1 . \tag{5.2-1}$$

If we define parameters U and W for the core and cladding, respectively, viz.,

$$U = a\sqrt{k_o^2 n_1^2 - \beta^2} \text{ , and} \tag{5.2-2a}$$

$$W = a\sqrt{\beta^2 - k_o^2 n_2^2} , \tag{5.2-2b}$$

the quadratic summation $V^2 = U^2 + W^2$ leads to the normalized frequency

$$V = ak_o\sqrt{n_1^2 - n_2^2} = \frac{2\pi a}{\lambda}\sqrt{n_1^2 - n_2^2} , \tag{5.2-3}$$

where *a* is the radius of the fiber and λ is the wavelength of the source. In performing the error analysis of Chapter 6, the radial frequency U is needed to approximate the propagation constant of the core, and W is needed to derive the mode field diameter of the fiber for a particular normalized frequency V.

5.3 Linearly Polarized Modes

Using the weakly guiding condition, the exact solutions of Maxwell's equations can be simplified to give an insight into the properties of certain combinations of modes, termed linearly polarized (LP) modes. The weakly guided modes have the same propagation constants and are linearly polarized along the x-axis and the y-axis, respectively. In addition to the simplication in the analysis and the ease in understanding the mode phenomena, Gloge has shown that it is possible to calculate the fields in the fiber and the characteristic equations of LP modes directly from Maxwell's equations [54].

The properties of the LP modes imply that the solution $\psi(r,\phi)$ in Equation (5.1-2) can be considered as a representation of the LP_{jm} (the first subscript denotes the Bessel function of the first kind of order v, the second represents the zeros of the Bessel function). Table 5.3-1 shows the correspondence between the exact modes of a circularly symmetric fiber and the approximated LP modes [58]. Continuity of the fields and the derivatives $\partial\psi/dr$ at the interface then lead us to the following solutions for the wave equation

$$\psi(r,\phi)=\begin{Bmatrix}\dfrac{AJ_j\left(\dfrac{Ur}{a}\right)}{J_j(U)}\\[2ex]\dfrac{AK_j\left(\dfrac{Wr}{a}\right)}{K_j(W)}\end{Bmatrix}\begin{pmatrix}\cos(j\phi)\\ \sin(j\phi)\end{pmatrix}\qquad\begin{Bmatrix}r<a\\ r>a\end{Bmatrix}, \tag{5.3-1}$$

as well as the characteristic equation

$$\frac{UJ_{j-1}(U)}{J_j(U)}=-\frac{WK_{j-1}(W)}{K_j(W)}. \tag{5.3-2}$$

Upon solving (5.3-2) for β it will be found that only discrete values restricted to the range $k_0 n_2 < \beta < k_0 n_1$ will be allowed to exist in the fiber. Equation (5.3-2) is a complicated expression that is typically solved using numerical methods and the solutions for any particular mode will provide all the information of that mode. The number of modes that can exist in a waveguide as a function of the normalized frequency V may be conveniently represented in terms of a normalized propagation constant *b* defined by [54,59]

$$b = \frac{(\beta/k)^2 - n_2^2}{n_1^2 - n_2^2}. \tag{5.3-3}$$

Figure 5.3-1 is a plot of the dispersion curves derived from the characteristic equation for a few of the low-order modes. A mode is defined to be in cut off when $\beta/k = n_2$ or b=0. In Chapter 6 we will investigate the behavior of the spectral estimation algorithm as a function of these characteristic fiber parameters.

Table 5.3-1. Linearly polarized mode structures.

Exact Modes	LP Modes
HE_{1m}	LP_{0m}
$HE_{2m} + TM_{0m} + TE_{0m}$	LP_{1m}
$HE_{(v+1)m} + EH_{(v-1)m}$	LP_{vm}

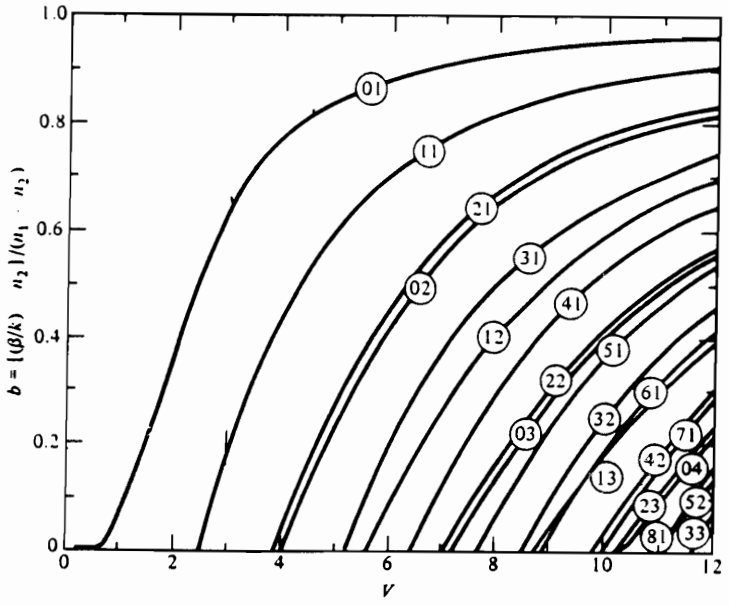

Figure 5.3-1. Plot of the normalized propagation constant b as a function of V for various LP_{jm} mode [54].

5.4 Coupling Between Waveguide Modes

In analyzing the optical waveguide we have assumed that the cladded-core fiber was perfectly straight, and had a circularly symmetric geometry with homogeneous material of constant refractive index in the core, cladding and jacket region. Any deviations from the constant average refractive index values were assumed to consist of random fluctuations correlated over short distances compared to the wavelength of the light. Such microscopic index fluctuations causing Rayleigh scattering of the guided mode to the radiation mode is usually considered as a bulk loss by a contribution to the imaginary component of the propagation constant. Actual fibers, however, are never quite perfect. Aside from the microscopic fluctuations due the random molecular structure of the material, the index also deviates macroscopically from its nominally symmetric circular symmetry. Furthermore, the fiber will never be straight as it is subjected to both microbends and macrobends particularly when it is embedded into another material [56-58].

All these deviations of the fiber from the ideal geometry and refractive index distribution lead to coupling of power among the modes. If the fiber guides only the fundamental mode, perturbations cause power coupling from the guided mode to leaky and radiation modes. In an ideal optical fiber, the evanescent fields are made to decay by using infinitely thick cladding region. Conventional optical fiber uses the lossy jacketing material surrounding the cladding to suppress the radiation modes. Because of the finite cladding thickness imposed by a practical fiber system, the cladding region also guides electromagnetic radiation but supports discrete cladding modes [58-61]. Thus, power in the fundamental guided mode is coupled to these discrete cladding modes. Since mode coupling is a wavelength dependent mechanism, our analysis of the fiber-based Fabry-Perot interferometric sensor must therefore account for these wavelength selective losses.

We can treat the situations of guided wave fiber optics involving the exchange of power between modes by means of the coupled-mode approach [62]. The formalism describes the total propagation disturbances in a structure as a sum of unperturbed modes of the system whose amplitude vary with distance *z* due to some coupling between them. In the following sections we will reproduce some of the main features of this theory but develop the coupled mode equations by proving that the modal fields in the optical fiber are orthogonal to one another.

5.4.1 Coupled-Mode Equations

We began by supposing that the following vector fields exist in an optical waveguide

$$\left.\begin{matrix}\overline{E}_u, & \overline{H}_u \\ \overline{E}_v, & \overline{H}_v\end{matrix}\right\} \quad \left\{\begin{matrix}n_u(r,\phi,z) \\ n_v(r,\phi,z)\end{matrix}\right\}, \tag{5.4.1-1}$$

and satisfy Maxwell's curl equations

$$\nabla \times \overline{H} = j\omega\varepsilon\overline{E} \tag{5.4.1-2}$$

$$\nabla \times \overline{E} = -j\omega\mu\overline{H} \tag{5.4.1-3}$$

We apply (5.4.1-2) to mode *v* and take the dot product of the complex conjugate of this equation with E_u

$$\overline{E}_u \cdot \nabla \times \overline{H}_v^* = -j\omega\varepsilon_v \overline{E}_v^* \cdot \overline{E}_u . \tag{5.4.1-4a}$$

Similary we apply (5.4.1-3) to mode *u* and take the dot product of the complex conjugate of this equation with H_u

$$-\overline{H}_u \cdot \nabla \times \overline{E}_v^* = -j\omega\mu_v \overline{H}_v^* \cdot \overline{H}_u . \tag{5.4.1.-4b}$$

Applying (5.4.1-2) to mode u and taking the dot product with E^*_v leads to

$$\overline{E}^*_v \cdot \nabla \times \overline{H}_u = j\omega\varepsilon_u \overline{E}_u \cdot \overline{E}^*_v , \qquad (5.4.1\text{-}4c)$$

and similarly applying (5.4.1-3) to mode u and taking the dot product with H^*_v produces

$$-\overline{H}^*_v \cdot \nabla \times \overline{E}_u = j\omega\mu_u \overline{H}_u \cdot \overline{H}^*_v . \qquad (5.4.1\text{-}4d)$$

Integrating the sum of Eqns. (5.4.1-4a) to (5.4.1-4d) yields

$$\int_V \nabla \cdot \overline{F}\, dV = \int_V \left(j\omega(\varepsilon_u - \varepsilon_v)\overline{E}_u \cdot \overline{E}^*_v \right) dV , \qquad (5.4.1\text{-}5)$$

where we define $\overline{F} = \overline{E}^*_v \times \overline{H}_u + \overline{E}_u \times \overline{H}^*_v$. Invoking the divergence theorem to a volume of infinitesimal thickness in z on the left side of (5.4.1-5) leads to a useful vector identity of the form [17]

$$\int_V \nabla \cdot \overline{F}\, dV = \int_S \frac{\partial}{\partial z}\left(\overline{F} \cdot \hat{z}\right) dS + \oint_{L_S} \overline{F} \cdot \hat{n}\, dL , \qquad (5.4.1\text{-}6)$$

where S indicates an area integration in the r,ϕ plane, and L_S is a line integral extended over an infinitely large circle around this area. $\hat{z}$ is a unit vector in the z-direction and $\hat{n}$ is an outward normal unit vector from the contour L_S. If one or both of the modes are guided modes of the waveguide, their field strength at infinity vanishes and the line integral goes to zero. The line integral also vanishes when both modes are radiation modes of the structure [56,61]. Changing the right hand side of (5.4.1-5) into a surface integral we obtain

$$\int_{z=\text{constant}} \frac{\partial}{\partial z}\left(\overline{E}^*_v \times \overline{H}_u + \overline{E}_u \times \overline{H}^*_v\right) dS = j\omega \int_{z=\text{constant}} (\varepsilon_u - \varepsilon_v)\overline{E}_u \cdot \overline{E}^*_v dS, \qquad (5.4.1\text{-}6a)$$

or

$$(\beta_v - \beta_u)\int_S \left(\overline{E}_v^* \times \overline{H}_u + \overline{E}_u \times \overline{H}_v^*\right) dS = j\omega\varepsilon_o \int_S \left(n_u^2 - n_v^2\right)\overline{E}_u \cdot \overline{E}_v^* dS. \qquad (5.4.1\text{-}6b)$$

Being more specific in defining the modal fields of the optical waveguide, the forward propagating electromagnetic fields of a lossless cylindrical uniform system characterized by ε_u are of the form

$$\overline{E}_u(r,\phi,z) = a_0(z)\left[\hat{e}_{uz}(z) + \hat{e}_{ut}(r,\phi)\right]\exp(-j\beta_u z), \qquad (5.4.1\text{-}7a)$$

and

$$\overline{H}_u(r,\phi,z) = a_0(z)\left[\hat{h}_{uz}(z) + \hat{h}_{ut}(r,\phi)\right]\exp(-j\beta_u z), \qquad (5.4.1\text{-}7b)$$

where β_u is the modal propagation constant, $\hat{h}_{ut}(r,\phi)$ and $\hat{e}_{ut}(r,\phi)$ represent transverse fields independent of the z-axis found from the solutions of the transverse wave equation. A similar representation applies to the modal fields *v*. Substituting (5.4.1-7a) and (5.4.1-7b) into (5.4.1-6b) and assuming that there is no perturbation applied to the optical fiber ($n_u^2 = n_v^2$), the right hand side of (5.4.1-6b) vanishes. In order to prove power orthogonality, we allow the backward traveling fields to propagate in the optical fiber, and thus obtain from (5.4.1-6b)

$$(\beta_v - \beta_u)\int_S \left(-\hat{e}_{vt}^* \times \hat{h}_{ut} + \hat{e}_{ut} \times \hat{h}_{vt}^*\right) dS = 0, \qquad (5.4.1\text{-}8a)$$

and

$$(\beta_v - \beta_u)\int_S \left(\hat{e}_{vt}^* \times \hat{h}_{ut} + \hat{e}_{ut} \times \hat{h}_{vt}^*\right) dS = 0, \qquad (5.4.1\text{-}8b)$$

for the backward and forward propagating modes, respectively. Taking the sum of (5.4.1-8a) and (5.4.1-8b), we can now show that nondegenerate modes are orthogonal via the following relations [53,58]

$$\int_S \left(\hat{e}^*_{vt} \times \hat{h}_{ut}\right) dS = 0,$$
$$\int_S \left(\hat{e}_{ut} \times \hat{h}^*_{vt}\right) dS = 0. \tag{5.4.1-9}$$

Any arbitrary field distribution of the optical waveguide can be expressed in terms of the orthogonal modes of the guide. It is thus possible to write

$$\overline{H}_v(r,\phi,z) = \sum_{m=1}^{N} a_m(z)\hat{h}_{vt}(r,\phi)\exp(-j\beta_{v_m} z), \tag{5.4.1-10a}$$

and

$$\overline{E}_v(r,\phi,z) = \sum_{m=1}^{N} a_m(z)\hat{e}_{vt}(r,\phi)\exp(-j\beta_{v_m} z), \tag{5.4.1-10b}$$

where the subscript *t* represents a transverse vector in the r,ϕ plane, label *m* denotes a particular orthogonal mode in the waveguide, and $a_m(z)$ is the modal coefficient. Substituting Equation (5.4.1-10) into (5.4.1-5) leads to a general differential equation for mode propagation in a perturbed waveguide from which the modal coefficients $a_m(z)$ can be determined [56,57,60,61]

$$\frac{da_m(z)}{dz} = \sum_{m=1}^{N} a_m(z)\exp\left(j\Delta\beta_{uv_m} z\right) C_{uv_m}, \tag{5.4.1-11}$$

where

$$\Delta\beta_{uv_m} = \beta_u - \beta_{v_m}, \tag{5.4.1-12}$$

and the coupling coefficient C_{uv_m} independent of z is defined as [58]

$$C_{uv_m} = \frac{\omega\varepsilon}{2j} \frac{\int_S \left(n_u^2 - n_v^2\right) \hat{e}_{ut} \cdot \hat{e}^*_{v_m t} dS}{\int_S \left(\hat{e}^*_{v_m t} \times \hat{h}_{ut} + \hat{e}_{ut} \times \hat{h}^*_{v_m t}\right) \cdot dS}. \tag{5.4.1-13}$$

Equations (5.4.1-11) through (5.4.1-13) represent an extremely complicated systems of coupled amplitude equations since *u* and *v* extend over all modes (discrete and continuous). Due to the complexity of these coupled mode fields, the calculations of the differential propagation constant in (5.4.1-12) and the coupling coefficients in (5.4.1-13) are generally evaluated using numerical techniques.

In deriving (5.4.1-11) through (5.4.1-13), we took an alternate approach by proving that the modes in the optical waveguide are orthogonal to each other in order to arrive at these equations. Nevertheless, the resulting expressions obtained by this approach are equivalent to that obtained by Marcuse [56] using perturbation theory, and Snyder [61] and Yariv [13,60] using coupled mode theory.

Finally, the value of $\Delta\beta$ called the phase matching condition is equal to the difference between the propagation constants of the two coupled modes. Careful examination of Equation (5.4.1-8) shows that in order to sustain a cumulative exchange of power between two modes, the phase matching condition must vanish. Otherwise, the values of $da_m(z)/dz$ from different parts of the propagation path interfere destructively. In a mode coupling situation, traveling mode *u* interacts with the perturbation to yield a traveling polarization wave. The polarization wave in turn excites mode *v*. Simultaneously, mode *v* interacts with the perturbation to drive mode *u*. When $\Delta\beta = 0$ power exchange between mode *u* and *v* is sustained [60].

6. Error Analysis of Distortion Effects

The transmission performance of an optical fiber is characterized by three global parameters: 1) the cutoff wavelength of the second order mode, λ_c, defining the spectral region of singlemode operation, 2) the mode field diameter (MFD), measuring the width of the modal intensity pattern, and 3) the chromatic dispersion which is expected to have minimal impact on the performance of the interferometer because of the short lead length used in typical fiber sensing applications. The objective of this chapter is to discuss how these parameters affect the spectral estimation algorithm. This chapter also discusses how wavelength selective attenuation induced by microbends and macrobends can impair the operation of the fiber-based Fourier transform spectroscopy. We will use coupled-mode theory and the approximated LP mode solutions derived in Chapter 5 to develop the modeling simulations. An extensive error analysis of chromatic distortion caused by modal interference, mode field diameter changes, microbends is also presented.

6.1 Modal Interference

The cutoff wavelength of the LP_{11} mode is a very important parameter because it indicates the wavelength region where the optical fiber can be used in singlemode applications. The theoretical cutoff wavelength can be deduced from the corresponding cutoff normalized frequency as

$$\lambda_c = \frac{2\pi a \Delta}{V_{11}}, \tag{6.1-1}$$

where V_{11} is the first solution of the characteristic Equation (5.3-2), and Δ is defined in Equation (5.2-1). The normalized frequency depends on the particular refractive index profile of the fiber. For a singlemode step-index fiber, the normalized cutoff frequency V_{11} is equal to 2.405. If the LP_{11} mode is allowed to propagate in the optical fiber, modal interference may occur. Interactions or interference of the fundamental mode and the LP_{11} mode can occur if the optical path length difference between the modes is less than the coherence length of the source or if the light emitting diode operates with wavelengths that fall below the cutoff wavelength of the optical fiber [21]. The interference signal that occurs is due to the superposition of two lower order modal fields,

$$I(r,\phi,z) = \left(E_{01} + E_{11}\right)^{1/2}, \tag{6.1-2a}$$

where

$$E_{01}(r,\phi,z) = E_0 J_0(q_{01} r) \exp(\omega t - j\beta_{01} z), \tag{6.1-2b}$$

is the electric field of the fundamental mode obtained from Equation (5.1-3) and

$$E_{11}(r,\phi,z) = E_1 J_1(q_{11} r) \cos(\phi) \exp(\omega t - j\beta_{11} z) \tag{6.1-2c}$$

is the electric field describing the LP_{11} mode. The argument q_{vm} is defined by Equation (5.1-4). It should be noted that for all modes, degeneracies can exist in terms of polarization states. For the LP_{01} mode, two polarization states may exist (x and y polarization) depending upon the launch and environmental conditions [56-58].

Polarization birefringence may also exist if the index in the fiber is anisotropic. For most practical applications, the polarization birefringence is minimal, and thus typically ignored. For the LP_{11} mode, there are four-fold degeneracy resulting from a combination of polarization effects and the periodic dependency on the azimuthal direction ϕ, termed odd or even. As a simplification to our analysis we will assume that only the even LP_{11} mode is excited.

Expansion of Equation (6.1-1) using Equations (6.1-2b) and (6.1-2c) leads to an interference pattern [63]

$$I(r,\phi,z) = J_0^2(q_{01}r) + J_1^2(q_{11}r)\cos^2(\phi) \quad + \\ 2J_0(q_{01}r)J_1(q_{11}r)\cos(\phi)\cos(\Delta\beta z), \tag{6.1-3}$$

where $\Delta\beta=\beta_{01}-\beta_{11}$ is the differential propagation constant. The first two terms contribute to a bias that remains constant across the imaging surface of the CCD array. The third term has a cosine term that varies as a result of the difference in the propagation constants between the two modes. Measurement of the overall intensity output will remain constant, but the intensity distribution oscillates between the two lobes of the LP_{11} mode.

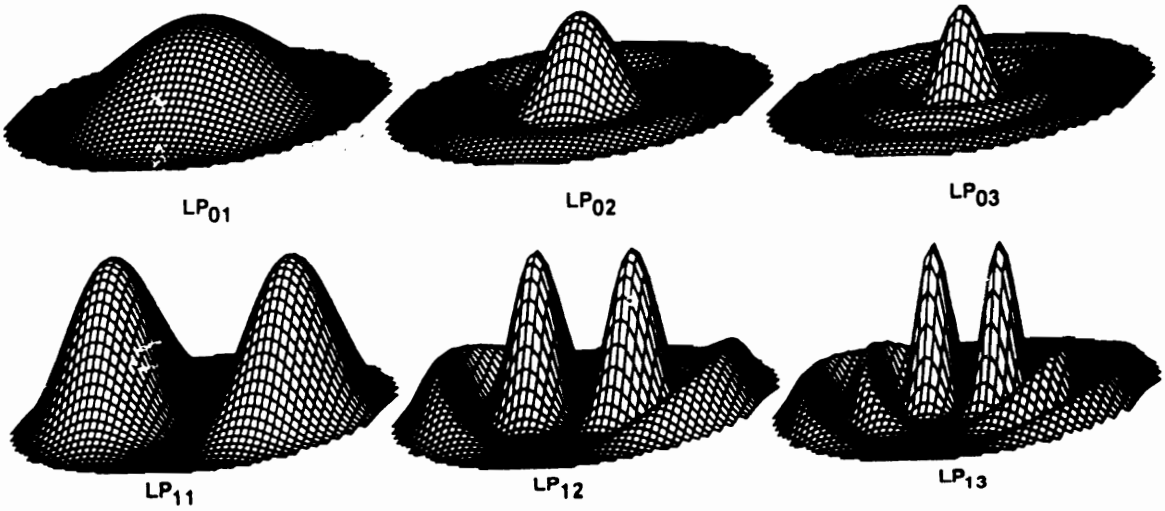

Figure 6.1.1-1. Intensity profile of several lower order LP modes.

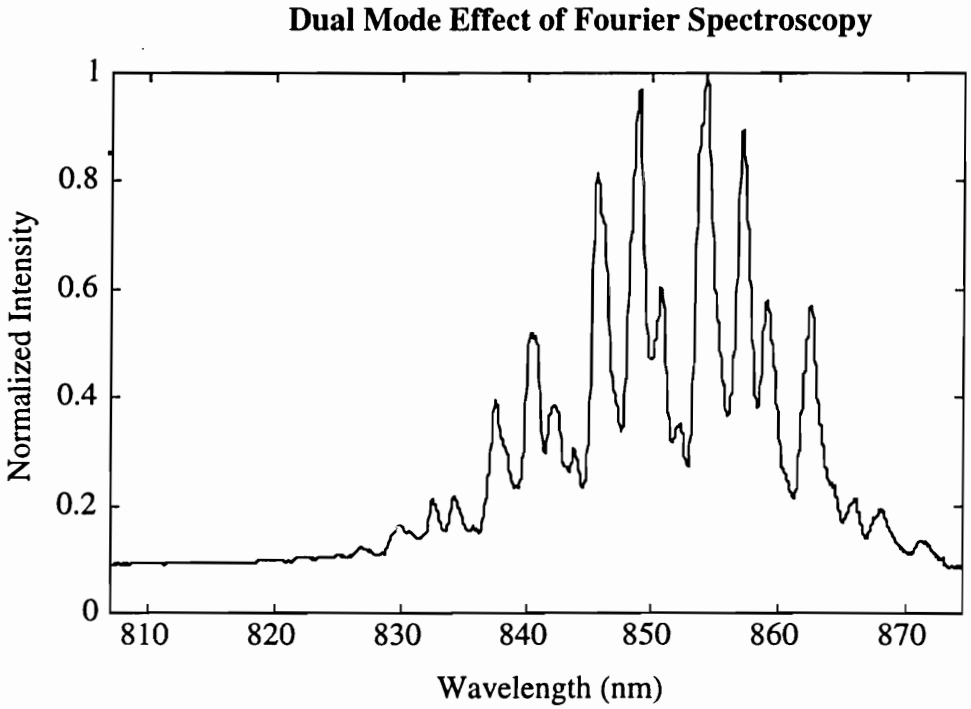

Figure 6.1.1-2. Chromatic distortion of Fourier transform spectroscopy caused by modal interference.

6.1.1 Effects of Modal Interference on Fourier Spectroscopy

Interrogation of a dual mode interferometer by the spectrometer produces a combination of chromatic distortion and spurious signal harmonics. Chromatic distortion is easy to understand since the profile of the fundamental guided mode differs from the LP_{11} guided mode as illustrated in Figure 6.1.1-1. The intensity profiles illustrated in Figure 6.1.1-1 for two guided modes are based on Equation (5.3-1). Figure 6.1.1-2 graphically illustrates the effect of modal interference on a Fabry-Perot interferometer fabricated with a 9 micrometer core diameter optical fiber (singlemode at 1300 nm) and operated with a 830 nanometer source. Figure 6.1.1-2 clearly shows the chromatic distortion effect. Depending on the input condition, the power spectral density of the harmonic component may exceed the fundamental frequency, thus causing spectral estimation error.

If we now combine the modal interference from Equation (6.1-3) with the simple interference model of the Fabry-Perot in Equation (3.0-4), the output intensity arriving at the imaging array takes the following form

$$I(r,\phi,z) = 2I_0\left[1+\cos\left(\phi_{gap}+\phi_{\Delta\beta}\right)\right], \qquad (6.1.1\text{-}1)$$

where

$$\phi_{gap} = \frac{4\pi d}{\lambda} + \phi_o, \text{ and} \qquad (6.1.1\text{-}2a)$$

$$\phi_{\Delta\beta} = \Gamma\cos(\Delta\beta z), \qquad (6.1.1\text{-}2b)$$

is the phase shift due to modal interference with

$$\Gamma = 2J_0(q_{01}r)J_1(q_{11}r)\cos(\phi), \tag{6.1.1-3}$$

being the amplitude of the phase shift. Equation (6.1.1-1) accounts for most phase modulation mechanisms that occur when the optical fiber is used as the waveguiding medium in a Fabry-Perot interferometer. The expression shown in Equation (6.1.1-1) does not, however, show the cause of signal harmonics when a dual-mode optical fiber is used. A more meaningful interpretation of the intensity equation can be obtained if we perform a series expansion of the cosine dependence in terms of the Bessel function to produce

$$I(r,\phi,z) = 2I_o\left\{\begin{array}{l} 1+\left[J_o(\Gamma)+2\sum_{n=1}^{\infty}J_{2n}(\Gamma)\right]\cos(\Delta\beta z)\cos\left[2n\left(\frac{4\pi d}{\lambda}+\phi_o\right)\right] \\ -\left[2\sum_{n=1}^{\infty}J_{2n-1}(\Gamma)\right]\cos(\Delta\beta z)\sin\left[(2n+1)\left(\frac{4\pi d}{\lambda}+\phi_o\right)\right] \end{array}\right\}, \tag{6.1.1-4}$$

where we have used the identities [26]

$$\cos(A\cos\theta) = \left[J_o(A)+2\sum_{n=1}^{\infty}(-1)^n J_{2n}(A)\right]\cos(2n\theta) \tag{6.1.1-5a}$$

and

$$\sin(A\sin\theta) = \left[2\sum_{n=0}^{\infty}(-1)^n J_{2n+1}(A)\right]\sin[(2n+1)\theta]. \tag{6.1.1-5b}$$

Equation (6.1.1-4) now clearly illustrates that in addition to the fundamental frequency component, modal interference in the optical fiber also induces an infinite number of harmonic distortion components. Equations (6.1.1-1) through (6.1.1-5) also illustrate the

difficulty in predicting and removing the distortion due to its dependence on a multitude of waveguide parameters.

Several methods have been employed to minimize harmonic distortion. One simple approach is to use a mandrel wrap to strip-off the LP_{11} mode. However, mode stripping is only a temporary solution. When the sensor is disconnected and reconnected from the demodulation system, a change in the injection condition may re-excite the LP_{11} mode. Thus, mandrel wrapping is effective only when the sensor is permanently affixed to the demodulation system. The second approach of minimizing the errors is handled by the signal processing electronics. Digital filters can be used to remove the distortion if the fundamental frequency component is sufficiently well separated from the harmonic signals. A disadvantage for using digital filters is that additional computation is needed to implement the filtering algorithm, and this may degrade the frequency response of the demodulation system.

6.2 Mode-Field Diameter

The mode-field diameter is another characteristic of the optical fiber that has a strong influence on the resolution of the spectral estimation since it determines the spread of the pattern incident on the diffraction grating. The output from the diffraction grating depends on the spread angle at the input and thus each wavelength component may excite a certain number of pixels on the CCD array. We have shown in Chapter 4 that the wavelength spacing across the CCD array is nonlinear. When the same output signal illuminates a different part of the CCD array, the digitized signal changes its frequency and introduces error in the spectral estimation.

6.2.1 Derivation of Mode-Field Distribution

The width of the electromagnetic field can be defined in several different ways. Depending on the choice from which the measurement of the guided field intensity distribution is performed, two distinct definitions of practical significance can be given for the spot size *d* and the MFD *w*. The spot size and MFD are related simply by the relation $d = 2\sqrt{2}w$[58]. Experiments have shown that shifts in the source wavelength and bends in the optical fiber will change the MFD. Consequently, the MFD affects the spectral estimation. The mode-field diameter can be defined in two regions, the near-field and the far-field. In the near-field definition the fundamental mode intensity pattern is detected from a point very close to the fiber end-face. In the near-field, the intensity pattern is proportional to the radial distribution of power into the fiber

$$I(r) \propto \psi^2(r), \tag{6.2.1-1}$$

where $\psi(r)$ is the field distribution of the LP_{01} mode from Equation (5.1-2). A standard approach used for defining the near-field spot size w_n is to use the root mean square (RMS) width of the near-field intensity distribution I(r) [56]

$$w_n = \left\{ \frac{\int_0^\infty r^2 \psi^2(r) r \, dr}{\int_0^\infty \psi^2(r) r \, dr} \right\}^2 . \tag{6.2.1-2}$$

In the grating demodulation system, the imaging plane of the CCD array is far from the output face of the fiber, that is, in the far-field region. Here, the effect due to free space propagation must be taken into account. Assuming that the imaging distance R from the fiber endface is large such that $R >> w_n^2/\lambda$, the effect of free-space propagation must be

considered by means of the theory of diffraction via Fraunhofer conditions [1]. Choosing a coordinate system (R,θ) as in Figure 6.2.1-1, the diffracted field takes the form [65]

$$\Psi(R,p) = \frac{ik_o}{R}\exp(ik_oR)\cos\theta\ F(p), \qquad (6.2.1\text{-}3)$$

where $k_o = 2\pi/\lambda$ is the vacuum wavenumber and $p=k_o\sin(\theta)$ is the angular propagation constant. The function F(p) above is dependent on the distribution of the modal field. Usually in calculations of interest, the term $\cos(\theta)$ can be taken to be unity, since at large angles the radiation pattern is faint. Under this assumption, F(p) is related to the near-field $\psi(r)$ by the cylindrical Fourier transform [58]

$$F(p) = \int_o^\infty \psi(r)\, J_o(pr)dr. \qquad (6.2.1\text{-}4)$$

The far-field intensity $F^2(p)$ represents the angular distribution of the output power of the singlemode fiber. Therefore, considering that the light beam radiated by the fiber is diffraction limited, that is, its angular width is approximately given by the reciprocal of its radial width, the far-field spot size w_f is defined as [55,63]

$$w_f = \left\{ \frac{\int_o^\infty F^2(p)p\ dp}{\int_o^\infty p^2F^2(p)p\ dp} \right\}^{1/2}, \qquad (6.2.1\text{-}5)$$

which is inversely proportional to the RMS width of the angular intensity distribution $F^2(p)$. Making use of well-known Fourier transforms properties, the far-field MFD can be derived directly from the field distribution of the propagation mode, viz. [58,66,67]

$$w_f = \left\{ \frac{\int_0^\infty \psi^2(r) r \, dr}{\int_0^\infty (d\psi/dr)^2 r \, dr} \right\}^{1/2} . \qquad (6.2.1\text{-}6)$$

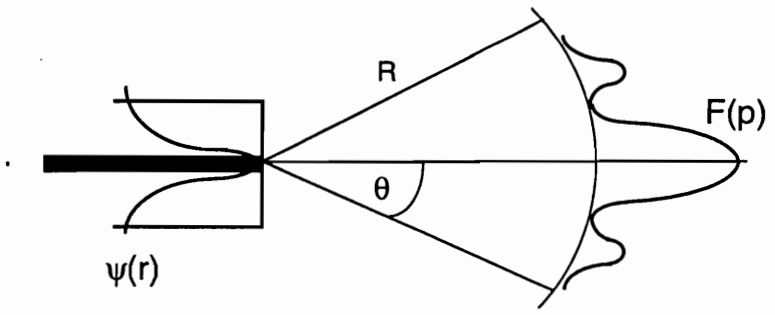

Figure 6.2.1-1. Coordinate system of the radiation pattern of the fiber in the Fraunhofer region (far-field).

6.2.2 Approximated Width of Guided Mode

The weak-guidance approximation described in Section 5.2 greatly simplifies the determination of the modal fields of optical waveguides, because it depends on solutions of the scalar wave equation rather than on vector solutions of Maxwell's equations. For circular optical fibers, with an arbitrary profile, the scalar wave equation must normally be solved using numerical methods. These solutions, including those for profiles of practical interest such as the step and clad power-law profiles, are given in terms of special functions or by series expansions, which usually necessitate tables or numerical evaluation to reveal the physical attributes of the modes. Because the fundamental mode intensity pattern is approximately Gaussian, we can take advantage of the simplicity of the Gaussian description and readily elucidate the physical attributes of a general profile

by assuming that the fundamental mode field distribution of an arbitrary profile can be approximated by some Gaussian function. For the guided mode near the core region of a step-index singlemode optical fiber, the field distribution is approximated very well with a Gaussian function having a spot size d [56]

$$\psi(r) = \exp\left[-\frac{r^2}{d^2}\right]. \qquad (6.2.2\text{-}1)$$

Note that in this notation, d describes the width of the electric field distribution but not the width of the energy distribution or mode field diameter which is narrower (by a factor of $2\sqrt{2}$). Note also that far away from the core, the Gaussian function is a poor approximation for the guided mode, since it is known that its field tail deep inside the cladding decays exponentially and not according to a Gaussian distribution. Therefore, the Gaussian approximation is only suitable for problems involving the field at or near the fiber core but not far from the core.

In Figure 6.2.2-1 the far-field spot size is plotted as function of the wavelength for a conventional singlemode step-index fiber. We have experimentally demonstrated in Section 4.3 how changes in the mode-field diameter introduces errors to the spectral estimation algorithm. In this section we have derived the exact and approximate mathematical expressions relating the mode-field diameter to the parameters characterizing the optical fiber.

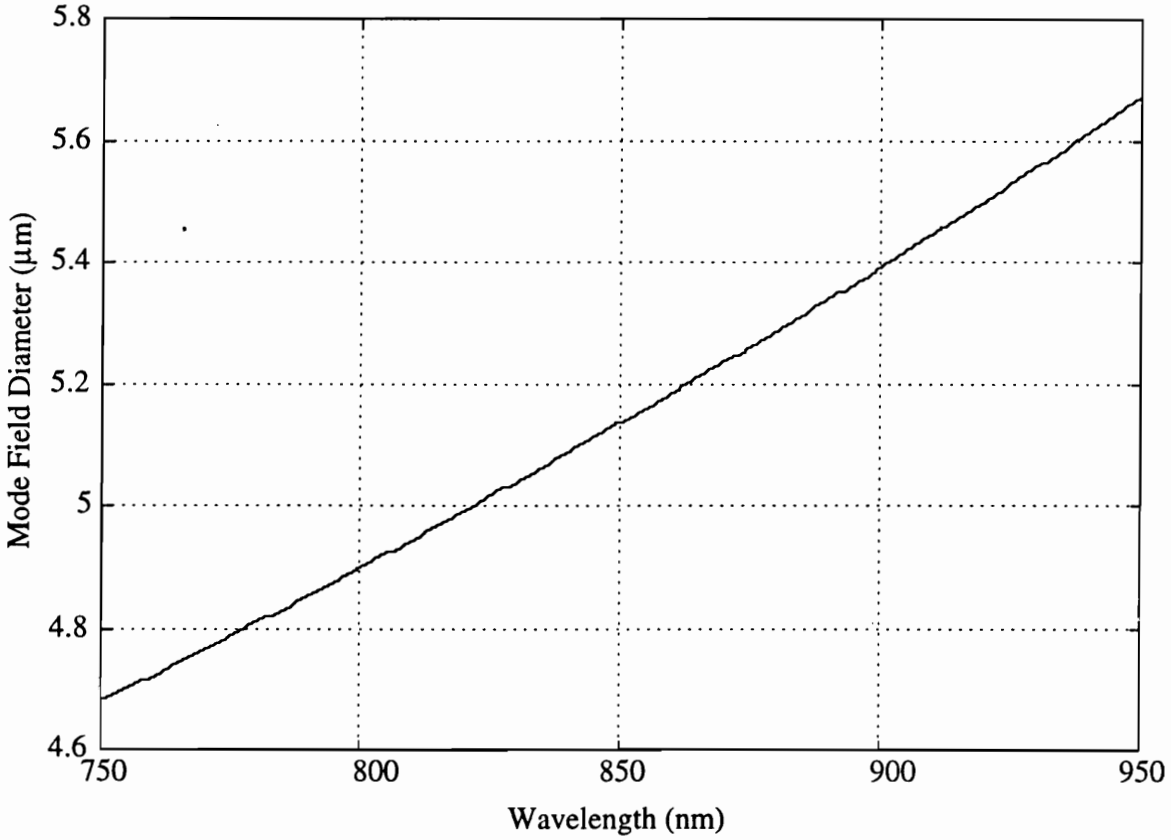

Figure 6.2.2-1. Far-field spot size w_f versus wavelength for a step index singlemode fiber (Spectran 830 nm singlemode - Pyrocoat SMC-A0820B).

6.3 Periodic Microbends

Of all the waveguide distortion mechanisms, optical losses due to microbends are the most difficult to mitigate because the attenuation is wavelength selective. Microbend-induced optical losses occur when optical power from the fundamental mode is coupled to the discrete cladding modes. Experimental and theoretical analysis by Marcuse [68], Probst [69], Peterman [70] and Bjarklev [71] have shown that when an optical fiber is exposed to the action of periodically repeated microbends, significant wavelength-dependent losses will occur due to the wavelength selective nature of mode coupling. There are two conditions that must be satisfied by the fiber before mode coupling occurs. If the microbends satisfy the phase matching condition, and the mode field overlap integral is nonzero, then strong spectral attenuation will occur at discrete wavelengths[56,57,60,61,64]. The purpose of this section is to investigate how these wavelength dependent losses affect the spectral estimation algorithm.

6.3.1 Microbend Loss Formulas

The derivation of the microbend loss formula is based on perturbation theory which describes the coupling between the guided mode and the cladding modes of a distorted singlemode fiber. The coupling strength between modes of an arbitrary waveguide (guided or radiation modes) as derived in Chapter 5 is generally described by the coupling coefficient having the form

$$C_{\mu\nu} = \frac{\omega\varepsilon_0}{4iP}\int_{-\infty}^{\infty}\left(n^2 - n_0^2\right) E_\mu^* E_\nu \, dS, \qquad (6.3.1\text{-}1)$$

where P is the total guided power, and n^2 - n_0^2 is the differential refractive index between the two modes. The capital letters E_μ and E_ν represent the electric field vectors of the coupled modes without their time and z variation, and the subscript μ and ν label the guided and radiation modes. The radiation loss associated with the coupling of the fundamental guided mode to the radiation mode for a circularly symmetric optical waveguide caused by a perturbation of the refractive index profile may be obtained from the expression [57,68]

$$2\alpha_m = \sum_{p=1}^{\infty} C_{vm}^2(\lambda)\, \Phi(\Delta\beta_{vm}), \tag{6.3.1-2}$$

where

$$C_{vm}(\lambda) = \frac{k}{2} \frac{\int_0^{\infty}\int_0^{2\pi} \frac{\partial n_o}{\partial r} \psi_{01}(\lambda)\psi_{vm}(\lambda) r\, dr\, d\phi}{\left(\int_0^{\infty}\int_0^{2\pi} \psi_{01}^2(\lambda) r\, dr\, d\phi \int_0^{\infty}\int_0^{2\pi} \psi_{vm}^2(\lambda) r\, dr\, d\phi \right)^{1/2}} \tag{6.3.1-3}$$

is the normalized z-independent coupling coefficient derived from (6.3.1-1) which describes the coupling strength between the LP_{01} guided mode and the LP_{vm} discrete cladding mode. The attenuation formula of Equation (6.3.1-2) also includes the spatial power spectrum caused by the microbends and is given by Unger [57] as

$$\Phi(\Delta\beta_{vm}) = \frac{1}{2L} \int_{-L}^{L} f(z) \exp(-i\Delta\beta_{vm} z) dz. \tag{6.3.1-4}$$

The function f(z) in Equation (6.3.1-4) describes the random deformation of the fiber axis and is directly related to the perturbed refractive index through the following first order Taylor expansion [56,64]

$$n(r,\phi,z) = n_o(r) + \frac{\partial n_o}{\partial r} f(z)\cos(\phi). \qquad (6.3.1\text{-}5)$$

For a broad class of fibers, Gloge [72] showed that the unperturbed refractive index profile $n_o(r)$ can be described by the power-law

$$n_o(r) = \begin{cases} n_1\left[1 - \left(\frac{r}{a}\right)^g \Delta\right] & 0 < r < a \\ n_2 & r > a \end{cases} \qquad (6.3.1\text{-}6)$$

with core diameter *a*, and the relative refractive-index Δ described by Equation (5.2-1). For a step index optical fiber, $g \to \infty$.

Microbend-induced radiation loss caused by mode coupling must also satisfy the phase matching condition between the fundamental guided LP_{01} mode and the circularly symmetric LP_{vm} cladding mode, specifically [14,60,61]

$$\Delta\beta_{vm}(\lambda) = \beta_{01}(\lambda) - \beta_{vm}(\lambda) = \frac{2\pi}{\Lambda}, \qquad (6.3.1\text{-}7)$$

where Λ is the microbend period, $\beta_{01}(\lambda)$ and $\beta_{vm}(\lambda)$ are the wavelength dependent propagation constants of the LP_{01} guided mode and the LP_{vm} cladding mode respectively.

In the derivation of the microbend loss formula, the calculation of the values for $\beta_{01}(\lambda)$ and $\beta_{vm}(\lambda)$ forms the basis of the theoretical analysis for they are used in the initial computation of the spatial power spectrum. Once the differential propagation constant $\Delta\beta_{vm}(\lambda)$ is known to be a function of the wavelength, the phase matching condition of Equation (6.3-7) can be used to determine how the periodicity, Λ, induces mode coupling

at a particularly wavelength. High losses will occur at wavelengths where the spatial power spectrum peaks coincide with the positions of the coupling coefficients [57].

In order to find $\Phi(\Delta\beta_{vm})$ for the special case where the refractive index profile is deterministic such as perturbation due to a sinusoidal wall boundary, the deformation function f(z) can be defined as [60]

$$f(z) = Y_0 \sin\left(\frac{2\pi z}{\Lambda}\right), \tag{6.3.1-8}$$

where Y_0 gives the deformation amplitude. Substituting Equation (6.3.1-8) into (6.3.1-4), the spatial spectrum simplifies to

$$\Phi(\Delta\beta_{vm}) = \frac{Y_o^2 L}{2}\left\{\frac{\cos\left[\left(\frac{2\pi}{\Lambda}+\Delta\beta_{vm}\right)L\right]}{\left(\frac{2\pi}{\Lambda}+\Delta\beta_{vm}\right)L} + \frac{\cos\left[\left(\frac{2\pi}{\Lambda}-\Delta\beta_{vm}\right)L\right]}{\left(\frac{2\pi}{\Lambda}-\Delta\beta_{vm}\right)L}\right\}^2. \tag{6.3.1-9}$$

For random deformation period, we can express the spectral attenuation in terms of the autocorrelation function of the fiber and its Fourier transform. However, in practice neither the form of the autocorrelation function nor the values of the root-mean-square deviation and correlation length are known for actual fibers. Assuming a Gaussian correlation function, the spatial power spectrum is derived from the Wiener-Khinchin theorem, viz., [23,68]

$$\Phi(\Delta\beta_{vm}) = \int_{-\infty}^{\infty} R(u)\cos(\theta u)du, \tag{6.3.1-10}$$

where R(u) is the autocorrelation function

$$R(u) = \sigma^2 \langle f(z) f(z+u) \rangle. \qquad (6.3.1\text{-}11)$$

With the assumption that the deformation is a Gaussian random process, the autocorrelation function is then [23,68]

$$R(u) = \sigma^2 \exp\left[-\left(\frac{u}{L_c} \right)^2 \right], \qquad (6.3.1\text{-}12)$$

where σ^2 is the rms deviation of the distortion function f(z), and L_c is the correlation length. The spatial power spectrum of the random fiber distortion function then becomes[57,60]

$$\Phi(\Delta\beta_{vm}) = \sqrt{\pi}\, \sigma^2 L_c \exp\left\{ -\left[\frac{1}{2} (\beta_{01} - \beta_{vm}) L_c \right]^2 \right\}. \qquad (6.3.1\text{-}13)$$

6.3.2 Approximations for the Microbend Loss Formulas

To simplify the computation of the microbend loss formula, particularly in the calculation of the propagation constants $\beta_{01}(\lambda)$ and $\beta_{vm}(\lambda)$, approximations from the weakly-guiding method proposed by Gloge can be employed [44]. The propagation constant of the fundamental guided mode, $\beta_{01}(\lambda)$, for a step-index fiber is obtained from Equation (5.2-2a) by the expression

$$\beta_{01}(\lambda) = \sqrt{k_1^2(\lambda) - \left(\frac{U(\lambda)}{a} \right)^2}, \qquad (6.3.2\text{-}1)$$

where $k_1^2(\lambda) = k_o n_1 = \frac{2\pi}{\lambda} n_1$. The parameter U is a wavelength dependent function that can be approximated by [57]

$$U(\lambda) = \frac{(2.405)V}{1+(4+V^4)^{0.25}}. \qquad (6.3.2\text{-}2)$$

Using Equation (6.3-2-1), $\beta_{0l}(\lambda)$ may be estimated for any wavelength if the parameters of the fiber are known. This is followed by the computation of the propagation constant for the circularly symmetric cladding modes $\beta_{vm}(\lambda)$ and may be approximated using

$$\beta_{vm}(\lambda) = \sqrt{k_2^2(\lambda) - \left(\frac{U(\lambda)}{b}\right)^2}, \qquad (6.3.2\text{-}3)$$

with $k_2^2(\lambda) = k_o n_2 = 2\pi n_2/\lambda$, and *b* is the cladding radius. It should be noted that since the fundamental guided mode is independent of ϕ, the coupling coefficients have nonvanishing values only for the LP_{vm} cladding modes which have the same ϕ-dependence as the index perturbation. This property thus excludes the coupling of the guided mode to the circularly symmetric LP_{1m} cladding mode. Furthermore, only the first order Bessel functions need to be considered since the coupling coefficients defined by Equation (6.3.1-2) vanish for the higher order cladding modes.

From the weakly guidance analysis approach, we may assume that the presence of the core has a negligible effect on the cladding modes and that the refractive-index discontinuity at the outer cladding boundary (r = b) is sufficiently large. With these assumptions, we can express the cladding modes as [55,56,57]

$$E_{lm}(r,\phi,z) = E_{lm} J_l(q_l r)\cos(\phi)\exp(\omega t - j\beta_{lm} z), \qquad (6.3.2\text{-}4)$$

and the guided mode being given by Equation (6.1-2b) or approximated by a Gaussian profile using (6.2.2-1).

Finally, in order for us to investigate the performance degradation caused by the wavelength selective attenuation, we can either incorporate the microbend radiation loss formula to the spectral estimation algorithm in the time domain or in the frequency domain. Since the optical attenuation presented here is readily recognized as a multiplicative effect,

$$P_r = \alpha P_g , \qquad (6.3.2\text{-}5)$$

where P_r and P_g are the radiated and guided optical power respectively. The complex field in the image plane of the CCD array is found by directly multiply the attenuation coefficient of Equation (6.3.1-2) with the intensity function of Equation (2.4-12)

$$I(\lambda) = \frac{\alpha_m T^2\left[1 - R^2 \exp(-4\pi\Delta\nu t_r)\right]}{\left[1 - R^2\right]\left\{\left[1 - R \exp(-2\pi\Delta\nu t_r)\right]^2 + 4R \sin^2(\pi\nu_0 t_r) \exp(-2\pi\Delta\nu t_r)\right\}}. \qquad (6.3.2\text{-}6)$$

The spectral estimation algorithm requires that the optical signal is converted to the frequency domain prior to being processed. For a linear system, we can calculate the Fourier transform of the wavelength selective attenuation separately from the amplitude modulated intensity interference pattern. In the frequency domain, we can express the impulse response of Equation (6.3.2-6) as a convolution operation

$$F\{I(\lambda)\} = F\{\alpha_m(\lambda)\} \otimes F\{I(\lambda)\}, \qquad (6.3.2\text{-}7)$$

where F denotes the Fourier transform operation, and ⊗ denotes the convolution operation given as

$$F\{\alpha_m(\lambda)\} \otimes F\{I(\lambda)\} = \int_{-\infty}^{\infty} \alpha_m(\lambda)\, I(f-\lambda)\, d\lambda. \qquad (6.3.2\text{-}8)$$

Equation (6.3.2-8) is a mathematical expression that allows us to gain insights into how periodic microbend induced losses affect the spectral estimation algorithm. In an actual experimental setup, we would not be able to separate out the spectral attenuation from the interference pattern and perform the convolution of the two expressions in the frequency domain. We would only have access to the composite expression illustrated in Equation (6.3.2-6) from which we would calculate the Fourier transform.

6.3.3 Sensitivity of Interferometers to Microbends

Using the above approximations, we can now predict the wavelengths at which mode coupling will occur for a particular microbend spacing period. We first calculate the propagation constants of the guided and the various cladding modes of a fiber at a specific wavelength. We then obtain the periodicities $\Lambda^{(n)}$ that are required to meet the phase matching condition given by Equation (6.3.1-6). The procedures are then iterated for different wavelengths.

Figure 6.3.3-1 plots the wavelengths where coupling from the fundamental mode to the cladding modes occur as a function of the perturbation period. The current simulation uses a Spectran 830 nanometer singlemode bend-insensitive fiber (cutoff wavelength 750 ± 50 nm, core diameter = 2.5 μm, cladding diameter = 62.5 μm, n_1 = 1.4574, n_2 = 1.4529).

Because the cladding mode propagation constants were approximated by ignoring the effect of the core, the curves in Figure 6.3.3-1 are not accurate indicators of the exact wavelengths at which coupling occur and should be used merely as a guideline. The curves are highly sensitive to small variations in the effective indices of the different modes and the radius of the core and cladding. The curves summarize the behavior of wavelength dependent losses, the wavelength separation of the different cladding modes and their dependence on different periodicities. For example, for a deformation period of 300 micrometers, the simulation shows the first spectral attenuation peak occurring at 720 nanometer for the LP_{11} cladding mode and the last detectable attenuation peak occurring at approximately 920 nanometer.

The graph can also be used as a guide to determine the deformation period that induces spectral losses in the operating range of the spectrometer. Because the spectrometer has a wavelength passband ranging from 750 to 950 nanometers, only deformation periods ranging from 330 to 520 micrometers will have spectral attenuation components that fall within the passband of the spectrometer.

The model developed above can also be used to study the behavior of the wavelength selective attenuation. For example, we can predict the spectral width of the attenuation coefficient peaks as a function of the length of the deformation period. The transmission spectrums shown in Figure 6.3.3-2(a) and 6.3.3-2(b) indicate that the spectral width of the attenuation peak is inversely related to the interaction length of the deformation. However, the amplitude of the attenuation peak is directly related to the interaction length of the microbends. Experimental results have also confirmed this behavior [73].

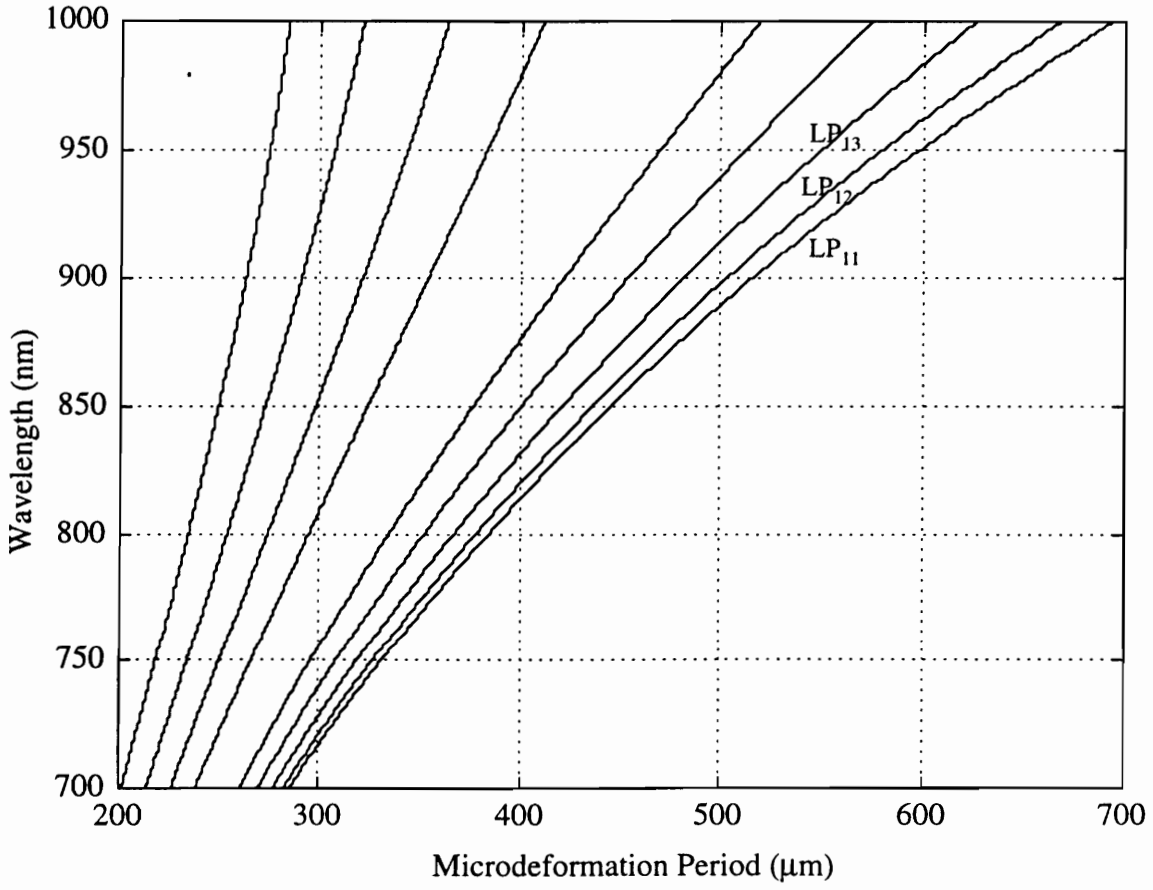

Figure 6.3.3-1. Theoretical determination of the relationship between microdeformation period and wavelength where guided-to-cladding mode coupling takes place for a Spectran 830 nm singlemode bend-insensitive fiber.

The behavior associated with the spectral width versus the number of deformation periods is an extremely important result because such wavelength selective losses will have a dramatic influence on the operation of Fourier transform spectroscopy. In Figure 6.3.3-3, we plot the power spectral densities of the distortion-free Fabry-Perot interferometer and the spectrum for a sensor induced with microbends. Without the influence of microbends, the simulation shows that a sinusoidal interferogram produces one dominant spectral peak and a number of low amplitude harmonic components. With wavelength selective losses, the magnitude of the harmonic distortion components may be equal to that of the fundamental component. We clearly see this behavior in Figure 6.3.3-3 where a microbend interaction length of 0.03 meter produces broadband spectral losses. Wideband spectral attenuation is shown to produce frequency oscillation. The opposite occurs when the interaction length increases to 0.12 meter as depicted in Figure 6.3.3-4 where the wavelength attenuation peaks are sharp but the magnitudes of the Fourier components are smaller.

In processing the signal shown in Figure 6.3.3-3, the discrete Fourier transform algorithm often fails to accurately estimate the gap of the interferometer due to the absence of a dominant spectral peak. The spectral estimation algorithm fails because in trying to locate a particular peak, the output oscillates between these peaks. Figure 6.3.3-5 shows the actual measured spectral losses for a 1300 nanometer singlemode optical fiber subjected to a microdeformation period of 0.97 millimeter over a length of 0.12 meter.

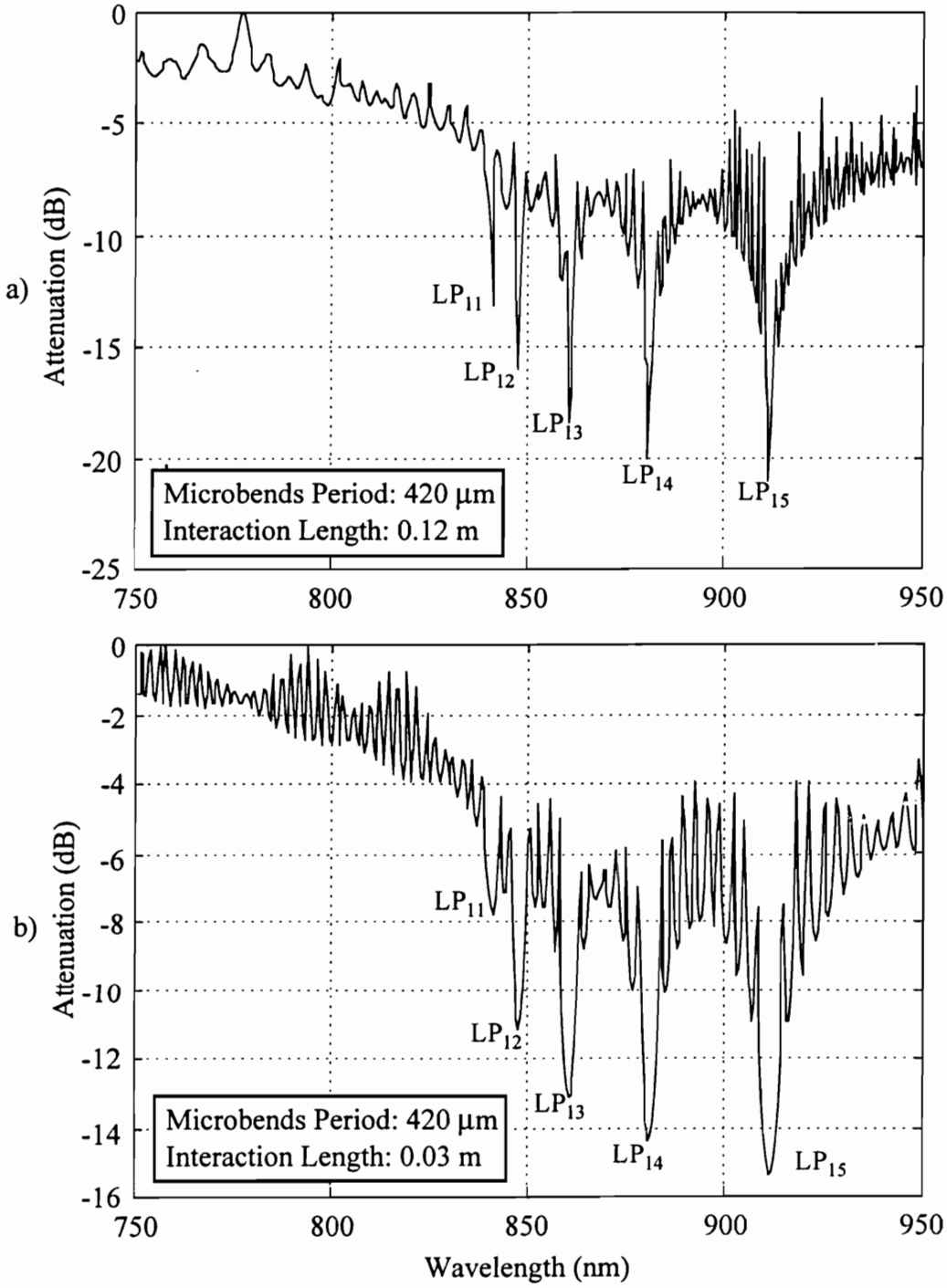

Figure 6.3.3-2. Theoretical determination of the attenuation coefficients α_m as a function of wavelength for a Spectran 830 nm singlemode bend-insensitive fiber deformed by microbends with a period of 420 μm.

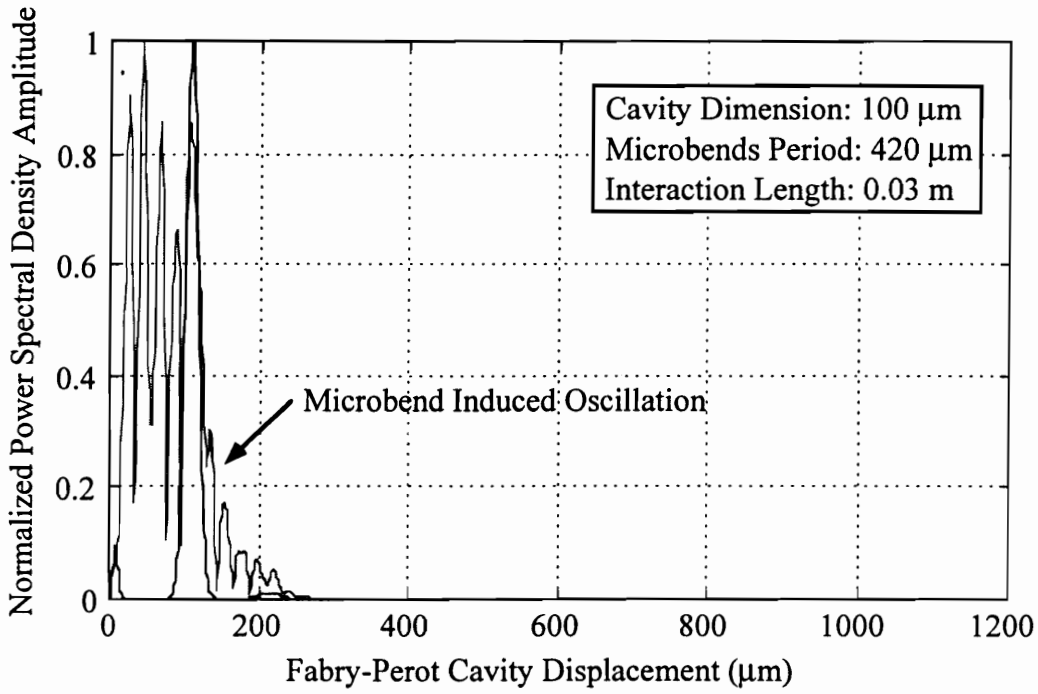

Figure 6.3.3-3. PSD of Fabry-Perot interferometer induced by microbends of 0.03 m in length. Solid line represents PSD of interferometer without microbends.

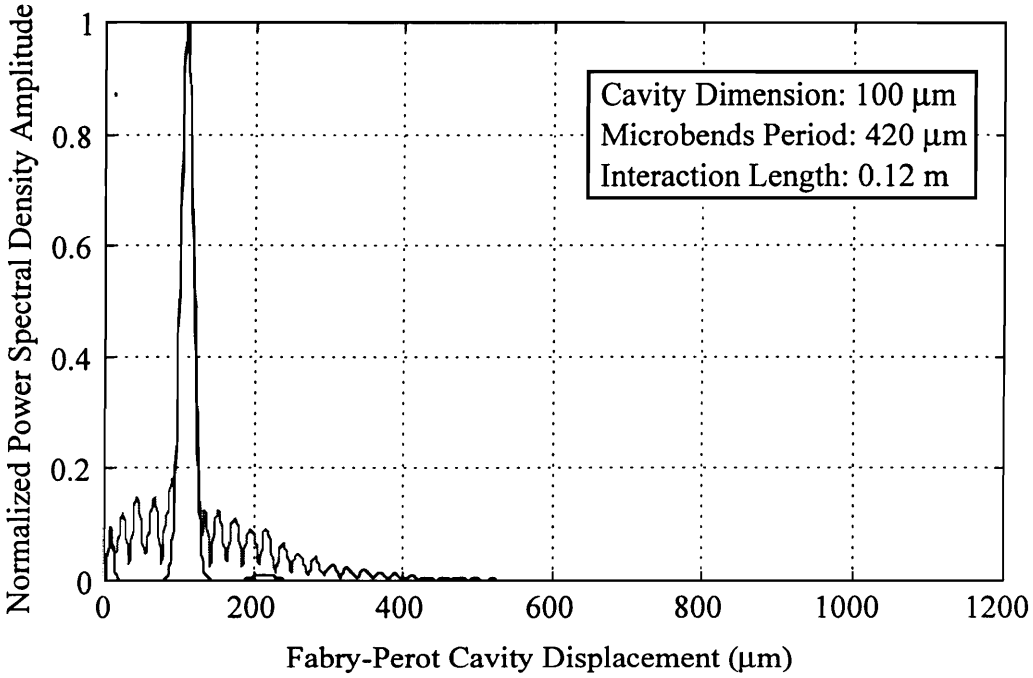

Figure 6.3.3-4. PSD of Fabry-Perot interferometer induced by microbends 0.12 m in length. Solid line represents PSD of interferometer without microbends.

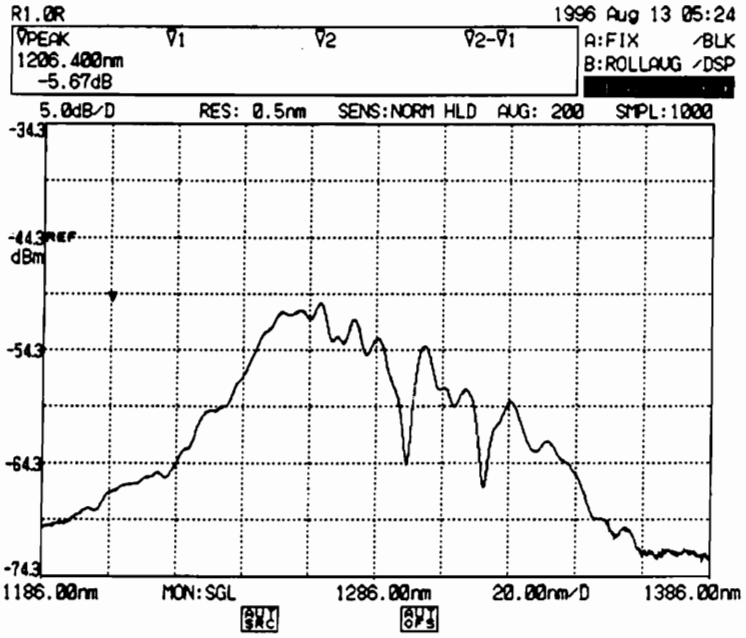

Figure 6.3.3-5. Wavelength dependent losses measured for a 1300 nm singlemode optical fiber subjected to a microdeformation period of 0.97 mm over a length of 0.12 m.

To compare the performance of the classical and chromatic spectral estimation algorithms in an actual experimental setup where the optical fiber is subjected microbends, two 830 nanometer singlemode EFPI sensors were embedded into a 11.5 x 11.5 cm cross-ply composite panel ($[0/90/0/90/0]_s$). The optical fiber sensors were fabricated with singlemode fiber to prevent modal interference and were then placed on the neutral axis of the composite laminate parallel to the reinforcement graphite fibers. Although laying the optical fiber along the axis of the graphite fiber reduces the effect of microbends, this arrangement prevents the embedded sensors from breaking when the composite is cured with a hot press. To compute the sensitivity of the optical fiber sensors to microbends, we monitored the strain produced by the composite laminate as it is being heated.

The experiment was designed so that as the composite laminate expands with temperature, the variation in the spatial period of the microbends will modulate the output signal. As predicted by the theoretical simulation, the Fourier spectral estimation approach causes large sinusoidal output variations compared to the chromatic spectral estimation approach. Figure 6.3.3-6 shows the relative variations associated with each algorithm. We see from Figure 6.3.3-6 that a 1 microstrain variation associated with the chromatic spectral estimation algorithm is two-order of magnitude less severe compared to the 100 microstrain variation associated with classical spectral estimation approach. To illustrate that the microbends do indeed affect the classical spectral estimation and not the chromatic spectral estimation, we calculated the power spectral density of the output strain estimation. The resulting frequency responses are plotted in Figure 6.3.3-7(a) and 6.3.3-7(b). Clearly, the frequency response of the chromatic spectral estimation algorithm is unaffected by microbends since the spectrum shows only a dominant spectral component at the lower frequency with high frequency white Gaussian noise. In

contrast, the frequency response of classical spectral estimation algorithm produces a number of distinct spectral peaks due to the oscillation of the strain output signal shown in Figure 6.3.3-6.

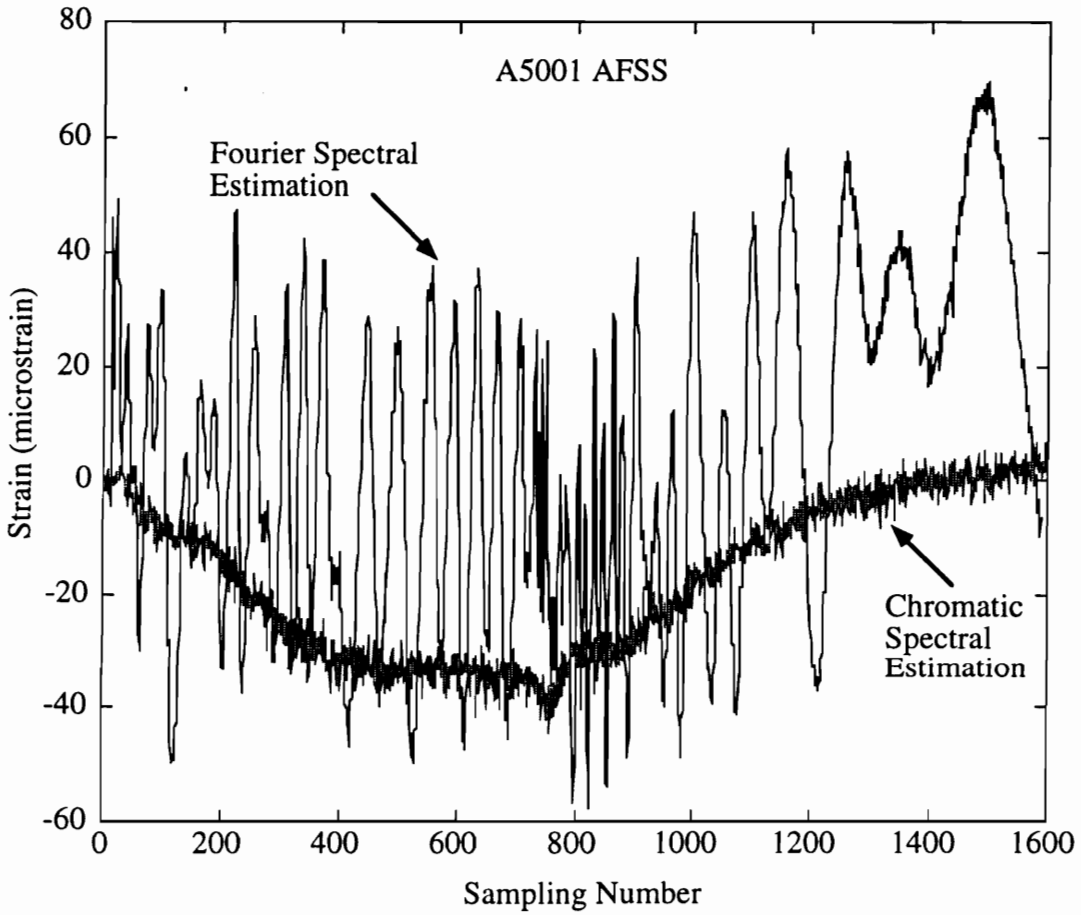

Figure 6.3.3-6. Illustration of the sensitivity of the classical spectral estimation to microbend induced optical losses.

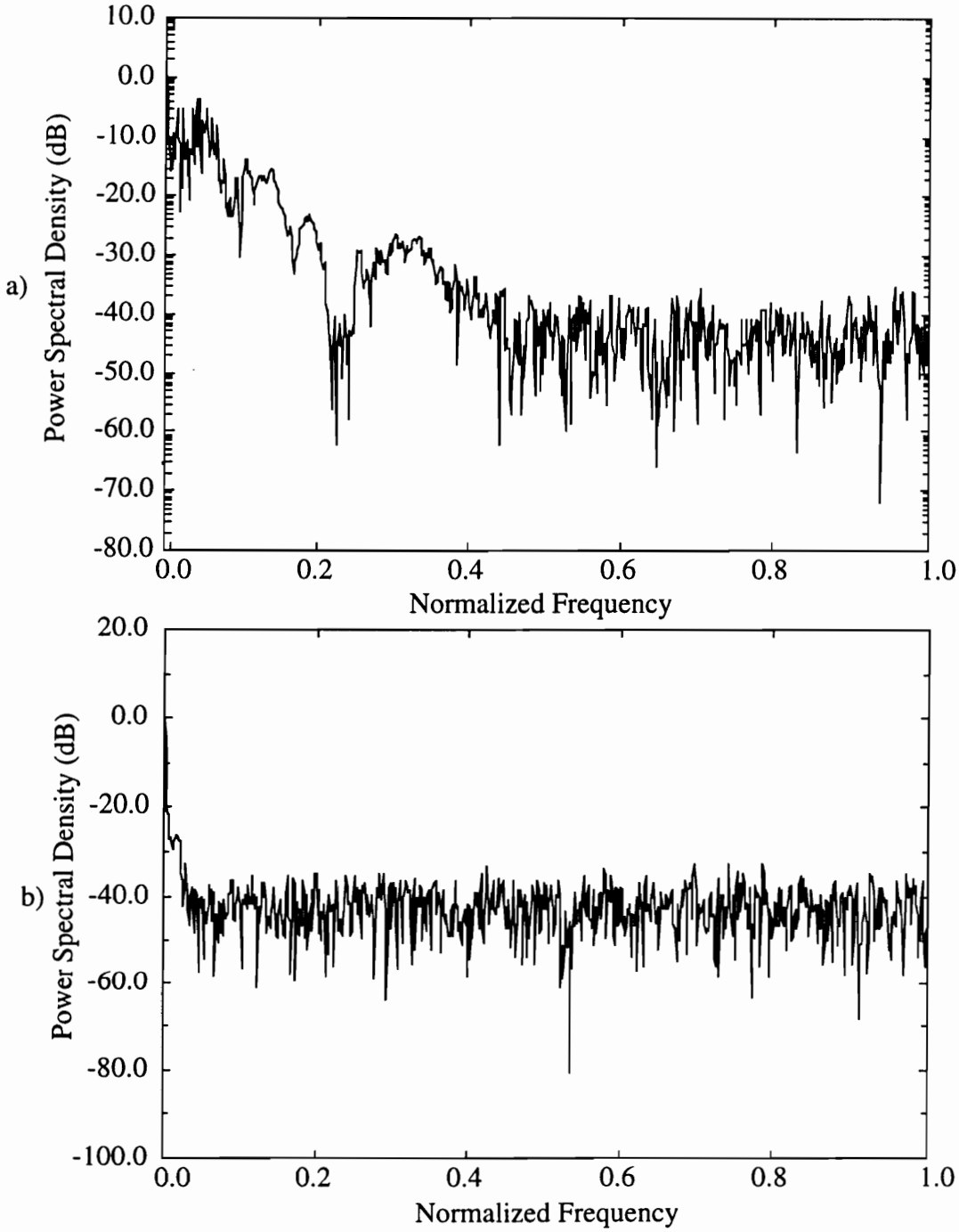

Figure 6.3.3-7. Frequency response showing the sensitivity of the classical spectral estimation algorithm to microbends. Top figure is the PSD of the classical spectral estimation algorithm, and bottom figure is the PSD of the chromatic spectral estimation algorithm.

6.4 Macrobends

It is also well known that dielectric waveguides lose power by radiation when their axes are curved [74-79]. Similar to losses caused by random microdeformation, macrobending losses are also wavelength dependent. However, the major difference is that the guided mode couples energy to a continuum of radiation modes as opposed to discrete cladding modes. Therefore, the losses caused by macrobends are primarily associated with the envelope of the source spectrum and not with the phase of the signal, and thus cause spectral modulation. While macrobending losses will affect the spectral estimation associated with the signal processing employed by the discrete Fourier transform, the resulting errors are less severe compared with microbending losses. However, large errors will result if bends less than 1cm are applied to a singlemode fiber due to a poor signal-to-noise ratio.

6.4.1 Coupling of Guided Modes to Radiation Modes

The calculation of the radiation losses for a dielectric optical waveguide whose axis is bent into a circle represents a challenging problem. Marcatili have approached this problem by regarding the bent waveguide as a ring resonator possessing eigenfrequencies and deriving an eigenvalue equation for the vector modes [74]. This exact approach of solving the problem is very complicated since it requires the evaluation of the Bessel functions in the regime where their large order numbers are comparable to the magnitude of their complex arguments. Even when a scalar approximation is applied to the vector problem, it still does not even lead to a simple computational problem.

Due to the reasons mentioned above, solutions to the bend loss problem have been approached with different approximation techniques. Snyder [78] has proposed solving the curvature loss problem by using the field of the straight fiber as a first approximation in the Kirchoff-Huygens diffraction integral in its vector form. Lewin solved the problem by constructing an appropriate solution for the electromagnetic field [79]. Marcuse approached the problem utilizing the fact that the structure of the field solution outside of the bent waveguide core is known so that an approximate solution of the radiation far field can be obtained by matching the approximate radiation field to the guided mode field near the waveguide core [75]. Recently, Marcuse demonstrated that the bend loss formula may be computed using diffraction theory [76]. In this section, we will summarize the important results from these earlier theoretical developments and use the results to investigate how bending loss affects the performance of the interferometer.

6.4.2 Curvature Loss Formula

The loss formula for curved step-index fibers can be derived by expressing the field outside of the fiber core as an integral expansion in terms of Hankel functions and determining the expansion coefficients by matching the field expansion to the guided mode field along a surface that is positioned tangential to the fiber core. The loss of the fiber may be obtained by calculating the amount of power coupled to radiation modes at infinity. Following this approach leads to the following general formula for curvature loss[77]

$$2\alpha = \frac{4\left|I_1\right|^2}{\pi^{1/2} k_1^{1/2} R^{1/2} I_2 \left|H_\mu^{(2)}(\xi)\right|^2}, \qquad (6.4.2\text{-}1)$$

where R is the bend radius and the Hankel argument $\xi = n_2 k(R + a)$. The bending loss formula involves two integrals,

$$I_1 = \int_0^r \psi(z)dz \tag{6.4.2-2}$$

$$I_2 = \int_0^{2\pi} d\phi \int_0^r |\psi|^2 r\, dr. \tag{6.4.2-3}$$

The function $H_\mu^{(2)}(\xi)$ stems from the expression for the field expansion in terms of the Hankel function. If the field of the LP modes of the straight fiber is substituted into Equation (6.4.2-1), the conventional curvature loss formula derived by Marcatili, Lewin, Marcuse and Snyder is [74,77-79]

$$2\alpha = \frac{2\kappa^2 e^{-2\gamma a}}{e_\nu \pi^{1/2} \gamma^{3/2} R^{1/2} V^2 \left|H_\mu^{(2)}(\xi)\right|^2 K_{\nu-1}(\gamma a) K_{\nu+1}(\gamma a)}, \tag{6.4.2-4}$$

where

$$e_\nu = \begin{cases} 2 & \text{for } \nu = 0, \\ 1 & \text{for } \nu \geq 1. \end{cases} \tag{6.4.2-5}$$

Figure 6.5.2-1 shows plots of the loss coefficient of the LP_{01} mode for different bend radii as a function of the wavelength for a Spectran 830 nm singlemode optical fiber. The graphs show that a bend radius on the order of 1 centimeter leads to significant losses over a broad range of wavelengths. Therefore, the performance of the interferometer degrades gradually as the curvature on the optical fiber becomes more severe. However, the losses associated with curvatures are not wavelength selective compared to effects associated with microbends. Since macrobends do not cause abrupt wavelength attenuation of the output mode field, spectral estimation algorithms based upon the

present frequency processing technique show minor sensitivity to large macrobends. The power spectral density of the attenuation function of Equation (6.2.2-4) is dominant at the lower frequency and may be straight forward to filter from the main spectral peak.

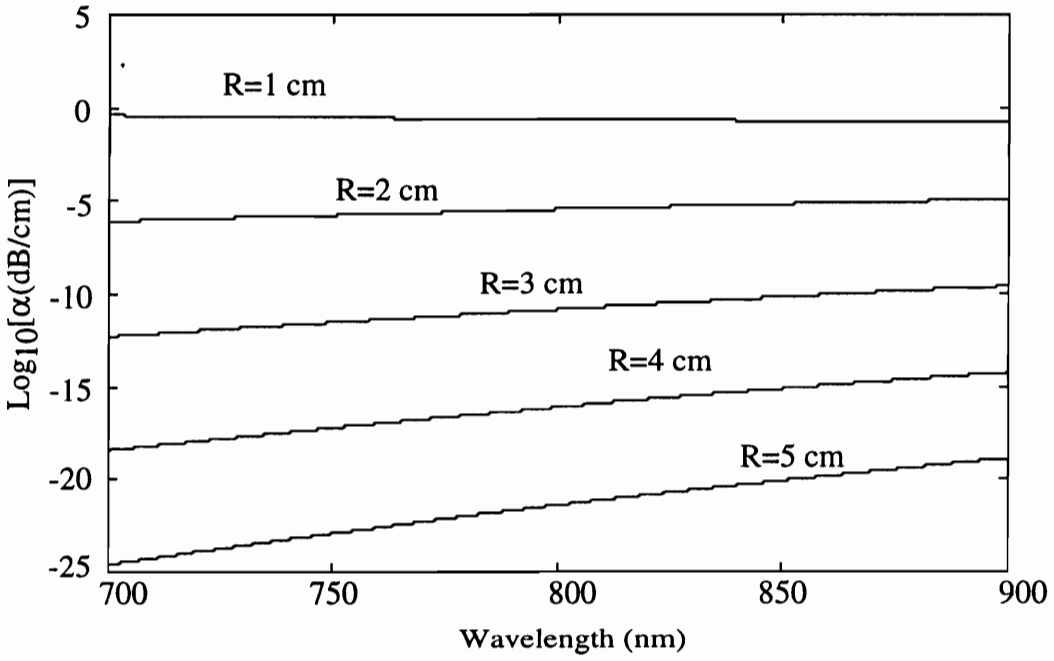

Figure 6.4.2-1. Loss coefficient of LP_{01} mode at various bend radii.

7. Conclusion

New signal demodulation and processing techniques were developed specifically to decode phase modulation information in optical fiber interferometers. The demodulation system uses an electronically scanned CCD array and a diffraction grating for the spectrometer. For signal processing the classical digital spectral analysis approach was extended to accommodate nonlinear effects associated with the sampling of a diffracted optical wavefront. Fourier domain analysis of the modulated spectrum exhibited extremely high spectral estimation resolution capability but the classical approach was shown to be unstable against chromatic distortion. To overcome the intensity fluctuation and source spectra variances, we presented a novel chromatic power spectral estimation technique. For these cases, we anticipated the problem and developed practical methods to resolve these effects.

Unlike amplitude fluctuation, chromatic distortions introduced by the optical waveguide are much more difficult to mitigate. Examples shown in research are wavelength dependent losses that originate by the coupling of guided mode to cladding modes. This waveguide phenomenon occurs when the optical fiber is subjected to periodic microdeformations such that the spatial power spectrum and the phase matching condition are simultaneously satisfied. Mode coupling in the optical fiber causing chromatic distortion produces harmonic distortion in the frequency domain. Therefore, isolating and correlating the spectra associated with the actual sensing signal may become unreliable using the classical spectral estimation approach. The use of this technique in

our spectrometer-based demodulation system has led to erroneous measurement estimations. Practical implementaion of Fourier transform spectroscopy must therefore determine if the microdeformation will cause wavelength selective losses that fall within the operating range of the source spectra.

Modal interference in the optical waveguide is an equivalent effect that was shown to be equally difficult to process. Here, the optical power losses do not occur as an abruptly interrupted signal, but as a slowly decaying function of wavelength. In the frequency domain, the power spectral density of modal interference is concentrated in the lower frequency band and may be easily removed with digital filters.

Our investigation of macrobend induced losses indicated that the attenuation becomes significant as the signal to noise ratio falls below a threshold. To aid in our understanding of the mode coupling that occurs when a waveguide is subjected to perturbations, we employed coupled-mode theory and used the approximated LP mode solutions to derive the modeling simulations.

In summary, a thorough understanding of how errors are introduced in the signal processing algorithm is paramount in designing any demodulation system for optical fiber-based sensors. This research has focused primarily on spectrometer-based systems, but has presented a number of viable decoding systems, including optical cross-correlators. We have attempted to probe issues that affect not only Fabry-Perot based interferometric sensors but other phase-modulated fiber sensor configurations as well. Newly developed fiber sensing configurations such as the Bragg grating and long-period grating sensors, which are susceptible to the same distortion mechanisms, will be prone to similar processing errors if the classical spectral estimation approach is used.

Although this research mainly addressed the fundamental limitations of the chromatic spectral estimation algorithm, future research in this area would need to determine how the algorithm can be optimized to improve its frequency response. A proposed technique would include implementing the algorithm in dedicated hardware designed specifically for digital signal processing applications. Another approach would be to develop a fast chromatic spectral estimation algorithm similar to the fast Fourier transform algorithm. Finally, future research efforts may also include the development of the cross-correlating demodulators briefly discussed in Chapter 3. For example, the Fizeau wedge cross-correlator may be made with a gradient refractive index lens which acts as both a correlating device by introducing a path length difference via the refractive index while focusing the optical signal onto the imaging detector array.

7.1 Summary of Original Contributions in Dissertation

1. Developed and experimentally demonstrated the principles of CCD-based scanning spectrometer for demodulating phase modulated optical fiber sensors.

2. Described several demodulation and signal processing methods that may be used to obtain a self-calibrating sensor demodulation system designed to quantify absolute displacement which can be correlated to the measurement of temperature, strain, and pressure measurements.

3. Extended the classical spectral estimation technique to improve the robustness of the signal processing algorithm against the nonlinear effects associated with an electronically scanned diffraction grating-based spectrometer system.

4. Demonstrated a highly adaptive signal processing algorithm designed to reduce the bias errors associated with source intensity fluctuations and wavelength variances.

5. Investigated how the use of the spectral estimation algorithm in a practical interferometric sensing system is affected by external perturbations applied on the optical fiber including effects such as modal interference, microbends, macrobends, and mode-field distribution.

6. Demonstrated a completely assembled optical fiber sensing, demodulation and signal processing system for strain and pressure measurements.

References

1. Born, M. and Wolf, E., *Principles of Optics*, Pergamon Press, New York, 1985.
2. Saleh, B. E., and Teich, M. C., *Fundamentals of Photonics*, Wiley & Sons, New York, 1991.
3. O'Shea, D. C., Callen, W. R., and Rhodes, W. T., Introduction to Lasers and Their Applications, Addison-Wesley, Massachusettes, 1978.
4. Giallorenzi, T. G., Bucaro, J. A., Dandridge, A., Sigel, G. H., Cole, J. H., Rashleigh, S. C., and Priest, R. G., Optical Fiber Sensor Technology, IEEE J. Quant. Elect., Vol. QE-18, pp. 626-665, 1982.
5. Okamoto, T., Kawata, S., and Minami, S., "Fourier transform spectrometer with self-scanning photodiode array," Appl. Opt., Vol. 23, pp. 269-272, 1984.
6. Takeda, M., and Ru, Q., "Computer-based highly sensitive electron-wave interferometry," Appl. Opt., Vol. 24, pp. 2068-3071, 1985.
7. Johnson, M., "White Light Interferometry," SPIE - Fibre Optics'90, Vol. 1314, pp. 307-314, 1990.
8. Zuliani, G., Hogg, D., Liu, K., Measures, R. M., "Demodulation of a fiber Fabry-Perot sensor using white light interferometry," SPIE - Fiber Opt. Smart Struct., Vol. 1588, pp. 308-312, 1991.
9. Wang, D. N., Ning, Y. N., Palmer, A. W., Grattan, K. T., and Weir, K., "An Optical Scanning Technique in a White Light Interferometric System," IEEE Photonics Tech. Lett., Vol. 6, pp. 855-857, 1994.
10. Lee, C. E., and Taylor, H. F., "Fiber-Optic Fabry-Perot Temperature Sensor Using a Low-Coherence Light Source," Journ. Light. Tech., Vol. 9, No. 1, pp. 129-134, 1991.
11. Belleville, C. and Duplain, G., "White Light Interferometric Multimode Fiber Optic Strain Sensor," Opt. Lett., Vol. 18, pp. 78-80, 1993.
12. Lee, C. E., Gibler, W. N., Atkins, R. A., and Taylor, H. F., "In-Line Fiber Fabry-Perot Interferometer with high reflectance internal mirrors," Jour. Light. Tech., Vol. LT-4, pp. 382-385, 1986.
13. Taylor, H. F., and Yariv, A., "Guide Wave Optics," Proc. IEEE, Vol. 62, pp. 1044-1060, 1974.

14. Wang, A., Gollapudi, S., Murphy, K. A., May, R. G., and Claus, R. O., "Sapphire Fiber-Based Intrinsic Fabry-Perot Interferometer," Opt. Lett., Vol. 17, pp. 1021-1023, 1992.

15. Murphy, K. A., Gunther, M. F., Vengsarkar, A. M., Claus, R. O., "Quadrature Phase-Shifted Extrinsic Fabry-Perot Optical Fiber Sensors," Opt. Lett., Vol. 16, pp. 273-275, 1991.

16. Murphy, K. A., Gunterh, M. F., Vengsarkar, A. M., Claus, R. O., "Fabry-Perot fiber optic sensors in full-scale fatigue testing on an F-15 aircraft," Appl. Opt., Vol.

17. Chen, D. K., *Field and Wave Electromagnetics*, Addison-Wesley, Massachusetts, 1983.

18. Hernandez, G., "Analytical description of a Fabry-Perot photoelectric spectrometer, Appl. Opt., Vol. 5, pp. 1745-1748, 1966.

19. Palik, E. D., Boukari, H., and Gammon, R. W., "Experimental study of the effect of surface defects on the finesse and contrast of a Fabry-Perot inteferometer," Appl. Opt., Vol. 35, pp. 38-50, 1996.

20. Imai, M. Ohtsuka, Y., and Satoh, S., "Spatial coherence analysis of light propagation in optical fibers by interferometric methods," Journ. Opt. Soc. Am., Vol. 3, pp. 1059-1064, 1986.

21. Ning, Y. N., Liu, Y., Grattan, K. T., Palmer, A. W., and Weir, K., "Relation between the coherence length and modal noise in a graded-index multimode fiber for white-light interferometric systems," Opt. Lett., Vol. 19, pp. 372-374, 1994.

22. Papoulis, A., *Signal Analysis*, McGraw-Hill, New York, 1977.

23. Papoulis, A., *Probability, Random Variables, and Stochastic Processes*, McGraw-Hill, New York, 1965.

24. Mandrel, L., Wolf, E., "Coherence Properties of Optical Fields," Rev. Of Mod. Opt., Vol. 37, pp. 231-287, 1965.

25. Ohtsuka, Y., "Optical coherence effects on a fiber-sensing Fabry-Perot interferometer," Appl. Opt., Vol. 21, pp. 4316-4320, 1982.

26. Abramowitz, A., and Stegun, I., *Handbook of Mathematical Functions*, National Bureau of Standards, Washington, DC, 1972.

27. T. A. Tran, W. V. Miller, K. A. Murphy, A. M. Vengsarkar, and R. O. Claus, "Stabilized Extrinsic Fiber-Optic Fizeau Sensor for Surface Acoustic Wave Detection," Journ. Light. Tech., Vol. 10, pp. 1499-1506, October 1992.

28. Fogg, B. R., Wang, A., Miller, M., Murphy, K. A., Claus, R. O., "Optical fiber sensor for absolute measurement," Fifth Annual Smart Matl. and Struct. Work., Blacksburg, Vol. 193, pp. 51-54, 1992.

29. Tran, T. A., Greene, J. A., Jones, M. E. Grace, J., Murphy, K. A., and Claus, R. O., "Optical Fiber Sensor-Based Smart Materials and Structures," Final Report for DARPA Grant No. DAAH01-94-C-R010, 1995.

30. Tran, T. A., Greene, J. A., Jones, M. E. Grace, J., Murphy, K. A., and Claus, R. O., "Optical Fiber Sensor-Based Smart Materials and Structures," July Report for DARPA Grant No. DAAH01-94-C-R010, 1995.

31. Couch, L. W., *Digital and Analog Communication Systems*, MacMillan, New York, 1993.

32. Ando Optical Spectrum Analyzer Instruction Manual, Model AQ-6315A/B, 1995.

33. Ocean Optics, Inc., *OEM Interface Guide*, Dunedin, Florida, January, 1993.

34. Hutley, M. C., *Diffraction Gratings*, Academic Press, London, 1982.

35. Marple, S. L., *Digital Spectral Analysis with Applications*, Prentice Hall, New Jersey, 1987.

36. Bhatia, V., Jones, M. E., Grace, J. L., Murphy, K. A., Claus, R. O., Greene, J. A., and Tran, T. A., "Applications of 'absolute' fiber optic sensors to smart materials and structures," Proc. Tenth Conf. Opt. Fiber Sens., Glasgow, Scotland, October 1994.

37. Bhatia, V., Murphy, K. A., Claus, R. O., Tran, T. A., and Greene, J. A., "Recent developments in optical fiber-based extrinsic Fabry-Perot interferometric strain sensing technology," Smart Matl. and Struct., IOP Publishing, pp. 246-251, 1995.

38. Snyder, R. and Hesselink, L., "High Speed Optical Tomography for Flow Visualization," Appl. Opt., Vol. 24, pp. 4046-4051, 1985.

39. Openheimer, A. V., Schafer, R. W., *Digital Signal Processing*, Prentice Hall, India, 1993.

40. Orfanidis, S. J., *Optimum Signal Processing*, McGraw Hill, New York, 1988.

41. Takeda, M., Ina, H., and Kobayashi, S., "Fourier-transform method of fringe-pattern analysis for computer-based topography and interferometry," Journ. Opt. Soc. Am., Vol. 72, pp. 156-160, 1982.

42. Slogget, G. J., "Fringe broadening in Fabry-Perot interferometers," Appl. Opt., Vol. 23, pp. 2427-2432, 1984.

43. Mahapatra, D. P., and Mattoo, S. K., "Exact evaluation of the transmitted amplitude for a Fabry-Perot interferometer with surface defects," Appl. Opt., Vol. 25, pp. 1646-1649, 1986.

44. Del Piano, V. N., and Quesada, A. F., "Transmission characteristics of Fabry-Perot inteferometers and related electrooptic modulator," Appl. Opt., Vol. 4, pp1386-1390, 1965.

45. Ramsay, J. V., "Aberrations of Fabry-Perot interferometers when used as filters," Appl. Opt., Vol. 8, pp. 569-574, 1969.

46. Prikryl, I., "Analytical description of an imperfect Fabry-Perot etalon," Appl. Opt., Vol. 23, pp. 621-627, 1984.

47. Kauppinen, J., Karkkainen, T. and Kyro, E., "Correcting errors in the optical path difference in Fourier spectroscopy: a new accurate method," Appl. Opt., Vol. 17, pp. 1587-1594.

48. Lai, G., Yatagai, T., "Use of the fast Fourier transform method of analyzing linear and equispaced Fizeau fringes," Appl. Opt., Vol. 33, pp. 5935-5940, 1994.

49. Barnes, T. H., "Photodiode array Fourier transform spectrometer with improved dynamic range," Appl. Opt., Vol. 24, pp. 3702-3706, 1985.

50. Shinpaugh, K. A., Simpson, R. L., Wicks, A. L., Ha, S. M., and Fleming, J. L., "Signal-processing techniques for low signal-to-noise ratio laser Doppler velocimetry signal," Experiments in Fluids, Vol. 12, pp. 319-328, 1992.

51. Hishida, K., Kobashi, K., Maeda, M., "Improvement of LDA/PDA using a digital signal processor (DSP)," Third Int. Conf. On Laser Anemometry, Univ. Of Manchester, Swansea, paper S.2, 1989.

52. Bachalo, W. D., Werthimer, D., Raffanti, R., Hermes, R. J., "A high speed Doppler signal processor of frequency and phase measurements," Third Int. Conf. On Laser Anemometry, Univ. Of Manchester, Swansea, paper S.2, 1989.

53. Marcuse D., *Light Transmission Optics*, Van Nostrand, London, 1972.

54. Gloge, D., "Weakly Guiding Fibers," Appl. Opt., Vol. 10, pp. 2252-2258, Oct., 1971.

55. Snyder, A. W., and Love, J. D., *Optical Waveguide Theory*, Chapman and Hall, New York, 1983.

56. Marcuse D., *Theory of Dielectric Optical Waveguides*, Academic, New York, 1991.

57. Unger, H. G., *Planar Optical Waveguides and Fibers*, Oxford, England: Claredon, 1977.

58. Tosco, F., *Fiber Optic Communications Handbook*, McGraw-Hill, Pennsylvania, 1990.

59 Keiser, G., *Optical Fiber Communications*, McGraw-Hill, New York, 1991.

60. Yariv, A., "Coupled-Mode Theory for Guided-Wave Optics," IEEE J. Quant. Elect., Vol. QE-9, pp. 9191-933, 1973.

61. Snyder, A. W., "Coupled-Mode Theory for Optical Fibers," Journ. Opt. Soc. Amer., Vol. 62, pp. 1267-1277, 1972.

62. Pierce, J. R., "Coupling of Modes of Propagation," J. Appl. Phys., Vol. 25, pp. 179-183, Feb., 1954.

63. Murphy, K. A., Miller, M. S., Vengsarkar, A. M., "Elliptical-core, two-mode, optical fiber sensor implementation methods," IEEE Journ. Light. Tech., Vol. 8, No. 11, p. 1688, 1990.

64. Marcuse, D., "Light Scattering from Period Refractive-Index Fluctuations in Asymmetric Slab Waveguides," IEEE Quant. Elect., Vol. QE-11, pp. 162-168, 1975.

65. Freude, W., and Sharma, A., "Refractive-index profile and modal dispersion prediction for a singlemode optical waveguide from its far field radiation pattern," Journ. Light. Tech., Vol. LT-3, pp. 628-634, 1985.

66. Pask, C. "Physical interpretation of Petermann's strange spot size for singlemode fiber," Elect. Lett., Vol. 20, pp. 144-145, 1984.

67. Peterman, K., "Constraints for fundamental-mode spot size for broadband dispersion-compensated single-mode fibres," Elect. Lett., Vol. 19, pp. 712-714, 1983.

68. Marcuse, D., "Microdeformation losses of singlemode fibers," Appl. Opt., Vol. 23, pp. 1082-1091, 1984.

69. Probst, C. B., Bjarklev, A., and Andreasen, S. B., "Experimental Verification of Microbending Theory Using Mode Coupling to Discrete Cladding Modes," Journ. Light. Tech., Vol. 7, pp. 55-61, 1989.

70. Peterman, K., and Kuhne, R., "Upper and Lower Limits for the Microbending Loss in Arbitrary Single-Mode Fibers," Vol. LT-4, pp. 27.

71. Bjarklev, A., "Microdeformation losses of single-mode fibers with step index profiles," Journ. Light. Tech., Vol. LT-4, pp. 341-346, 1986.

72. Gloge, D. and Marcatili, E. A. J., Bell Syst. Tech. Journ., Vol. 52, p. 1563, 1973.

73. Arya, V., Murphy, K. A., Wang, A., and Claus, R. O., "Microbend Losses in Singlemode Optical Fibers: Theoretical and Experimental Investigation," Journ. Light. Tech., Vol. 13, pp. 1998-2002, 1995.

74. Marcatili, E. A., "Bends in optical dielectric guides," Bell Syst. Tech. Journ., Vol. 48, pp. 2103-2132, 1969.

75. Marcuse, D., "Curvature loss formula for optical fibers," Journ. Opt. Soc. Am., Vol. 66, pp. 216-220, 1976.

76. Marcuse, D., "Bend Loss of Slab and Fiber Modes Computed with Diffraction Theory," IEEE J. Quant. Elec., Vol. 29, pp. 2957-2961, December 1993.

77. Marcuse, D., "Field deformation and loss caused by curvature of optical fiber," Journ. Opt. Soc. Am., Vol. 66, pp. 366-320, 1976.

78. Snyder, A. W, White, I., and Mitchel, J., "Radiation from Bent Optical Waveguides," Elect. Lett., Vol. 11, pp. 332-333, 1975.

79. Lewin, L., Chang, D. C., Kuester, E. F., Electromagnetic Wave and Curved Structures, Peter Pergrinus, England, 1977.

Vita

Tuan Anh Tran was born in Can Tho, Vietnam on October 30, 1965. He received the Bachelor of Science, Master of Science and the Doctor of Philosophy in Electrical Engineering at Virginia Polytechnic Institute and State University in May 1988, May 1991 and December 1996, respectively.

From 1991 to 1992 he was an associate engineer at IBM, East Fishkill, New York, where he worked on developing software to automate the routing of electronic circuits, and the design and packaging of water-cooled multi-chip modules for mainframe computers. While pursuing his doctoral degree at Virginia Tech, he held a position as senior engineer with F&S, Inc. Tuan has led numerous research and development programs with both private and government organizations in designing and developing optical fiber sensors, and advanced instrumentation for civil, biomedical, environmental and aerospace applications.

He is married to Linh Thuy-Do Tran and has two children, Maxwell Anh-Tu Tran and Michael Anh-Hao Tran. In addition to raising a family, enjoying tennis, golf, racketball and volleyball, he is actively involved with the U.S. Congress and international organizations to promote human rights in Vietnam and countries involved in the oppression of these fundamental freedoms.